THE EFFECT OF WELDING SPEED ON THE PROPERTIES OF ASME SA516 GRADE 70 STEEL

A Thesis

Submitted to the College of Graduate Studies and Research

For the Degree of

Master of Science

In the Department of Mechanical Engineering

University of Saskatchewan

Saskatoon, Saskatchewan

By

Alicia Hall

PERMISSION TO USE

In presenting this thesis in partial fulfillment of the requirements for a Master of Science degree from the University of Saskatchewan, I agree that permission for copying of this thesis in any manner, in whole or in part, for scholarly purposes may be granted by the Professors who supervised the thesis work or, in their absence, by the Head of the Department or the Dean of the College in which the thesis work was done. It is understood that any copying or publication or use of this thesis or parts thereof for financial gain shall not be allowed without the author's written permission. It is also understood that due recognition shall be given to the author and the University of Saskatchewan in any scholarly use which may be made of any material in this thesis.

Requests for permission to copy or make other use of the material in this thesis in whole or part should be addressed to:

Head of the Department of Mechanical Engineering

University of Saskatchewan

57 Campus Drive

Saskatoon, Saskatchewan, Canada

S7N 5A9

ABSTRACT

Submerged arc welding (SAW) is often the method of choice in pressure vessel fabrication. This process features high production rates, welding energy and/or welding speed and requires minimal operator skill. The selection of appropriate parameters in SAW is essential, not only to optimize the welding process in order to maintain the highest level of productivity, but also to obtain the most desirable mechanical properties of the weld.

The focus of this study was to investigate the effect of welding speed on the properties of SA516 Grade 70. Plates of SA516 Gr. 70 steel 17 mm x 915 mm x 122 mm were submerged arc welded with a welding current of 700 A and welding speeds of 15.3, 12.3 and 9.3 mm/s. Following the welding; strength, microstructure, hardness and impact toughness of the specimens were examined. Charpy impact testing was performed according to ASTM E 23 on specimens notched in the weld metal (WM) and in the heat-affected zone (HAZ), to measure the impact toughness. Fractography was performed on broken specimens using optical and scanning electron microscopy in order to correlate the mechanisms of fracture with the impact toughness values.

The highest hardness values were in the coarse-grained HAZ followed by the WM with the lowest hardness in the parent metal (PM). The HAZ had higher impact toughness than the WM and PM for all welding speeds. The slowest welding speed (9.3 mm/s) obtained complete penetration and therefore produced the most visually sound weld. The fastest welding speed (15.3 mm/s) had the narrowest HAZ and showed good ductile-to-brittle transition behaviour for both the WM and HAZ specimens, but produced incomplete penetration defects. Welding speed had little affect on the notch toughness of the HAZ with only a 9 J rise in upper shelf energy and an 8 °C drop in the impact transition temperature (ITT) with increased welding speed from 9.3 to 15.3 mm/s. However, for the WM, there was a 63 J drop in the upper shelf energy but also a 41 °C improvement of the ITT between the 9.3 and 15.3 mm/s welding speeds.

ACKNOWLEDGEMENTS

I would like to express my appreciation to my supervisors, Professors Spiro Yannacopoulos and I.N.A Oguocha for their encouragement, guidance, and support throughout this research project. I would like to thank the members of my supervisory committee Professors Qiaoqin Yang and Akindele Odeshi and my external examiner Professor Lisa Feldman for their support, suggestions and useful feedback during the completion of this work. I am also grateful for the assistance, advice and encouragement provided by Professor Barry Hertz.

Technical assistance from Mr. Dave Crone and Engineering Shops is also greatly appreciated as well as Mr. James Amanie's contribution of the tensile testing. Finally, I would like to thank my colleagues for their encouragement and support to make my time more enjoyable.

I would like to express my gratitude to Hitachi Canadian Industries Ltd., in particular Mr. Rob McEachern and Dr. Huawei Guo for their help and provision of materials and welding. Finally, I would like to acknowledge the financial support from Hitachi, the Natural Sciences and Engineering Research Council (NSERC), and the Department of Mechanical Engineering of which I am most grateful.

May God Bless them all.

DEDICATION

I would like to dedicate this thesis to my family, above all to my parents Brian and Carol whose unconditional love, support, guidance and wise advice have always been there for me when it was needed.

TABLE OF CONTENTS

LIST OF TABLES

LIST OF FIGURES

LIST OF ABBREVIATIONS

PVQ	Pressure vessel quality
HSLA	High strength low alloy
SAW	Submerged arc welding
DCEP	Direct current electrode positive
MIG	Metal inert gas
GMAW	Gas metal-arc welding
SMAW	Shielded metal arc welding
FMAW	Flux-cored arc welding
ESAB	Elektriska Svetsnings-Aktiebolaget (Electric Welding Limited Company)
PM	Parent metal
WM	Weld metal
WI	Weld interface
HAZ	Heat affected zone
CGHAZ	Coarse-grained heat affected zone
FGHAZ	Fine-grained heat affected zone
GF	Grain boundary ferrite
WF	Widmanstätten ferrite
AF	Acicular ferrite
M-A	Martensite-austenite
M-A-C	Martensite, austenite, carbide
PF	Polygonal ferrite
B	Bainite
BF	Bainitic ferrite
BU	Upper bainite
BL	Lower bainite
SPF	Side plate ferrite
H	Heat input

E	Arc voltage
S	Travel speed
I	Current
R	Cooling rate
T_o	Preheat temperature
BI	Basicity index
COTD	Crack tip opening displacement
CCT	Continuous cooling transformation
AWS	American Welding Society
ASME	American Society of Mechanical Engineers
ASTM	American Society for Testing and Materials
SEM	Scanning electron microscopy
VHN	Vickers hardness number
ITT	Impact Transition Temperature
DBTT	Ductile-to-brittle transition temperature
P	Penetration depth
b	Bead width
w	Width of the heat-affected zone
R	Bead reinforcement
YS	Yield strength
TS	Tensile strength
EL	Elongation
C	Carbon
Mn	Manganese
Si	Silicon
S	Sulphur
P	Phosphorus
Cu	Copper
Mo	Molybdenum
Ti	Titanium
CO_2	Carbon dioxide

LITERATURE COPYRIGHTS OBTAINED

Figure 2.6 a)	TWI Ltd., World Centre for Materials Joining Technology
Figure 2.6 b)	BB Welding Services, Haverhill, Suffolk, UK
Figure 2.7	BB Welding Services, Haverhill, Suffolk, UK
Figure 2.10	Espoo, VTT, Technical Research Centre of Finland
Figure 2.11	Welding Journal, American Welding Society, Miami, Fla.

1 INTRODUCTION

1.1 Overview

The desire for increased productivity of the manufacturing industry provides an ongoing incentive to find methods to improve the manufacturing processes used. The ability to increase the efficiency of the welding process while maintaining weld integrity has been a source of research for many years.

Selection of appropriate parameters in submerged arc welding (SAW) is essential, not only to optimize the welding process itself, but also to obtain the most desirable mechanical properties of the weld. The integrity of the welded joint is crucial in ensuring the performance of manufactured structures.

It has been well established through research [1-6] that when welding low-alloy steels the objective is to develop weld microstructures consisting mainly of acicular ferrite to achieve good low-temperature toughness. Key factors in the achievement of good toughness include a combination of welding parameters, plate and electrode chemistry, flux composition and cooling rates of the weld metal after welding.

The welding process creates a solidification structure called the weld metal (WM) that is distinct from the parent metal (PM) in both microstructure and chemical composition. The properties of the weld joint are determined by various factors such as the cooling rate and heat input, weld metal composition, solidification features, and the reheating thermal cycles (in multiple pass welds) [7]. The extreme temperatures and the thermal cycles taking place during welding of the molten weld pool alter the base metal microstructure and properties and form a region which is known as the heat-affected zone (HAZ). The size of the HAZ is determined by various welding parameters. In this region, low temperature transformation products such as martensite are likely to form,

which can reduce the toughness [7]. A sketch of the three main regions of a welded joint is shown in Figure 1.1.

Submerged arc welding is often the method of choice in construction of pressure vessels because of the high quality welds it produces and its capability for high production rates. This process also features high welding energy and/or high travel speed and requires minimal operator skill to produce quality welds.

Selection of appropriate welding parameters is essential in order to economically achieve an optimum combination of high strength and excellent low-temperature toughness in welds. The good toughness of acicular ferrite has been attributed to its fine basket-weave microstructure [2, 7, 8]. However, good toughness is dependent on many factors such as the welding parameters, initial grain size [9], post weld heat treatments (i.e. stress relieving) [10], chemistry of the plate, welding rod and flux [11, 12], and the rate at which the weld metal cools.

Many studies [3, 9, 12-14] on the effects of welding process parameters on the toughness of steels have been implemented by changing the heat input by varying combinations of welding parameters including the welding current, voltage and speed. Often at least two of the parameters were varied instead of only varying one in order to study the effect an individual weld parameter. In this project, the effect of the welding speed was observed individually by holding the all of the other parameters constant. This will be effective in order to investigate exactly which parameter, if any, plays a predominant role in modifying the toughness rather than just the heat input in general. Available literature of studies carried out in this way is limited so the knowledge of the effects of the individual parameters does not appear to be well established.

1.2 Research Objectives

The objectives of this project were to

- Determine the effect of welding speed on the properties and microstructure of SA516 Gr. 70 steel.
- Study the relationship between the welding parameters and weld quality.

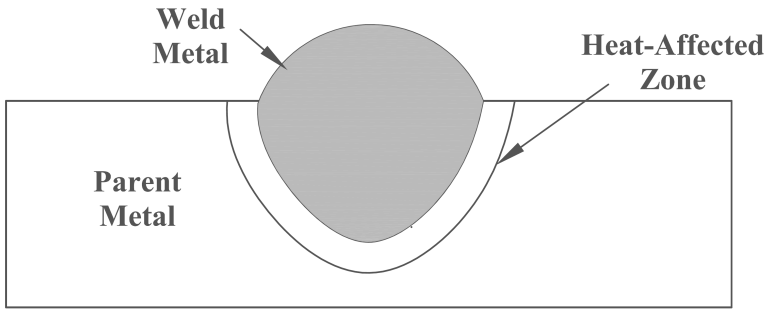

Figure 1.1. Basic regions of a welded joint.

1.3 Motivation

In order to ensure the safety of pressure vessels it is important to have good weld quality and excellent mechanical properties. Toughness is one of the most important factors for ensuring the safety of pressure vessels. High shop productivity in the manufacture of pressure vessels is also desired to reduce costs. Increased productivity can be realized by high speed welding; however, faster welding speed also increases the probability of developing weld defects.

Available literature on the effect of welding speed on the mechanical properties of low alloy steel is limited. To the best of the author's knowledge there is no available literature on the effect of submerged arc welding with increasing welding speeds with a welding current of 700 A and a voltage of 35 V on the mechanical properties of ASME SA516 Gr. 70. Since SAW of this grade of steel is very common in the pressure vessel industry it is important to know how the process parameters affect the mechanical properties.

1.4 Thesis Outline

This thesis consists of five chapters. The first chapter provides an overview of the current research efforts to optimize the efficiency of the welding process through selection of appropriate welding parameters. Chapter 2 presents a comprehensive literature review of SA516 steels, welding, and the effects of welding parameters on submerged-arc welding. The third chapter establishes the materials and experimental procedures used in this study while Chapter 4 discusses the experimental results

obtained in this research. Chapter 5 summarizes the conclusions deduced from the results and suggests recommendations for future work.

2 LITERATURE REVIEW

This chapter discusses the properties and applications of pressure vessel steel ASME SA516 Gr. 70. Fusion welding is discussed with a brief overview of some of the main types with the focus on submerged arc welding. The different zones of a welded joint, their microstructures and properties, and the common weld defects that can occur are also discussed. Finally, a discussion of how welding speed and heat input affect the weld geometry, properties, and microstructures of welds is presented.

2.1 Pressure Vessel Steels

2.1.1 Historical Development of Pressure Vessel Steels

The high pressure differential across the wall of pressure vessels is potentially dangerous and has caused many fatal accidents in the history of their development and operation. For this reason the structural integrity of weldments is critical to the performance of pressure vessels. In recent years much research has been conducted to the study of variations in welding parameters and consumables on the mechanical properties of pressure vessel steel weldments [15-22] to optimize weld integrity and ensure pressure vessels are safe.

2.1.2 ASME SA516 Steel

ASME SA516 (also known as ASTM A516) steel is a C-Mn (Carbon-Manganese) or ferritic steel, which, according to ASTM specifications, is of pressure vessel quality (PVQ) and is normally used in applications requiring moderate- to low-temperature service where excellent notch toughness is important. It is the most popular pressure vessel steel plate grade in the industry and is produced in grades 55, 60, 65, and 70 with grade 70 being the most common. SA516-Gr. 70 has been widely used in nuclear piping or pressure vessel systems because of its relatively good fracture characteristics. This steel is used for pressure vessels in a variety of industries including railway (railcar

pressure vessel parts) [23], petrochemical [22], oil and gas, nuclear [24], shipbuilding, construction, and mining [25].

2.1.3 Main Alloying Elements in A516 Steels

The mechanical properties of steels are sensitive to the amount and type of alloying additions they contain. For example, Keehan *et al* [26] discovered that impact toughness greater than 60 J at –100 ˚C in combination with a yield strength of over 900 MPa was achievable once the optimum level of Mn, Ni, and C were chosen.

It is well known that it is pertinent to choose alloying elements that minimize the formation of martensite. Only a low level (3-wt %) of martensite has been found to downgrade the low-temperature properties of the weld metal [1]. The bulk of common alloying elements shift the "nose" of a continuous cooling diagram to the right, allowing finer-grained structures to develop under a lower cooling rate [1].

The dominant alloying elements of SA516 Gr. 70 steel and their effects are briefly described in the following paragraphs.

Carbon, C (0.22 wt %)

Carbon is the most important alloying element in steel. Additions of carbon strengthen and harden steel, and increase its wear resistance and ability to harden by heat treatment. However, higher carbon contents hinder weldability, decrease the ductility, and reduce impact toughness of the steel [27]. McGrath *et al.* [22] found that a 0.1wt % carbon level gave optimum toughness in a Cr/Mo pressure vessel steel. Carbon in excess of 0.2 wt %, in carbon steels, forms hard microstructures such as martensite or bainite [27] that are susceptible to hydrogen cracking.

Manganese, Mn (1.14 wt %)

The main reason manganese is added to steels is to counteract the harmful effects of sulphur. Manganese can also be added to provide solid solution strengthening [27, 28], deoxidization [28], and improve machinability [29]. It can increase strength, promote grain refinement, and increase hardenability [29]. Additions of manganese can improve

toughness [27] but has been found to cause rapid deterioration of notch toughness when manganese content in submerged-arc weld metal was above 1.6 wt % [30].

McGrath *et al*. [19, 22] found that the presence of manganese (1.37 wt %) in SA516 Gr. 70 steel encouraged the formation of acicular ferrite in the columnar region and refined the polygonal ferrite (PF) in reheated regions of a multipass weld. They also found that manganese contributed to SA516 Gr. 70 by lowering the temperature at which austenite transforms to ferrite.

Silicon, Si (0.24 wt %)

Silicon is added to steels primarily to act as a deoxidizer and to increase the strength and hardenability. Strengthening occurs through solid solution strengthening of ferrite [27]. However, high proportions of Si are avoided, as it tends to deteriorate toughness and weldability [27]. For example, McGrath *et al.* found that a high silicon (0.8 wt %) had an undesirable effect on the low temperature toughness of a C-Mn SA516 Gr. 70 steel by encouraging the formation of martensite-austenite (M-A) microphases [19].

Other Minor Alloying Elements

Strengthening of steels is also achieved by the other minor alloying elements such as molybdenum, chromium, titanium, nickel, copper, and nitrogen. Molybdenum, chromium, and nickel are added for hardenability. Nickel has also been found to increase toughness [4].

Toughness is affected by minor elements such as molybdenum by lowering the ductile-to-brittle transition temperature (DBTT) and refining the grain size. However, excessive addition of molybdenum (0.5 wt % [19]) has been found to encourage the formation of coarse-grain boundary ferrite and ferrite with aligned second phase, both of which cause poor low-temperature notch toughness properties. Titanium retards austenite grain growth, increases the fraction of acicular ferrite [4], lowers the DBTT, and raises the grain coarsening temperature. Small aluminium additions improve the toughness by promoting a fine grain size [6, 29, 31].

2.2 Fusion Welding

Fusion welding is a steel joining process, which involves melting two edges or surfaces and joining them by adding a small amount of molten steel, or filler metal, into the gap between the two components [32]. When the weld pool cools the molten metal solidifies forming a bond with the parent metal. A continuous joint between the two components is formed once solidification is complete.

Arc welding is the main type of fusion welding. This includes a variety of processes, which use a heat source or electric arc to melt and join two components. The type of electrode material and the type of shielding technique are often used to classify the different arc welding processes. Shielding of the arc from the atmosphere is necessary to obtain welds with optimum strength and ductility. Without protection the molten steel readily absorbs oxygen and nitrogen from the air as it cools which can impair the strength and toughness of the welded joint [33]. This can also lead to porosity defects in the weld or other metallurgical problems such as embrittlement. This protection from the atmosphere can be obtained through multiple techniques, which include surrounding the arc with flux, gas, or a combination of the two [6]. Many forms of fluxes are available including granular powder or coated metal rods. Fluxes shield the molten metal by keeping out the atmosphere, help remove impurities from the molten weld deposit, and provide a blanket of slag. The slag blanket over the weld serves two functions including stabilization of the arc and decreasing the cooling rate [34].

Shielded metal-arc welding (SMAW) (or manual metal arc welding) uses a consumable flux-coated electrode, which forms a gaseous shield as the electrode and flux coating decompose in the arc to provide protection from atmospheric contamination. When welding, the electrode coating forms a blanket of slag providing additional protection while the electrode core serves as filler metal [35].

Flux-cored arc welding (FMAW) uses a consumable, flux-filled electrode which, when melted, produces gases that provide shielding. Auxiliary gas (normally carbon dioxide) can also be added for additional shielding if necessary [35]. The difference between flux-cored arc and shielded metal-arc welding methods is that instead of the electrode

being flux-coated, it is flux-cored. Having the flux on the interior of the electrode as opposed to as a coating is superior as it makes coiling possible so that the wire can be continuously fed rather than being limited in length. This allows the process to be fully automated [35].

Gas metal-arc welding (GMAW), otherwise known as MIG (Metal Inert Gas) welding, uses a bare solid wire consumable electrode that is continuously fed into the arc and is consumed as filler metal. Atmospheric contamination protection is provided by a gaseous shield, fed through the electrode holder in the form of a stream of gas, or a mixture of gases. With no slag this process is faster than some of the others (i.e. flux-cored arc welding) as there is no need for slag removal between passes. However, the lack of slag cover increases the rate of cooling making the welds produced more susceptible to weld-metal cracking [35].

The choice of welding method to be used for particular applications can be determined by a combination of feasibility and economics. In the welding of pressure vessels it is preferred to weld the main seam welds in the flat position. Due to the thickness of the plates to be welded it is also necessary to maximize the deposition rate of the weld metal. Submerged arc welding (SAW) is the method most commonly chosen to weld pressure vessels because it is both feasible and economical [6].

2.2.1 Submerged Arc Welding

The method of welding featured in this study is submerged arc welding. Submerged arc welding (SAW), illustrated in Figure 2.1, uses a large diameter, bare-metal electrode that is fed into the arc at a controlled rate. Granular, fusible flux is poured to form a pile surrounding the arc, blanketing the molten weld and base metal and protecting them from atmospheric contamination [35, 36]. Operation of the SAW process can be either semiautomatic or fully automatic [35].

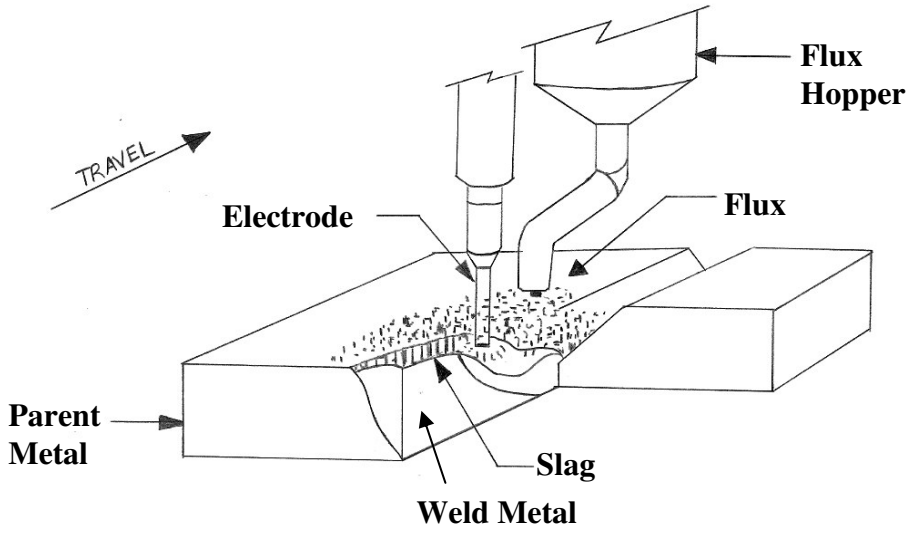

Figure 2.1. The SAW process [adapted from 37].

With this method only welds in the flat and horizontal positions are possible. Speeds up to 84 mm/s are achievable and metal deposition rates have been reported up to 45 kg/h (100 lb/h) [38]. Deep joint penetration can be achieved, little edge preparation is required, and the welds produced are uniform with good impact toughness values [38].

Some of the flux is converted to slag by the arc, which protects the weld as it cools. The slag can easily be chipped off the weld once cooled and the surplus flux is then collected for re-use. The flux blanket conceals and shields the arc removing the need for eye protection while nearly eliminating weld spatter and sparks. Besides acting as a protective shield, the flux blanket may also supply deoxidizers and modify (or add to) the chemical composition of the weld metal [35].

SAW is often the method of choice in the manufacture of pressure vessels because of the high production rates it offers. High welding energy and/or travel speed are often involved which cause a large amount of dilution or mixing with the parent metal. Due to mixing, the composition of both the base metal and welding consumables may have a similar effect on the notch properties of the weld [1]. The choice of a proper combination of electrode and flux are therefore important considerations. The goal is to achieve strength, toughness and corrosion resistance properties of the welded joint that closely match those of the base metal [36, 39].

2.3 Weld Zones and Their Structures

During cooling and solidification of the weld pool, considerable heat is conducted out through the parent metal. The heating and cooling cycles result in a weld comprising of four distinct metallurgical zones (see Figure 2.2) including the: 1) unaffected zone or parent metal (PM); 2) weld interface (WI) or fusion line; 3) heat-affected zone (HAZ); and 4) the fusion zone or weld metal (WM). The respective sizes of each of the zones across the weld are a result of a balance between the rate of heating and the rate at which heat is conducted away. The structure of the weld zones is strongly influenced by the presence of alloying elements, including carbon content. The structures that will develop from a particular set of cooling conditions with a particular type of steel can be predicted with the use of the continuous cooling transformation diagrams.

2.3.1 The Unaffected/Parent Metal Zone

The unaffected zone includes the metal that is sufficiently removed from the heat source such that it remains unaffected by the heat of welding and no alteration occurs to its mechanical properties and/or microstructure. Therefore, the structure of the parent metal remains in its cold-worked state and retains the associated properties. The typical grain structure of the parent metal of low-carbon steel is of ferrite and pearlite [34]. Consistent with this, Huang *et al*. [17] reported the microstructure of unaffected SA516 Gr. 70 steel to consist of a ferrite/pearlite-banded structure.

2.3.2 The Weld Interface

The weld interface is the narrow boundary that separates the fusion zone and the heat-affected zone. The base metal in this narrow zone has undergone full or partial melting during the welding process. This material, at the edge of the fusion zone, remains unmixed with the filler metal.

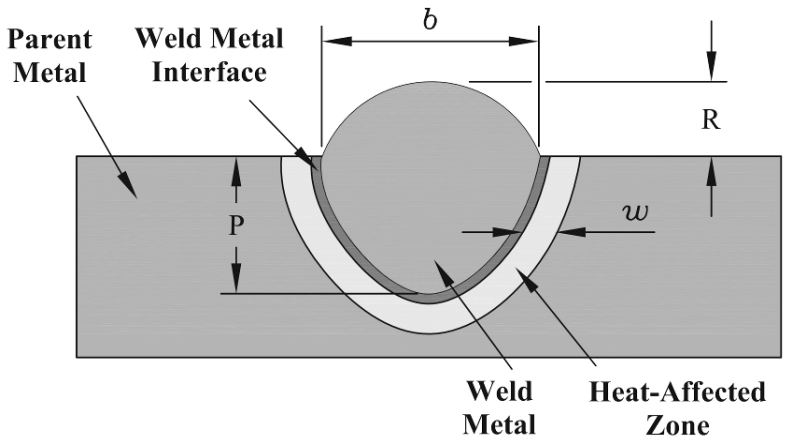

Figure 2.2. Zones of the welded joint and weld geometry parameters.

2.3.3 Heat-Affected Zone

Immediately adjacent to the weld there is a region which has not melted but has undergone change to its microstructure and mechanical properties due to the heat encountered during welding. This region is called the heat-affected zone (HAZ). The HAZ retains the chemical composition of the parent metal but its properties are controlled by a combination of factors such as the welding heat input and prior and postweld heat treatments that have been used [40].

The heat-affected zone of a welded component is characterized by high levels of embrittlement due to the coarse grain structure that develops from time spent at elevated temperatures above the grain coarsening temperature. Above the grain coarsening temperature the growth of austenite grains is uninhibited so the longer the material spends above this temperature the larger the grain structure will be [6]. As coarse grain structure provides low resistance to crack propagation the HAZ has been considered the region of a welded joint most prone to potential crack initiation and failure. Concerns about the HAZ originate on account of the many past failures that have been associated with HAZ cracking. These concerns have generated extensive research and testing on the mechanical properties, particularly the toughness, of the HAZ [3, 9, 13-16, 20, 21, 40-57]. However, the concern for the HAZ brittleness may not always be warranted if the toughness of the HAZ, at any given temperature, can be proven to be greater than

that of the parent metal. Structurally it is not necessarily the low toughness of the HAZ but its toughness relative to that of the base metal that is important [15, 56].

Upon cooling, the austenite grains within the HAZ transform into a variety of possible microstructures. The microstructure that forms is controlled by the chemical composition of the steel and the rate at which the molten metal cools. In turn the cooling rate is determined by the arc energy or heat input to the joint, the steel thickness, the type of joint, and the preheat temperature of the steel [36].

The transformation of austenite under a rapid cooling rate can lead to the formation of martensite in the heat-affected zone. This causes hard, brittle regions in the HAZ, which have high strength but low ductility. To maintain good toughness in a weld the development of martensite should be avoided and thus good control of the welding process is essential. Maintaining a low percentage of carbon can help to prevent the formation of martensite.

The size (or width) of the HAZ, to an extent, gives an indication of its toughness and grain size. A high cooling rate will result in a narrow heat-affected zone (HAZ) region, a fine grain size, and consequently good toughness. Very high cooling rates, however, will cause formation of martensite or bainite, which lower the toughness. Similarly, low cooling rates correspond with wide HAZs, large grain sizes, and inferior toughness [58].

The HAZ consists of at least three different microstructural zones that include a coarse-grained (grain-growth) zone, a fine-grained (grain-refined) zone, and a transition zone. The grain size within the HAZ is regulated by the grain coarsening temperature of the steel and the weld thermal cycles encountered. Coarser grains will be produced with higher rates of heat input and with more time spent above the grain coarsening temperature [6]. The maximum grain size will occur near the weld fusion boundary and will decrease with distance from that boundary [59]. Figure 2.3 illustrates the microstructure of each zone within the welded joint as they relate to temperature. The hardness of the different regions varies: gradually declining from the weld interface to the coarse-grained zone. Higher hardness values usually correlate with increased brittleness and reduced ductility [59].

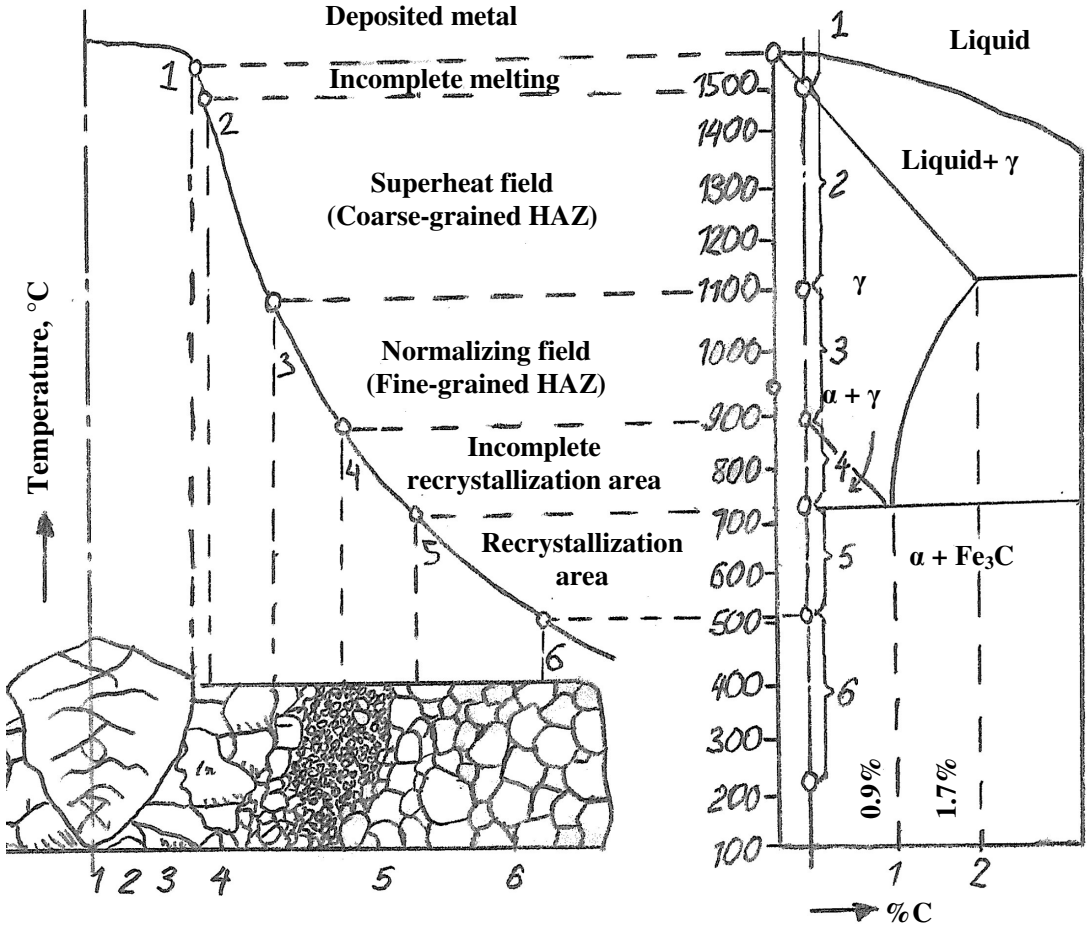

Figure 2.3. Schematic representation of the microstructures at different temperatures within the welded joint [adapted from 60].

The coarse-grained zone (CGHAZ) of the HAZ is located adjacent to the fusion boundary of the weld metal and consists of large prior austenite grains that have grown due to considerable time spent at extreme temperatures near the melting point of the metal [6]. These thermal cycles can substantially alter the HAZ microstructure within the prior austenite grains, with the degree of deterioration depending on the composition of the steel and the welding process parameters. This deterioration of the HAZ can considerably influence the integrity of a structural component and increase the occurrence of failure by brittle fracture. The CGHAZ is normally considered to be the region of the welded joint with the lowest subzero temperature toughness causing researchers to label it as a local brittle zone [3, 43, 49, 52, 53, 55, 56]. The low

toughness found in this zone can be explained by the formation of undesirable microstructures within the prior austenite grains upon reaustenization. Some typical low toughness microstructures that may form in this zone include upper bainite, martensite, coarse prior austenite grains, microalloy precipitates, and martensitic islands [49, 52, 53, 55]. The high carbon martensitic island, or martensite-austenite (M-A) constituent (also known as M-A-C or martensite, austenite, carbide), has been reported to be the most likely cause of deteriorated toughness in the CGHAZ because it has high hardness and is susceptible to crack propagation [49, 52, 53, 55]. For example, Kim *et al.* [52] and Lee *et al*. [53] (in overlapping studies) reported voids and microcracks initiating at the M-A constituents in the HAZ. The type of microstructure that forms depends on the cooling rate and/or carbon content of the steel. Higher cooling rates and higher carbon content produce harder, acicular structures such as martensite or upper or lower bainite or a combination of these constituents. Coarser prior austenite grains will form coarser microstructures (i.e. larger blocks of proeutectoid ferrite or wider spaced martensite laths) and may encourage harder microstructures to form [6].

The finest grain structure exists within the region called the fine-grained zone (FGHAZ). The grains in this region have reached temperatures, which correlate with complete grain refinement. Due to the complete recrystallization occurring at these temperatures the austenite forms much finer ferrite and pearlite [34] than the original parent metal.

The transition zone is the region beyond the coarse and fine-grained zones where only partial transformation to austenite (or austenization) occurs. The pearlite regions in this zone have been refined but the ferrite grains remain unaltered [34].

Clark and Varney [34] described the structure of the CGHAZ of low-carbon steel to contain large regions of pearlite with smaller ferrite grains. They reported the area closest to the fusion zone, transformed from large austenite grains during an intermediate rate of cooling, containing the coarsest structure to be of the Widmanstätten type, consisting of ferrite lines interleaved between pearlite areas. On the other hand, Güral *et al*. [57] found, for low carbon steel (AISI 1010), the

microstructure of the HAZ near the fusion line to typically contain coarse-grained polygonal ferrite and pearlite colonies.

Huang *et al.* reported that the HAZ microstructure can be ferritic, pearlitic, bainitic, or martensitic etc. [17]. In a SAW weldment of SA516 Gr. 70 obtained from a welding heat input of 4.5 kJ/mm they found the main phase of the CGHAZ to be of Widmanstätten ferrite (WF). This concurred with what was reported in Clark *et al.* for low carbon steels [34]. Yang [16] in his testing of SA516 Gr. 70, for heat inputs between 1.83 to 4.15 kJ/mm, found the HAZ structure to mainly consist of interlocking laths of ferrite, a network of prior austenite grain boundaries and carbide or martensite otherwise called martensite, austenite, carbide (M-A-C).

For HY-80 McGrath *et al*. [3] reported the microstructure in the CGHAZ under a variety of heat inputs (2 and 4 kJ/mm) to be a completely martensitic structure with intergranular discontinuities.

Sundaram *et al*. [54] found that the HAZ obtained by manual metal arc welding (with heat input of 1.6 kJ/mm) for Tisten 55 (equivalent to ASTM A 572 Gr. 50 Type 1) contained a martensite-type structure as well as AF and some PF. In contrast, a CO_2 weld with similar heat input (1.75 kJ/mm) revealed the presence of martensite-type structure and fine ferrite. Similarly, Moon *et al*. [61] found the HAZ microstructure in their testing of HSLA-100 welded at a heat input of 1.2 kJ/mm to be martensitic consisting of untempered lath martensite and coarse autotempered plate martensite. However the parent metal of the HSLA-100 originally consisted of primarily of fine-lath martensite and an abundance of coarse martensite while that of Tisten 55 steel consisted of elongated grains of ferrite and pearlite.

2.3.4 Fusion Zone or Weld Metal

The fusion zone (or weld metal) is the zone where the parent metal melts and intermixes with the filler metal and forms a new alloy. The weld metal mixture is sometimes about 50-75% [1] parent metal combined with melted electrode. The addition of the filler metal to the weld gives the region a “cast structure of coarse columnar grains known as the deposited metal zone” [6]. The structure of this zone is relatively homogenous. The

columnar structure is formed as the welded joint cools from the parent metal in towards the centre of the weld metal.

Contributors to the final weld metal microstructure include the heat input and cooling rate through the transformation range, PM composition, solidification features, prior austenite grain size [2, 7], hardenability of the weld deposit [18], and, in multiple pass welds, the reheating thermal cycles [7].

Transformation of the weld microstructure primarily depends on the rate at which the metal mixture cools from the temperatures of the austenitic region and on the alloy content of the steel. Increasing the cooling rate, and thus reducing the heat input, lowers transformation temperatures [6]. Weld microstructures progressively refine with increases in the cooling rate from grain boundary ferrite (GF) to side plate ferrite (SPF), acicular ferrite (AF), bainite, and eventually to martensite [7]. The intergranular formation of acicular ferrite has been found to thrive from a mid-level cooling rate and the presence of inclusions [2]. The mid-level cooling rate does not allow much time for formation of proeutectoid ferrite at the grain boundaries but is not fast enough to form bainite or martensite. The dominant weld structure that forms under high cooling rates is ferrite in the form of groups of parallel laths separated by carbides or retained austenite. Exceptionally high cooling rates, however, are likely to form martensite [2].

Figure 2.4 is the continuous cooling transformation curve for a carbon-manganese steel weld deposit. From this diagram it can be seen that as the weld deposit cools proeuctectoid ferrite begins to form around austenite grain boundaries. Subsequently, the interior of the grains transforms into either acicular ferrite or side plate ferrite or a combination of the two. Martensite and carbides may form between grains of ferrite and some austenite may be retained. The major microconstituents of the final weld microstructure therefore will consist of a mixture of primary ferrite (grain boundary and/or polygonal) ferrite and Widmanstätten ferrite (WF). The WF may be in the form of side plates or a fine acicular ferrite [34]. Upper bainite as well as microconstituents such as pearlite, cementite and martensite may also be found in the weld metal microstructure of low carbon, microalloyed steels [7].

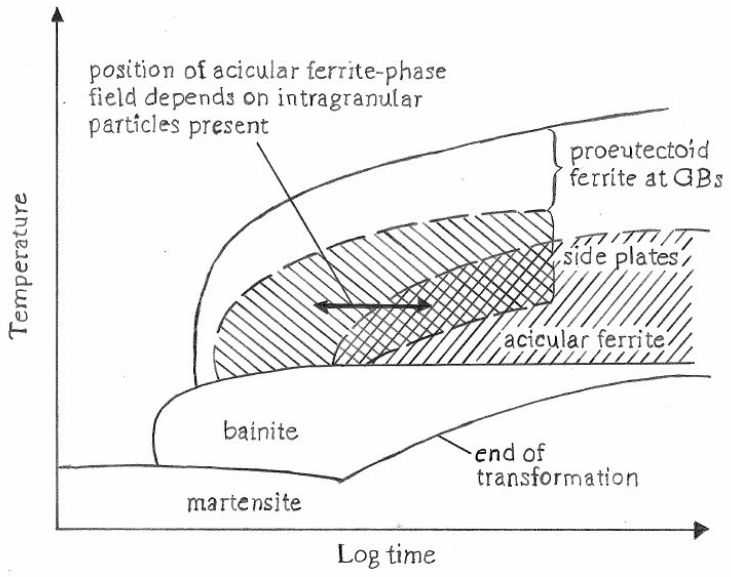

Figure 2.4. Continuous cooling transformation (CCT) diagram for a typical carbon-manganese (C-Mn) weld deposit [adapted from 6].

It is generally accepted that the optimum notch ductility or good low-temperature toughness of weld metal is obtained by a microstructure consisting of mainly acicular ferrite (AF) [1, 3-7, 18, 19, 22, 28, 42]. This has generated considerable research focused on obtaining the optimum volume fraction of acicular ferrite in high heat input submerged arc weld metals. Research has found that the primary requirements for optimum toughness include not only a microstructure of predominately acicular ferrite but also a combination of a fine grain size [12, 18] (2-5 μm [5]) and a low level of inclusions [1, 3, 14, 18]. However, although Lazor *et al*. [4] discovered that acicular ferrite content generally increased the amount of energy absorbed at -20 ˚C and at +22 ˚C they saw very little effect of the acicular ferrite content on the toughness of steel at temperatures down to -60 ˚C. They concluded that although acicular ferrite increases toughness it does not provide significant benefit to very low temperature toughness [4].

Acicular ferrite is "a fine Widmanstätten constituent which has been nucleated by an optimum intragranular dispersion of oxide-silicate particles" [6]. Its toughness can be attributed to its basket-weave type structure [2, 7, 8] consisting of short, randomly oriented needles of ferrite [2, 7]. It has also been described to consist of "highly dislocated, low-aspect-ratio (4:1) ferrite laths, typically 1-3 μm wide, separated by high-

angle grain boundaries" [14]. Its interlocking structure and fine grain size give acicular ferrite low temperature notch toughness values and resistance to crack propagation [2, 7] because it forces cracks to "re-initiate at the closely spaced high-angle boundaries" [14].

Microstructures that should be minimized because they are known to degrade the weld toughness include feathery upper bainite, coarse GF, and proeutectoid ferrite [2]. Also, unless stress relief through tempering is an option, even the smallest quantity of martensite should be avoided [1].

Consistent with the CCT diagram in Figure 2.4 [6], Huang *et al.* [17] reported that the weld metal of SA516 Gr. 70, produced using SAW with a heat input of 1.5 kJ/mm, consisted of a mixture of GF, AF and WF. Güral *et al.* [57] found the same microstructure combination in their MIG welded AISI 1010 steel weldment with a similar heat input of 1.9 kJ/mm. Similar to Huang *et al.*, Yang [16] reported the weld metal of SA516 Gr. 70 to consist of AF, GF, and block ferrite for heat inputs of 1.83 to 4.15 kJ/mm.

McGrath *et al*. [19, 22] performed two studies of SAW of SA516 Gr. 70 for narrow groove welds deposited in thick sections. A part of each study included testing of the same material, welding parameters, and flux/electrode combination (i.e. welds CM1 and CM2 in [22] are equivalent to NG1 and NG3 in [19]). The as-deposited weld metal microstructure of weld CM1 or NG1 which used a flux/electrode combination providing 1.37 wt % Mn consisted of an elongated columnar structure comprising primarily AF and fine PF in the reheated region. The prior austenite grain interiors contained AF. The second phase observed was composed of either elongated martensite-austenite (M-A) microphases, containing retained austenite and twinned martensite, or carbides. The reheated region consisted of fine PF. As-deposited weld metal of CM2, which used a flux/electrode combination providing only 0.91 wt % Mn, featured coarse GF and ferrite with second phase, and a coarser PF (than CM1) in the reheated region. In Figure 2.5 the weld CM1 with a mainly AF microstructure in the as-deposited region and fine PF in the reheated region showed superior resistance to both low temperature brittle fracture and high temperature ductile fracture than CM2.

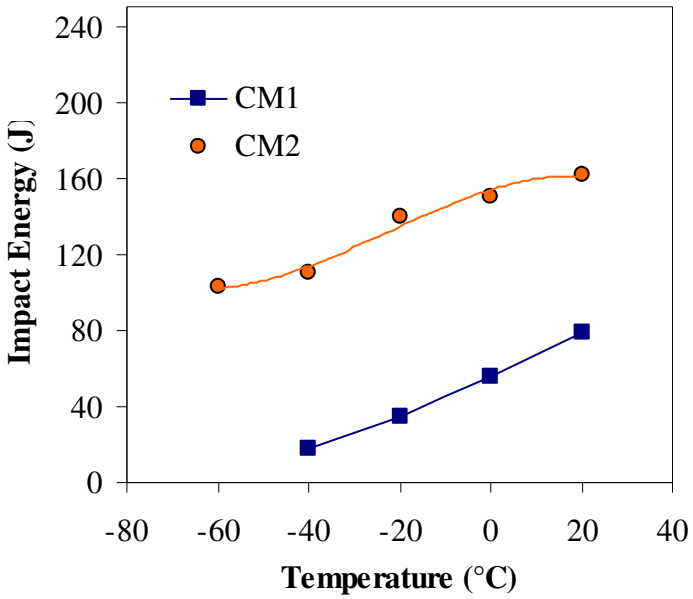

Figure 2.5. Charpy transition curves of SAW-NG welds of SA516 Gr. 70 C-Mn steel [adapted from 22, not to scale].

In Smith *et al.*'s [14] study of HSLA-80 steel (a modified version of ASTM A710 Gr. A Class 3), welded with SAW at heat inputs ranging from 2-4 kJ/mm, the as-deposited weld metal microstructure predominantly consisted of acicular ferrite with various quantities of grain boundary ferrite, ferrite with second phase, and polygonal ferrite. Minor constituents of martensite-austenite (M-A) microphase were also found to exist between acicular ferrite laths and at the grain boundaries.

Sundaram *et al.* [54] compared two different welding processes, SMA and CO_2 welding with similar levels of heat input (1.6 kJ/mm for the SMA and 1.75 kJ/mm for the CO_2). They found the weld metal obtained by the SMA process to contain polygonal ferrite with some pearlite while the CO_2 weld metal microstructure not only contained polygonal ferrite but also acicular ferrite. Moon *et al.* [61], in their testing of HSLA-100 GMA welded with a heat input of 1.2 kJ/mm, discovered a fusion zone mainly consisting of lath ferrite with varying amounts of fine untempered lath martensite, as well as a bit of interlath retained austenite and oxide inclusions.

2.4 Weld Defects

Improper welding techniques or selection of welding parameters can cause defects to form in a weld that can influence the service performance of the components. One of the most common weld defects is porosity. Porosity, shown in Figure 2.6 (a), is a hole or void caused by gasses that have not escaped from the weld metal during solidification. Pieces of slag or other substances that become trapped in the molten steel during solidification are called non-metallic inclusions (Figure 2.6 (b)).

Incomplete (or lack of) penetration occurs when the penetration from welding is insufficient to complete the joint. When the weld and the surfaces of the base metal do not fuse the defect is called a lack of fusion. Both lack of fusion and penetration defects occur when the weld bead is not hot enough to penetrate the base metal and both lead to a weakened joint. Incomplete penetration and lack of fusion defects are illustrated in Figures 2.7 (a) and (b) respectively.

Undercutting occurs, when the parent metal melts at the side wall but is insufficient to fill in the groove. These undercuts generate a longitudinal notch along the edges of the weld that can lead to failure. HAZ (or cold) cracks are sometimes called “under-bead cracking” because they occur below the fusion boundary in the HAZ. HAZ cracks have been attributed to trapped hydrogen in the weld atmosphere and high cooling rates which promote formation of hard microstructures (i.e. martensite) which are prone to cracking [62].

2.5 Toughness

Toughness is a measurement of a material’s resistance to fracture, at a set temperature, when placed under a sudden impact loading. It can be defined as the amount of energy that can be absorbed by a material before breaking. There are many qualitative methods used to evaluate the impact energy required to break a notched specimen. Some of these tests include the Charpy impact test, the Izod impact test, and the drop-weight test. The Charpy impact test is the most common and most widely accepted impact test. The Charpy V-notch impact test is not without its limitations whereas its results are not

(a) 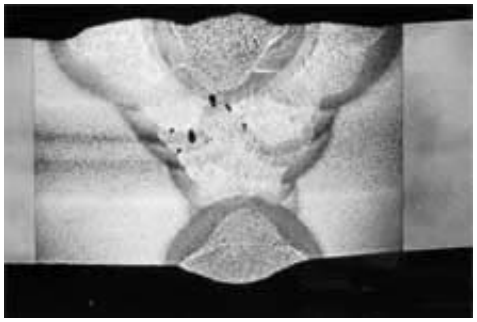 (b) 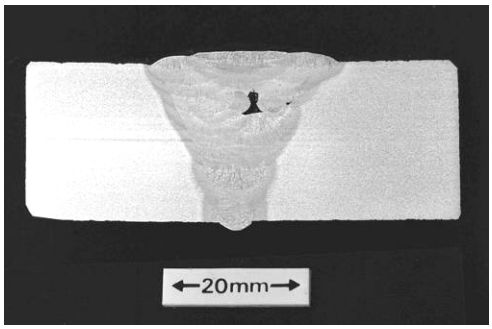

Figure 2.6. a) Porosity (Courtesy of TWI) [63] and b) Slag Inclusion (Courtesy of BB Welding Services) [64].

(a) 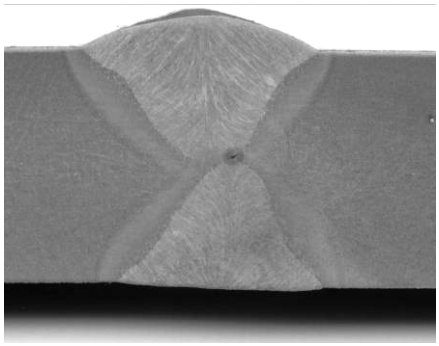 (b) 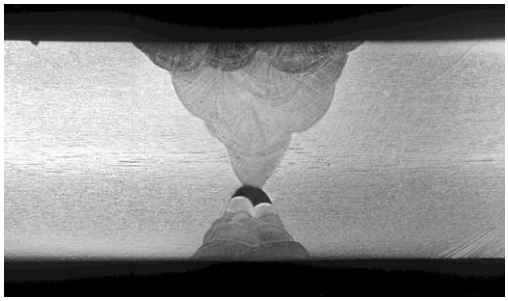

Figure 2.7. a) Incomplete Penetration and b) Lack of (Root) Fusion Defect (Courtesy of BB Welding Services) [64].

directly applicable for design and the ductile-to brittle transition observed is dependent on the specimen size. The Charpy impact test is however useful for determining the range of temperatures over which a material undergoes the ductile-to-brittle transition [65]. Also, because of the sensitivity of the Charpy impact test to changes in welding conditions it is an effective method for measuring the effect of welding parameters on the weld toughness [66].

It has been well established that Charpy V-notch impact toughness is inversely proportional to strength and therefore generally decreases with increasing tensile strength of a weldment [28]. The toughness of a welded joint depends on many factors such as the selection of alloying content of the base metal, filler metal and flux, weld process parameters, operating temperatures, and joint preparation. The processing history of the metal is also important as it determines how its microstructural features will develop.

The chemical composition and microstructure play a major role on the toughness of a material. Weld chemistry influences the notch toughness properties mainly by controlling the weld metal microstructure [22]. Increased carbon content, coarser grains, and a higher proportion of brittle inclusions will lower the toughness of steel and increase its hardness [31]. A fine grain structure is obtainable by additions of alloying elements as well as through treatments such as controlled rolling or normalizing [31]. The strength and toughness of weld metal can both be improved by grain refinement [28, 44]. For example, small additions of alloying elements such as aluminum induce fine grain sizes and, in turn, improve the toughness.

For example, Lee *et al*. [49] tested a conventional normalized steel, welded using the SAW method with a heat input of 5.0 kJ/mm. Testing standard Charpy V-notch specimens over a range of temperatures from -80 to -10 °C they found the Charpy impact energy to rise steadily with increased test temperature. Figure 2.8 displays this trend for the parent metal and the HAZ. It is obvious from this Figure that the CGHAZ exhibits much lower toughness than that of the base metal.

2.5.1 The Ductile-to-Brittle Transition

Generally, as operating temperatures are lowered the toughness of a material declines. Materials of the body-centered cubic (bcc) type, including carbon and most alloy steels, undergo a transition from ductile-to-brittle behavior as temperatures decrease [31]. The temperature at which the fracture behavior of the material changes from ductile to brittle is known as the ductile-to-brittle transition temperature (DBTT). This temperature correlates with fracture surfaces displaying 50% brittle and 50% ductile fracture characteristics. Below the transition temperature, with the presence of a stress concentration, even a small load can initiate a fracture and produce cracks that will easily propagate. The rate at which a material transitions from ductile to brittle behavior depends on many factors such as the chemical composition, structure, strength, and method of fabrication of the material [31]. Ideally this transition rate will be gradual.

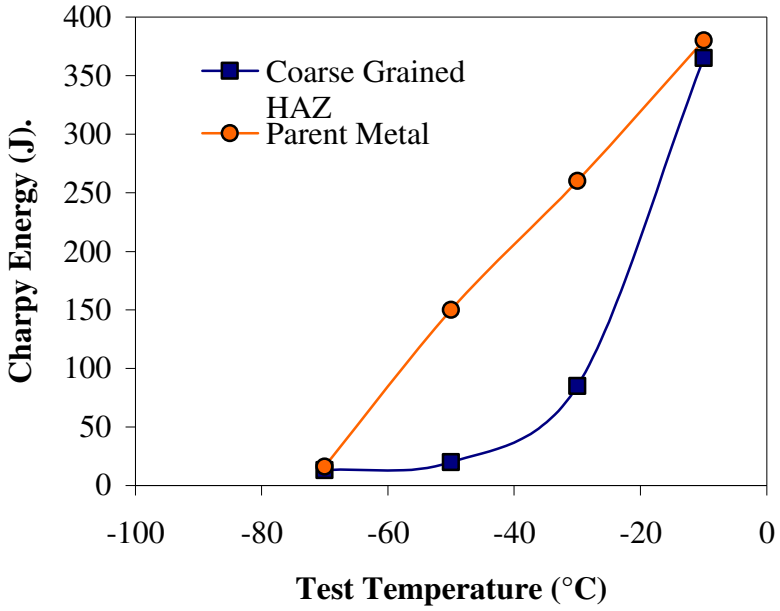

Figure 2.8. Charpy impact energies of base metal and HAZ as a function of test temperature for normalized steel [adapted from 49, not to scale].

2.6 Effect of Welding Process Parameters on Microstructure and Mechanical Properties of a Weldment

The selection of an optimum combination of process variables is essential when manufacturing with SAW in order to achieve welds of adequate quality and to control the dimensions of the heat-affected zone (HAZ) [67, 68]. The main variables that determine the weld characteristics include: 1) welding current, 2) type of flux and particle distribution, 3) welding voltage, 4) welding speed, 5) electrode size, 6) electrode extension (or stick-out), and 7) type of electrode.

Most studies of the effect of welding parameters on the impact toughness of steels focus on the effect of welding parameters combined in the form of heat input. According to Basu *et al*. [2], studying the properties combined together in this way does not properly assess the effects of each individual welding parameter such as current and speed. They hypothesized that the effects of variation of welding current and speed may result in subtle variations in microstructure, which could lead to mechanical properties ranging from highly desirable to highly detrimental even when welding with the same heat input. From their investigation they found considerable variations in the bead morphology and

weld microstructure occurring under identical heat input but with different combinations of current and travel speed. They attributed this to the differences in the microstructural features and the weld bead morphologies. Differences in the weld bead morphologies may lead to variations in weld cooling rates, which affect the microstructural development. For this reason it is important to study not only the effect of the combined heat input, but also the effect of the individual welding process parameters. The following sections discuss the literature on the effect of heat input and welding speed on the mechanical properties of steels.

2.6.1 Effect of Welding Speed

The welding speed affects the weld quality and toughness, governs production rates, and affects the rate of heat input. Welding speed and heat input are inversely proportional whereas increasing the welding speed decreases the heat input.

In 1983 Bhole & Billingham [42] studied the effect of heat input on the impact toughness of the HAZ of different HSLA steels. In their testing they varied the heat input by changing the welding speed with a constant welding current and voltage. They found a general deterioration of maximum HAZ hardness and toughness with increased heat input (or slower welding speeds) and associated this deterioration to the formation of "high-temperature transformation products such as proeutectoid ferrite, Widmanstätten ferrite, and upper bainite" [42].

Yang [16] studied the effect of welding speed with different amounts of current on submerged arc welded SA516 Gr. 70 and A709 Gr. 50. He reported increased hardness in both the WM and the HAZ with higher heat input (slower welding speeds) due to a higher fraction of hard phases such as bainite and martensite. He also found an increase in the WM toughness with increased welding speed, which was attributed to the finer grain size produced with lower heat inputs.

Yongyuth *et al.* investigated the influence of submerged arc welding speed on the weld toughness of a C-Mn steel, for a constant voltage and welding current [69]. A deterioration of toughness resulted with increases in welding speed from 6.7 to 8.3 mm/s

(30 V, 600 A) but marginally improved upon further increase as shown in Figure 2.9. This trend occurred even at subzero temperatures. They attributed the decrease in toughness with welding speed to an increase in the dendrite content in the weld metal and the subsequent small improvement to the decrease in area fraction of dendrites. Lack of significant change in the hardness and chemical composition, even with a wide variation in dendrite content, indicated that the microstructure was essentially unchanged. Thus they concluded that the 'macrostructure', or dendrite content, was the main parameter influencing the toughness.

Murti *et al.* [62] varied the heat-input rate by employing different welding speeds ranging from 4.2 to 10 mm/s (or heat inputs 1.9 to 0.8 kJ/mm). At all heat inputs they found the WM to be austenitic with 5-10 % ferrite. With a faster welding speed (10 mm/s) and low heat input (0.8 kJ/mm) they found the ferrite to be predominately acicular ferrite, while the slower speeds mainly produced other types of ferrite such as vermicular ferrite (1.2 kJ/mm) and skeleton ferrite (1.6 kJ/mm). They also reported an increase in hardness in both the WM and HAZ with faster welding speeds (or reduced heat input) as seen in their data in Table 2.1. These results correlate with the findings of Yang [16] and with Bhole *et al.* [42] for the HAZ. Bhole *et al.* attributed the reduction in HAZ hardness with increased heat input to the formation of high temperature products like proeutectoid ferrite, WF, and upper bainite. Murti *et al.* concluded that in all cases studied the maximum hardness value occurred in the HAZ at the fusion-zone boundary. The hardness decreased from the HAZ to the PM to the WM. They attribute the higher hardness of the HAZ to the higher rates of cooling due to a 'chilling effect' from the adjacent base metal, which would produce lower transformation temperature products. Moon *et al*. [61] also found the HAZ as the hardest region in each of the weldments they examined regardless of base metal, filler type or heat input. However, they found the hardness to peak midway through the HAZ rather than adjacent to the fusion boundary. In contrast, Sundaram *et al.* [54] observed a slight increase in hardness with higher heat inputs in their CO_2 weldments of Tisten 55. They found the highest hardness on the HAZ side adjacent to the weld interface and attributed it to the lath martensitic-like structure in this area.

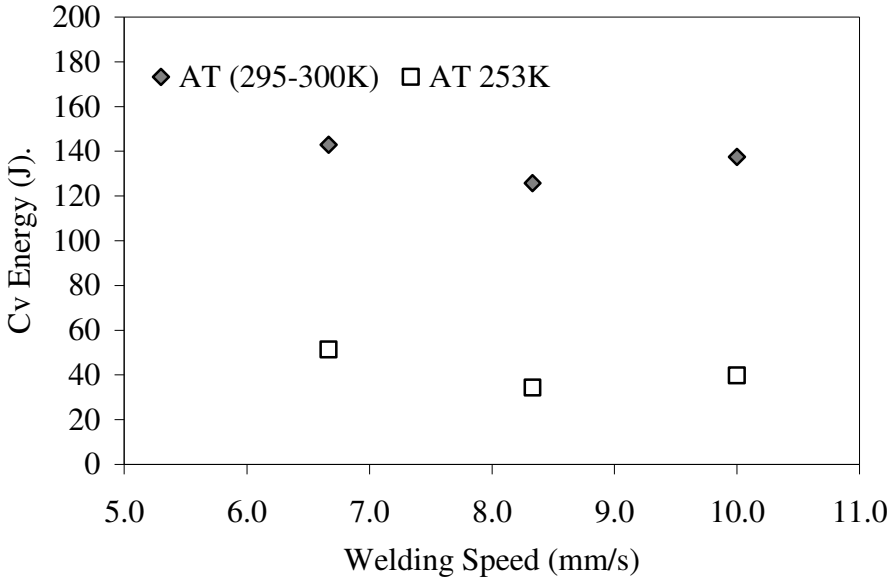

Figure 2.9. Effect of welding speed on impact toughness of the as-welded, transverse oriented specimens as influenced by temperature [adapted from 69].

Table 2.1. Variation in hardness with heat input rate [adapted from 62].

No.	Heat input (kJ/mm)	Mean hardness of fusion zone (Hv)	Highest hardness value in HAZ (Hv)
1	0.8	211	541
2	1.2	208	502
3	1.4	202	460
4	1.6	198	426

2.6.2 Effect of Heat Input

Heat input is a relative measure of the arc energy transferred from the electrode to the base metal during welding. It is an essential parameter as it controls the cooling rate, which in turn affects the microstructure and mechanical properties of the weld and the HAZ. The heat input per unit length can be calculated as [62, 70]:

$$H = \frac{EI}{1000\,S} \tag{2.1}$$

where H = heat input (kJ/mm), E = arc voltage (volts), I = current (amps), S = travel speed (mm/s).

The rate of heat increase, cooling rates, maximum temperatures, and the duration spent at elevated temperatures can vary considerably between the different welding processes [71]. For this reason the measure of heat input is more useful in comparing weld parameters for a given welding process than for comparison of different welding processes [70].

Since the welding speed, current, and voltage all control the heat input, many researchers have included variations of these parameters into studies of the effect of heat input on toughness. Most studies have involved varying combinations of more than one parameter to vary the heat input but have not focused on any one of these parameters individually. This section describes the research of this type.

In an attempt to increase fabrication productivity, researchers have made many attempts to discover the ways to weld at higher heat inputs while maintaining satisfactory mechanical property requirements (particularly the HAZ toughness). Higher heat inputs decrease the cooling rate of the weld for a given base metal thickness.

The relationship between the heat input and cooling rate can be described by a proportionality function as follows [70]:

$$R \alpha \frac{1}{T_O H} \tag{2.2}$$

where R = cooling rate (˚C/sec), T_O = preheat temperature (˚C), H = heat input (kJ/mm).

The cooling rate is a primary controlling factor in determining the final microstructure of both the weld metal and heat-affected zone (HAZ) [70]. Slower rates of cooling (or higher heat inputs) that prolong the weld metal cooling result in larger grains, which is detrimental to the mechanical properties of the metal [12]. Adjustment of the cooling rate can be used to control the level of microstructural refinement. Increased cooling rates (or decreased heat input) corresponds with more a refined, or finer-grained

microstructure. Despite the general trend of an inverse relationship between strength and toughness the mechanism of microstructural refinement both strengthens and toughens the material and is therefore a particularly attractive strengthening mechanism [10, 12, 27]. Microstructural refinement has also been beneficial in reducing the DBTT of a material [10]. Fine-grained structures generally correspond with low temperature transformation products, however, the higher the cooling rate the greater the chance of forming low temperature transformation products, such as martensite, which have higher strength but lower toughness [10, 12].

Researchers have generally arrived at the same conclusions regarding the effect of increased heat input. Most studies have shown that an increase in heat input, or a decrease in cooling rate, reduces the WM and HAZ toughness [3, 12, 16, 21, 42, 45, 46], hardness [14, 16, 21, 30, 42, 46, 48], and the yield and tensile strengths [14, 30, 46, 72].

Deterioration of toughness of a weldment, with additional heat input, has been credited to coarsening of the microstructure [3, 45, 46, 72] and formation of high temperature transformation products such as proeutectoid ferrite, Widmanstätten ferrite, and coarse or upper bainite [42]. Other unfavourable microstructural features which may degrade toughness include coarse grain boundary ferrite [17, 45], primary ferrite, side plate ferrite (SPF) [46], martensite-austenite (M-A) constituents [21, 45], and aligned ferrite [45]. Higher heat input rates also widen the HAZ zone [3, 14, 43, 45, 46, 48], increasing the chance of its inclusion in the fracture path. McGrath *et al*. [3] and Smith *et al*. [14] both attributed significant reduction in notch toughness at high heat inputs to the increased width of the CGHAZ. Their philosophy was that the wider the embrittled CGHAZ the more it will participate in the fracture process.

Reduction of hardness, at higher heat inputs, has normally been attributed to coarsening of the microstructure [28, 46, 72], and increases in the volume fraction of soft materials such as ferrite [9, 17, 46]. Increased heat input and coarsening of the microstructure also correspond with decreased tensile and yield strength but enhanced ductility due to the softening with the increase in grain size [3, 46, 72].

Increasing heat input has also been reported to increase the transition temperature through microstructural coarsening [10, 45] and to coarsen the prior austenite grains [13, 45, 46], which particularly affects the CGHAZ [21, 46]. Robino et al. have also found that lower heat inputs notably lower upper shelf energy due to the low transformation temperature products in the HAZ [40].

Vilpas *et al.* [13] reported a weld metal of mainly acicular ferrite with less than 10% of other microstructural constituents consistently over various heat inputs in both SMA and SAW welds of N-A-XTRA 70 (equivalent to ASTM A514). In the CGHAZ they found the microstructure to consist of a combination of martensite and lower bainite. They reported that there was no discernible effect of heat input (from 1.7 to 3.0 kJ/mm) on the microstructure, strength or ductility of the weld metal. However, an increase was noted in the austenite grain size of the HAZ of the SMA welds. Their results showed that toughness (both impact and COTD fracture toughness) decreases with increases in heat input. At the fusion boundary (HAZ), Figure 2.10 shows that the lower heat input produced a transition curve that was superior to the higher heat input. They concluded that the heat input should be kept low to achieve good impact properties at the fusion boundary of the steel.

Huang *et al*. [17] found in their studies of SAW of SA516 Gr. 70 steel weldments that increased heat input gave rise to growth in the volume fraction of GF in the weld metal while a reduction in heat input was found to increase the proportion of acicular ferrite in the weld metal. They saw that change in heat input did not change the weld metal microstructural constituents but the relative amounts of each. Increasing the heat input from 1.5 to 4.5 kJ/mm, revealed a coarsening of the predominantly Widmanstätten ferrite structure in the grain-coarsened HAZ.

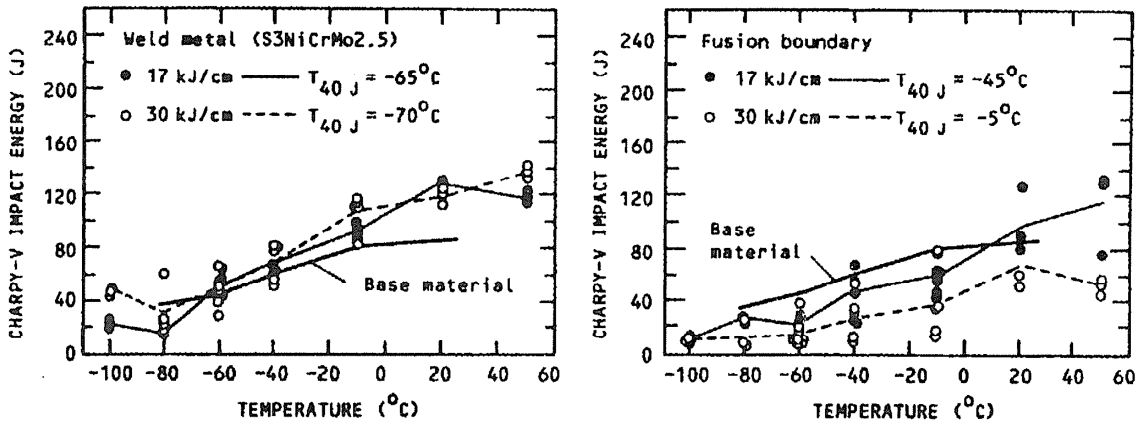

Figure 2.10. Charpy-V transition curves for the weld metal and fusion boundary and the corresponding transition temperatures (T40 J) for the SAW-joints (Courtesy of VTT, Technical Research Centre of Finland) [13].

In their study of CO_2 welding of Tisten 55, Sundaram *et al.* [54], with an increase in heat input from 1.75 to 2.55 kJ/mm, produced results contradictory to most other studies. They reported that the higher heat input consistently resulted in increased fracture toughness (CTOD) values in both the WM and HAZ (60 % and 70 % respectively) but only a marginal decrease in the yield and tensile strengths. The lower heat input HAZ contained fine ferrite and a martensite-type structure whereas the HAZ from the higher heat input contained more lath martensite-type structure and acicular ferrite and lower polygonal ferrite content.

Smith *et al.* [14] found a slight decrease in the amount of acicular ferrite in the weld metal with increased heat input. With the decrease in acicular ferrite they also saw a corresponding increase in other minor constituents such as grain boundary ferrite, ferrite with second phase and polygonal ferrite. They reported that the notch toughness behaved differently in each region of the weld. In the submerged arc weld metal they found a trend of higher notch toughness with an increased heat input despite the coarsening of the microstructure. Figure 2.11 shows how the Charpy impact energy for the CGHAZ of HSLA-80 decreased with increasing heat input. They attributed the decrease in toughness to an increased proportion of CGHAZ taking part in the fracture and a change in the microstructure of CGHAZ from low-carbon martensite/bainite to coarse upper bainite. Their conclusion was that higher notch toughness is expected at

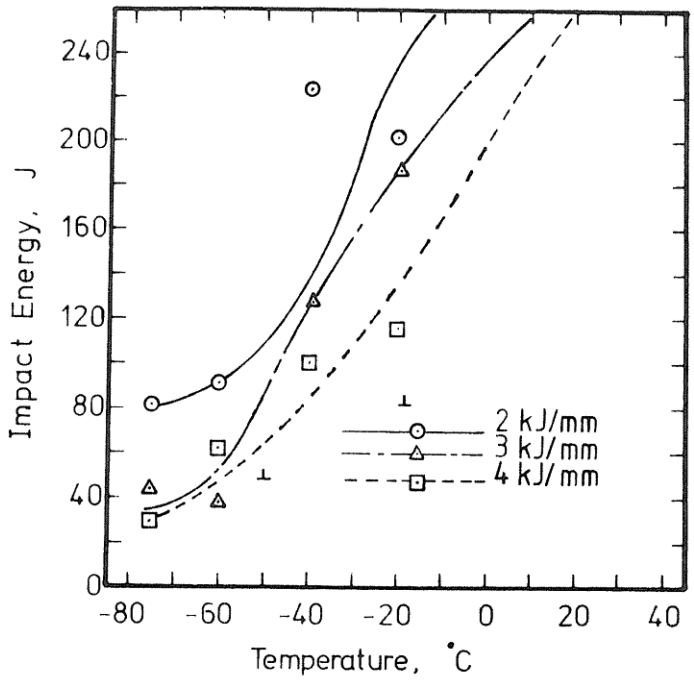

Figure 2.11. Charpy impact energy for the CGHAZ of HSLA-80 with increasing heat input (Courtesy of Welding Journal, American Welding Society, Miami, Fla.) [14].

lower energy inputs because of the higher proportion of fine weld metal structure. They also found an increase in energy input to lower the yield strength, which was caused by the slight coarsening of the weld metal microstructure. In contrast, McGrath *et al.* [3] reported no change in the microstructure of the CGHAZ for HY-80 under a variety of heat inputs (2 and 4 kJ/mm) as it remained completely martensitic with intergranular discontinuities.

2.7 Effect of Welding Process Parameters on Weld Geometry of a Weldment

In SAW, the weld bead shape plays a role in determining the mechanical properties. The weld bead shape can be used in quality performance evaluation for a weld according to the process parameters. Weld quality is primarily determined by the weld bead geometry, which depends greatly on the amount of filler metal deposited. The weld geometry parameters used to measure the weld quality are illustrated in Figure 2.2.

The penetration, P, is the depth to which molten metal deposits into a joint. Penetration determines both the size and strength of bead that will hold the joint together [73]. The

mixing ratio of the filler and parent metal are influenced by the penetration [59]. The depth of penetration depends on the current, voltage and the cross-sectional area of the bead. Manipulation of the electrode can be used to increase or decrease the penetration. For example, an increase in the distance between the electrode and the weld increases arc flaring, which consequently leads to a widening of the bead but reduced penetration. Deepened penetration occurs with a higher current level and the subsequent increased arc intensity [73].

In Figure 2.2, *P* is the penetration (of the deposited metal into the joint), *b* is the bead width (indicating the diameter of the deposited metal), *R* is the reinforcement (the height of the weld bead above the surface of the material), and *w* is the width of the heat-affected zone (HAZ).

2.7.1 Effect of Welding Speed

According to the findings of many researchers, the welding speed is the main factor next to current that governs the heat input and the HAZ size [67, 74] and the joint penetration [75]. As the heat input and welding speed are inversely proportional, an increase in the weld speed will result in a lower heat input. Hence as the welding torch travels at lower speeds the heat input will be greater. The added heat conducts out further from the fusion zone to the parent metal increasing the width and grain size of the HAZ [74]. Gunaraj and Murugan found that the weld interface (WI) and the different regions of the HAZ are all narrower with faster welding speeds [67] as less of the parent metal is affected by the elevated temperatures. The results of Benyounis *et al*. [74] confirm that widening of the HAZ occurs at slower welding speeds.

Studies have generally found a decrease in percentage of dilution (*D*), *R*, *b*, and *P* with increased welding speed [16, 68, 76, 77]. Increase in the speed reduces the heat input and therefore melting a smaller portion of the base metal reducing the metal deposition rate on the bead. This lower heat input and metal deposition rate cause a reduction in the size of weld pool and all the bead parameters [68]. The American Welding Society (AWS) [75] and the Lincoln Electric Company [78] confirm the lower *R*, *P*, and *b* with faster speed. Karadeniz *et al*. [79] saw an increase in the penetration with increased

welding speed (in GMAW) up to a certain optimum point, after which they found a decrease. This increase in *P* until an optimum speed and maximum penetration are achieved with subsequent decreases in *P* is consistent with the AWS [75].

Excessive travel speeds may cause weld defects such as porosity, poor bead appearance, undercutting, arc blow, incomplete penetration, and a lack of fusion between the deposit and the base metal [75, 78]. Slow travel speeds allow more gases to escape before cooling thereby reducing the occurrence of porosity defects. On the other extreme, very slow travel speeds can also cause problems such as rough, convex, or large weld beads that are susceptible to cracking, spatter, or slag inclusions [75, 78].

2.7.2 Effect of Heat Input

The size of the weld bead is generally proportional to the amount of heat input supplied. Increased supply of energy from the arc will promote electrode and base metal melting and produce a larger bead. Additional heat input also reduces the cooling rate for a given thickness of base metal. The metal cooling rate plays a primary role on the development of the microstructure in both the weld and the HAZ.

Much research has been focused on the role of heat input on the geometry of the weld bead and the heat-affected zone. The general consensus of studies in this area has concluded that excessive heat input results in wider HAZ dimensions [58, 45, 46, 48, 67, 74]. The size of the HAZ indicates the extent of which welding heat has altered the structure of the base metal. A wide HAZ may indicate deterioration of the mechanical properties correlating with low-impact strength, particularly in high-heat input submerged arc welds [67]. For this reason the selection of appropriate process variables is essential in managing the HAZ dimensions and the weld integrity.

The heat input is inversely proportional to the welding speed. This suggests that a reduction in the welding speed (with current and voltage constant) will cause an increase in the heat input and will consequently cause the material to cool at a slower rate. High heat input results in a larger molten pool, which remains liquid for a longer period of time. Consequently, there is increased heat flow into to the metal, enlarging both the

individual grains and the width of the HAZ [58, 67]. At low heat inputs, with faster welding speeds, there will be less time for wasteful heat flow. The larger molten pool from the increased heat input also results in the achievement of deeper penetration into the joint [74].

2.8 Flux and Electrodes

Flux and electrode combinations are chosen to obtain certain mechanical properties. The flux used in SAW is a granular substance which contains various proportions and mixtures of oxides such as manganese, silicon, magnesium, titanium, aluminium, calcium, zirconium, and compounds such as calcium fluoride. Flux can be classified by the basicity index (*BI*), which can be determined by the following formula [1] expressed in weight percent (wt. %):

$$BI = \frac{CaO + MgO + BaO + SrO + Na_2O + K_2O + Li_2O + CaF_2 + \frac{1}{2}(MnO + FeO)}{SiO_2 + \frac{1}{2}(Al_2O_3 + TiO_2 + ZrO_2)} \quad (2.3)$$

Flux can be acidic, neutral, semibasic, or basic. When the basicity index is less than 1 a flux is deemed acidic, between 1 and 1.5 it is neutral, semibasic between 1.5 and 2.5, and basic when greater than 2.5 [1]. Acid flux produces more inclusions and increases oxygen content in the weld metal; these have both been found to be detrimental to the material toughness. Basic flux produces the lowest levels of oxygen but provides poor welding performance. As a compromise, semibasic flux is a good choice for adequate weld performance and low-temperature toughness.

Figure 2.12 illustrates how the notch toughness of the metal is affected by the basicity index of the flux as found by Thomas *et al*. [1]. In general the notch toughness is superior with a higher or more basic flux. For example, McGrath *et al*. [22] found that welds performed on SA516 Gr. 70 using a higher basicity flux showed good toughness by lowering the inclusion content.

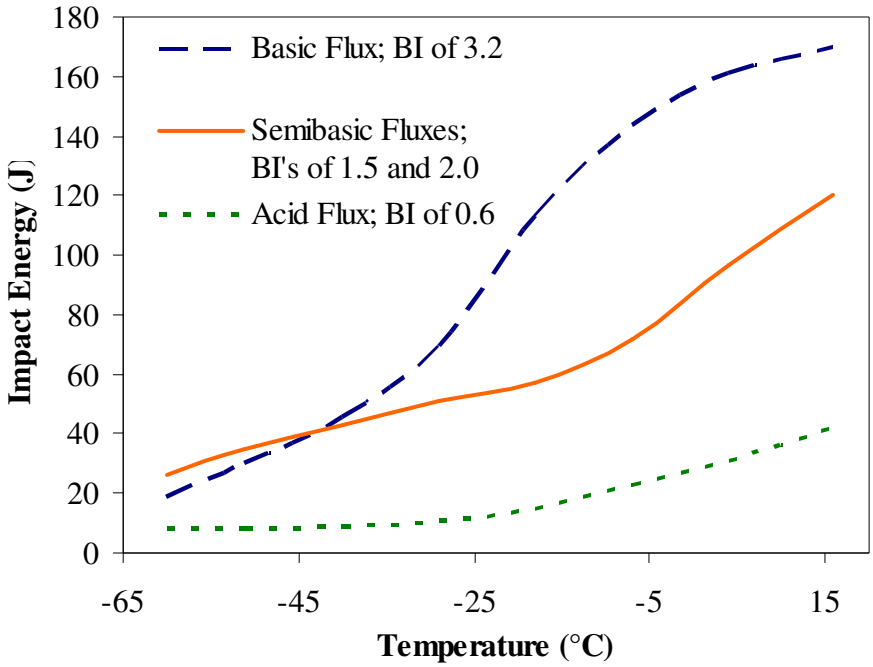

Figure 2.12. Comparison of flux basicity index [adapted from 1, not to scale].

3 MATERIALS AND EXPERIMENTAL PROCEDURE

This chapter provides a description of the materials and experimental techniques that were used in this investigation. Various difficulties were encountered during the testing. The tool recommended in ASTM E23 for the lateral expansion measurements of the fractured Charpy specimens was not available so an improvised method was used for these measurements as described in Section 3.3.4. Difficulties also occurred in estimating the exact temperature the Charpy specimens were tested at due to the lapse of time required to remove the piece from the chiller or heater and place it into the tester. Weld defects were found in many of the Charpy specimens. Specimens with weld defects could not all be ignored due to the high percentage of specimens that contained defects. Only a representative sample was taken from each welded plate to measure the weld geometries due to machining limitations. The plate was assumed to be consistent across its length.

3.1 Materials

The material studied was ASME SA516 Grade 70 otherwise known as ASTM A516 Grade 70 (UNS Number K02700), carbon-manganese steel. The material was supplied as normalized, hot rolled steel plates measuring 17 mm x 915 mm x 122 mm. Its composition and mechanical properties, as supplied, are shown in Tables 3.1 and 3.2 respectively. Chemical composition of the steel, flux and electrode were based on test certificates provided by Hitachi Canadian Industries (HCI) Ltd., Saskatoon, Saskatchewan. The composition was determined by ISPAT SIDEX SA according to the EN10204/3.1B standard.

3.2 Weld Procedures

The submerged arc welding (SAW) technique was used by Hitachi for single-pass welding of the test plates for this research. The 17 mm thick plates were butt-welded, a single pass on each side, with no bevelling, preheat or post-weld heat treatment.

Table 3.1. Chemical composition of SA516 Grade 70.

Material	C	Mn	P	S	Si	Al	Cu	Ni	Cr	Mo	Ti
SA516 Gr. 70	0.22	1.14	0.019	0.008	0.24	0.054	0.02	0.01	0.02	0.002	0.004

Table 3.2. Material properties of SA516 Grade 70 from the ASTM A516 standard.

Material/Properties	TS (MPa)	YS (MPa)	EL (%) (200 mm) gauge length	EL (%) (50 mm) gauge length
SA516 Gr. 70	485-620	260	17	21

Using an ESAB (Elektriska Svetsnings-Aktiebolaget or Electric Welding Limited Company) welding machine, the first side was welded at room temperature then the plates were flipped and welded on the other side. On account of this technique, the temperature of the plate for the second side weld was much higher than that of the first. This difference in temperature produced variations in both the weld geometry and hardness of the two welds. Table 3.3 outlines the welding procedure of the welds tested.

A preliminary MIG weld pass was performed on the side of the plate correlating with the second SAW pass. The function of this MIG pass was to tack the plates together as a seal weld in order to prevent the puddle from running away through the gap between the plates. Measurement of the length of time to cover a known distance was used to validate the accuracy of the speed shown on the digital readout of the ESAB machine. The digital readout was found to be out by 0.423 mm/s (1”/min). This machine error was then taken into account for all successive welding.

The electrode stickout, or the distance between the contact tip and the base metal was measured to be 28 mm and was kept constant for the welding of each of the three plates. The polarity was DC or electrode positive. The flux and electrode used for the welding were OK Flux 10.72 and EM12K – 4.0 mm (5/32”) diameter, respectively. The chemical compositions of the electrode and deposited weld metal (obtained in ESAB

testing) are given in Table 3.4, while that of the flux is shown in Table 3.5. ESAB Welding and Cutting Products material test certificates were provided by Hitachi.

The OK Flux 10.72 used in the welding process is an agglomerated aluminate-basic flux that was designed for applications requiring good low temperature toughness. It is a flux that adds manganese to the weld deposit and has a very high current-carrying capacity. Applications in which it is used include pressure vessels production and general construction exposed to impacts at -51 ˚C (-60˚F) [80].

Table 3.3. Welding parameters.

Weld #	Weld Current (A)	Weld Voltage (V)	Weld Speed (mm/s)	Heat Input (kJ/mm)
PV-2	700	35	9.3	2.6
PV-3	700	35	12.3	2.0
PV-4	700	35	15.3	1.6

3.3 Experimental Procedure

3.3.1 Mechanical Testing

In order to obtain a good understanding of the mechanical properties of the different welds, a variety of mechanical tests were performed, including Charpy impact testing, hardness measurements, and tensile testing. Tensile testing was performed by colleague Mr. James Amanie.

3.3.2 Specimen Preparation

The dimensions of a standard Charpy test specimen according to ASTM A370 [81] (or ASTM E23 [82]) are shown in Figure 3.1 (a) and (b). Notches were cut in the centre of the weld metal and in the heat-affected zone according to AWS (American Welding Society) D1.1 specifications [83] for specimens with a single V-groove of thickness greater than 12 mm. A schematic of the method for cutting Charpy specimens is shown in Figure 3.2.

Table 3.4. Chemical Composition of electrode and deposited weld metal.

	Chemical Composition (wt %)						
	C	Mn	Si	S	P	Cu	Other
Electrode (EM12K OK 10.72)	0.1	0.99	0.24	0.01	0.006	0.13	< 0.50
Deposited Weld Metal	0.08	1.6	0.31	0.009	0.18		

Table 3.5. Chemical composition of flux [80].

Chemical Composition (Nominal %)	
$SiO_2 + TiO_2$	20%
$Al_2 + MnO$	30%
$CaO + MgO$	25%
CaF_2	20%
Basicity Index : 1.9	

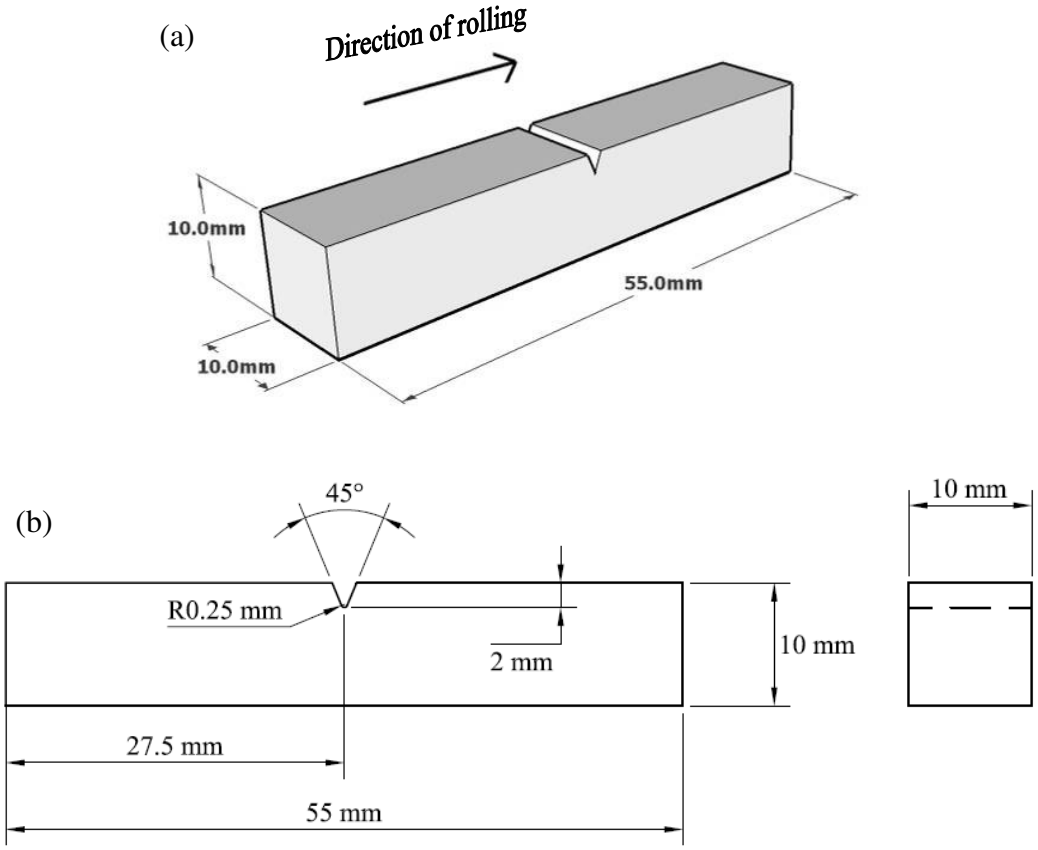

Figure 3.1. (a) 3D illustration of test specimen, (b) Detail drawing of specimen dimensions.

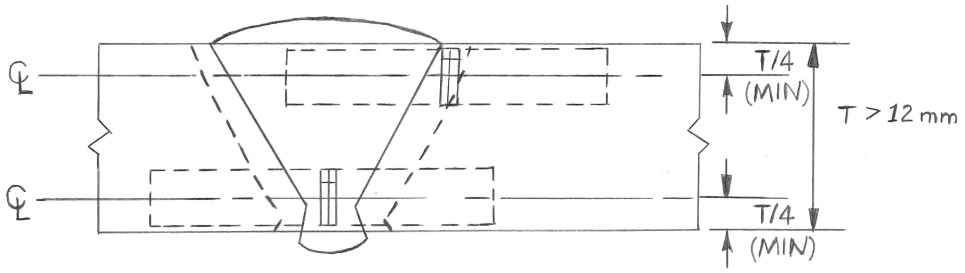

Figure 3.2. Sketch of Charpy weld specimens cutting locations [adapted from 83].

In order to prepare the machined specimens for cutting the notches, the first step was to etch the specimen to display the weld features and the HAZ. The specimens were etched with 2% nital until the weld zones were visible (about 30 seconds). Notches were cut transverse to the rolling direction using a broaching machine in the weld metal and in the HAZ for each of the welded plates. Due to the curvature of the weld and HAZ profile, the notches in the HAZ notched specimens were placed such that each notch ran through as much of the HAZ as possible.

Standard rectangular tensile specimens were prepared in accordance with ASTM A370. Approximate dimensions of a typical tensile specimen are shown in Figure 3.3.

3.3.3 Charpy Impact Testing

Charpy impact testing was performed on weld specimens to determine the effect of temperature and welding parameters on the impact toughness of the steel. The number of specimens tested was dependent on the amount of data required to complete a clearly defined transition curve. The number of specimens tested ranged from 26 to 31 for each curve; these are outlined in Table 3.6. The Charpy impact tester used for the testing was a RIEHLE Charpy Impact Tester.

The tests were performed according to ASTM E 23 (or A370) on standard-sized V-notched specimens at temperatures ranging from -190 °C to 100 °C to measure the impact toughness (or impact energy). The test specimens were brought to the required temperature by holding them in a liquid medium at the test temperature for at least 5 minutes.

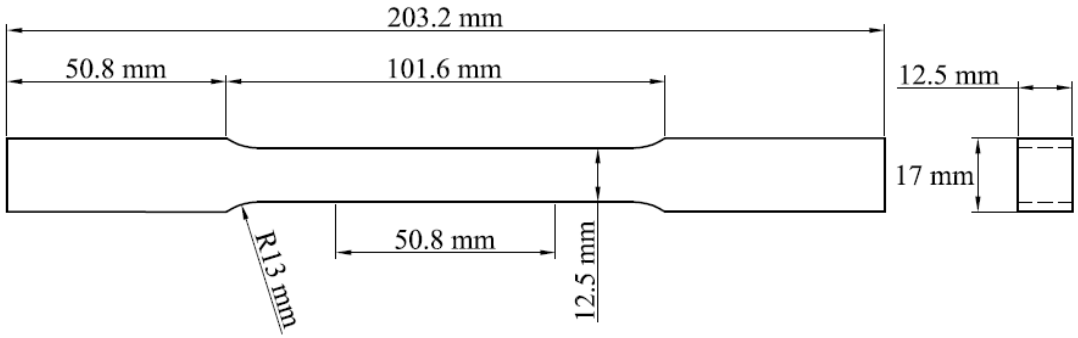

Figure 3.3. Sketch of typical tensile specimen.

Table 3.6. Number of Charpy V-notch specimens tested.

	Location of Notch	
Weld Speed (mm/s)	HAZ	WM
9.3	27	26
12.3	31	30
15.3	31	30
PM (Transverse)	27	
PM (Longitudinal)	27	

To obtain cryogenic temperatures, the specimens were either immersed in a mixture of liquid nitrogen and methanol or in a bath of methanol in a chiller. High temperatures were obtained using a beaker of water warmed on a hot plate. The test specimen was then carefully centred in the anvil of the Charpy impact tester and the pendulum released to break the specimen. If the pendulum was not released within 5 seconds of specimen removal from the liquid media, it was returned once again to the bath to bring the specimen back up to the correct temperature.

The impact energy absorbed for each tested specimen was recorded to the nearest ft-lb and later converted to joules. Before testing the next specimen, the matched pieces of each broken specimen were recovered for subsequent fracture surface observation(s). The absorbed energy obtained from various test temperatures within the range of -190 ºC to +100 ºC (accurate to ± 5 ºC) were plotted to obtain a transformation curve.

Representative fracture surfaces from the Charpy impact specimens for different temperatures were lined up and photographed using a digital camera.

The ductile-to-brittle transition temperature (DBTT) was determined by finding the temperature at which the energy absorbed falls halfway between the points required to completely fracture a ductile specimen and that required to completely fracture a brittle specimen. The DBTT found using the Charpy impact test and the average energy method is called the Impact Transition Temperature (ITT). After plotting the absorbed energy as a function of temperature the points are fit with a smooth curve. The upper shelf and lower shelf energies are determined from the curve and the midpoint or average energy is determined. Next, a line is drawn from the average energy to the curve then down to find the ITT. This temperature depends on the shape of the curve and must be obtained graphically as shown illustrated in Figure 3.4. Another method for determining the DBTT is by using the fixed energy method. In this method the temperature at which the average absorbed energy is a predetermined value (often 27 J) is found graphically from the Charpy curve.

Other methods to determine the DBTT consist of measuring the lateral expansion (or plastic deformation) the specimens incurred at each test temperature or by the fracture appearance method where the transition temperature is determined by finding the temperature for which the impact specimen shows a fracture surface that is half brittle – half ductile.

3.3.4 Lateral Expansion

The lateral expansion of a broken specimen gives an indication of the ductility of the material. When a ductile metal is broken it undergoes plastic deformation before fracture. The amount of deformation is measured and is recorded as a percentage lateral expansion. The lateral expansion of the fracture surface of each broken Charpy V-notch specimen was measured according to ASTM. Measurement of lateral expansion is also used as an alternative method for determining the transition temperature. The procedure is based on the fact that protruding shear lips are produced (perpendicular to the notch)

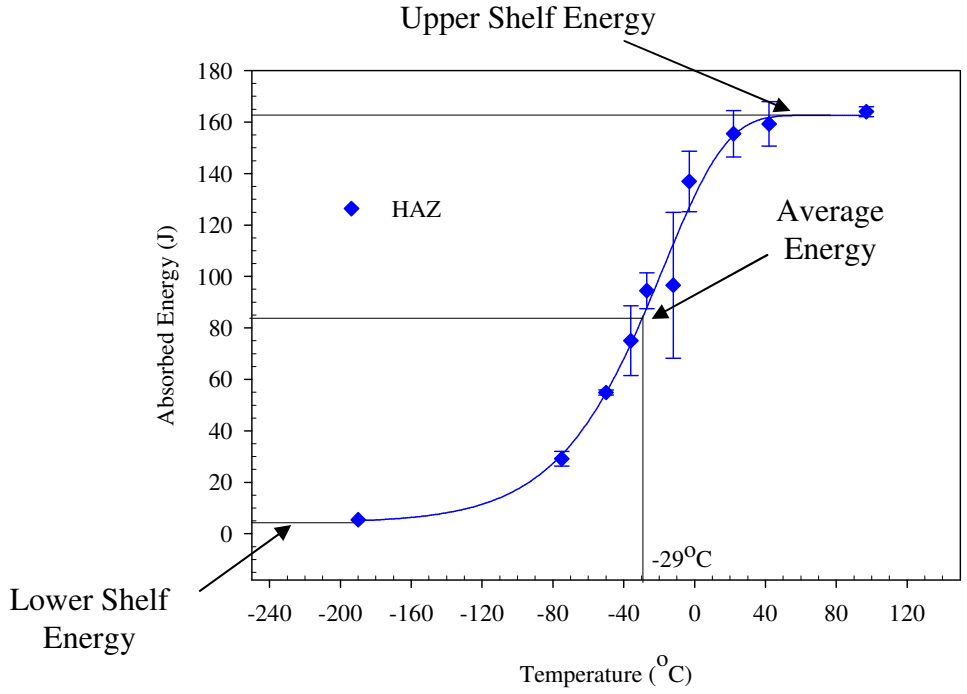

Figure 3.4. The average energy method for calculating the impact transition temperature (ITT).

on either side of each broken specimen. Larger protrusions correlate with greater ductility [65].

The measuring device recommended in ASTM E23 was not available for measuring the lateral expansion so an alternative method was used. The lateral expansion of the fracture surface of each specimen broken during the Charpy impact test was obtained by measuring the largest expansion of the fracture surface over the two pieces of the broken specimen, as illustrated in Figure 3.5. Vernier callipers were used in order to obtain a reading accurate to ± 0.01 mm. The largest expansion readings were recorded and the original, undeformed width of the specimen was subtracted in order to calculate the lateral expansion using Equation 3.1 described as

$$Lateral\ Expansion\ (\%) = \frac{W_{\max} - W_0}{W_0} \times 100 \qquad (3.1)$$

where W_{max} is the maximum deformed width of the broken specimen including both halves and W_o is the original width of the specimen.

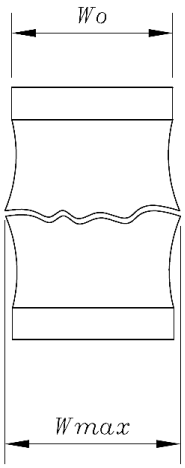

Figure 3.5. Illustration of measurements for calculating lateral expansion.

The percentage of lateral expansion was then plotted as a function of test temperature and the ductile-to-brittle transition temperatures (DBTTs) were determined from the graph. The method used was much the same as that used for with the Charpy energy readings. Figure 3.4 describes the method except that in this case the vertical axis was lateral expansion instead of absorbed energy.

A second method for measuring the lateral expansion was used but was deemed inaccurate and therefore was not presented. In this alternative method, the largest protrusions of each end of the broken specimen were measured with respect to the undeformed width as recommended in the standard, i.e. A1, A2, A3, and A4 as illustrated in Figure 3.6. This was completed by scaling measurements from photographs of the fractured ends of the specimens using AutoCAD due to the unavailability of a measuring device like the one recommended in ASTM E23. Using Equation 3.2 the maximum lateral expansion was then calculated. This method was inaccurate due to the inability to determine the exact edges of the specimens from the pictures. It is not recommended that this method be used. Data plotted using this method is listed in Appendix E for reference.

$$Lateral\ Expansion = \max(A1, A2) + \max(A3, A4) \tag{3.2}$$

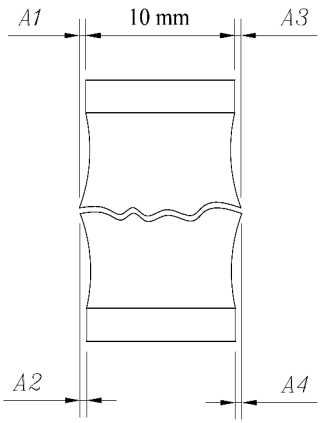

Figure 3.6. Illustration of measurements for calculating lateral expansion according to ASTM E23.

3.3.5 Microhardness Measurements

Hardness traverses were recorded by collecting microhardness measurements from the parent metal across the weld using a Mitutoyo MUK-H1 Vicker's Hardness Tester. Five rows of hardness measurements, 5 mms apart, were taken across the weld from parent metal to parent metal; see Figure 3.7 for an example. Each reading was measured with an indentation load of 300 g and a resident time of 15 seconds. Measurements were taken for the 1st pass welds of all 3 welding speeds but the 2nd pass welds were only measured for the 12.3 and 15.3 mm/s weld speeds due to time restrictions. These hardness measurements were taken across the weld not only to correlate with other properties but also to discover if any excessive hardening or softening of the joint has occurred. The hardness traverse therefore shows the variations in material hardness from the parent metal, heat-affected zone and weld metal.

3.3.6 Tensile Testing

Tensile specimens were prepared in accordance with ASTM A370. Three specimens of each weld speed as well as of the parent metal were tested. The Instron Universal Testing Machine Floor Model 550R was used for the testing of samples with a load of 5 kN a crosshead speed of 5 mm/min correlating with an initial strain rate of 0.098 min^{-1} calculated by Equation 3.3. The gauge length was 50.8 mm.

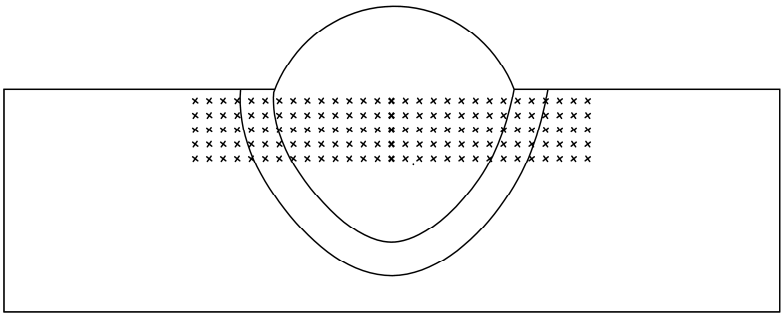

Figure 3.7. Illustration of hardness measurements.

$$Initial\ Strain\ Rate = \frac{Crosshead\ Speed}{GaugeLength} \tag{3.3}$$

3.4 Microscopy

3.4.1 Optical Microscopy

Optical microscopy was used to observe the microstructures of each of the 5 zones of the weldments. The samples were ground, polished and etched for about 30 seconds with 2% nital. Optical photographs were taken using a Nikon Optiphot metallurgical microscope and a Nikon D70 digital camera at 7 locations including the PM, WM of the first and second pass welds, PM/HAZ interface (or transition zone), HAZ/WM interface, interface of the top and bottom welds and the HAZ.

3.4.2 Scanning Electron Microscopy (SEM)

Scanning electron microscopy (SEM) was used to study the fracture surface of the Charpy Impact test specimens in order to investigate the proportions of ductile and brittle fracture on the surfaces. The fracture surfaces of the broken Charpy Impact specimens were cut off at about ¼ in thick using a diamond cutter and cleaned using an ultrasonic cleaner. They were then examined in a Philips 515 scanning electron microscope using an accelerating voltage of 20 keV and pictures were taken using a Polaroid camera. The mechanism of fracture was identified and related to the observed Charpy test results.

4 RESULTS AND DISCUSSION

This chapter presents and discusses the results found from the testing described in Chapter 3. The analysis will show the effect of the welding speed on the weld quality and properties of the SA516 weldment. Curve fit data is listed in Appendix G for reference. In all cases error bars shown in graphs of the experimental results represent the standard deviation for the data point. See Appendix H for numerical values of standard deviations not listed in this section.

4.1 Effect of Welding Speed on the Microstructure of SA516 Weldments

4.1.1 Microstructures of the Welded Joint

Typical microstructure for the as-received SA516 Gr. 70 steel is shown in Figure 4.1. This micrograph reveals the microstructure of coarse banded ferrite (F) and pearlite (P) of the rolled steel. The typical WM microstructure observed for the specimens, shown in Figure 4.2, consists of a columnar structure of ferrite including a large proportion of acicular ferrite (AF) with grain boundary ferrite (GF), and some Widmanstätten ferrite (WF). Yang [16] and Huang *et al*. [17] reported similar structures in their welds produced with SAW of SA516 Gr. 70 steel.

As discussed previously, the microstructure that forms in the coarse-grained region of the HAZ depends on various factors including the chemical composition, the peak temperature reached during the fusion process, and the rate of cooling. The peak temperature controls the austenite grain growth therefore determining the grain size. The rate of cooling controls the final microstructure that forms within the prior austenite grains once cooling is complete. The alloy composition plays a role in determining both the austenite grain size and the microstructure. The microstructure of the CGHAZ for a welding speed of 12.3 mm/s, shown in Figure 4.3, mostly consists of a conglomeration of bainite (upper bainite (BU), lower bainite (BL), ferritic bainite (BF)) with some

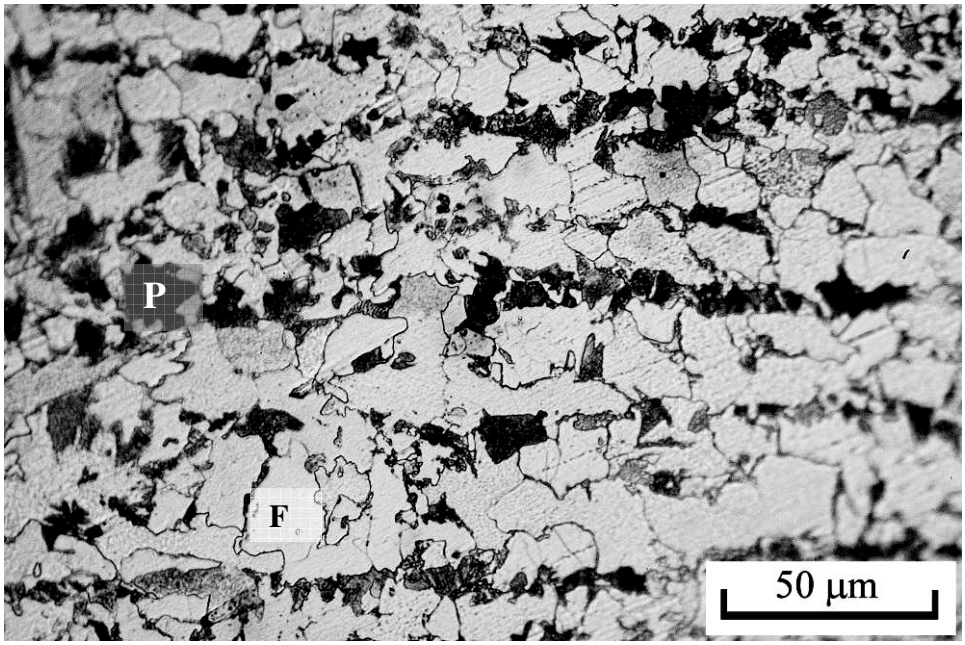

Figure 4.1. Typical SA516 Gr. 70 steel parent metal microstructure. P = pearlite, F = ferrite.

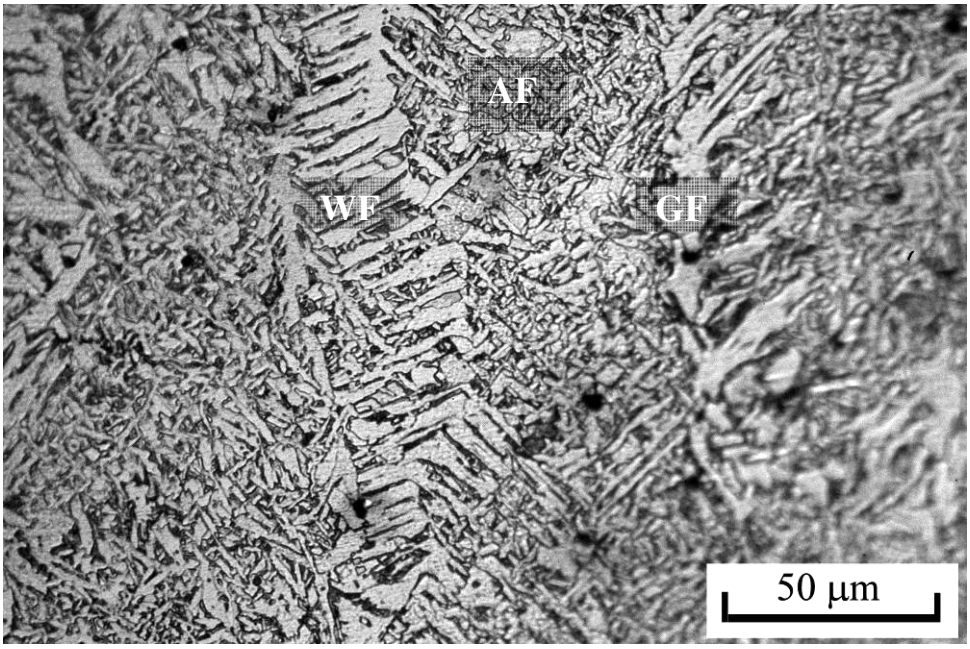

Figure 4.2. Microstructure for SA516 Gr. 70 (1st pass) weld metal at 9.3mm/s. AF = acicular ferrite, GF = grain boundary ferrite, WF = Widmanstätten ferrite.

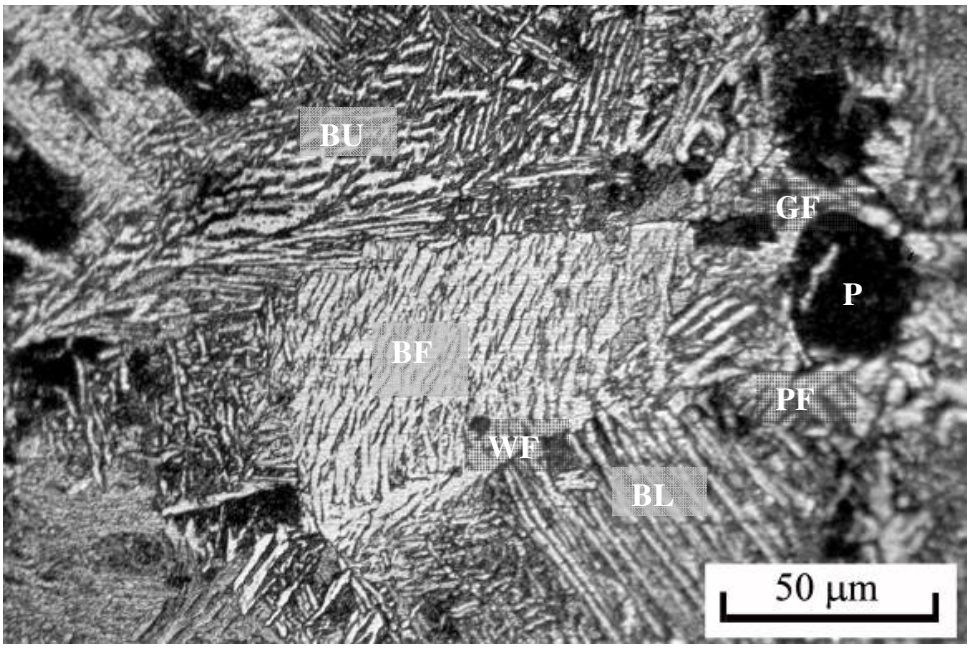

Figure 4.3. SA516 Gr. 70 microstructure for CGHAZ at 12.3mm/s. BU and BL = upper and lower bainite, BF = bainitic ferrite, GF = grain boundary ferrite, P = pearlite, PF = polygonal ferrite.

Widmanstätten ferrite (WF), pearlite (P), grain boundary ferrite (GF), polygonal ferrite (F), and maybe some martensite with retained austenite (M-A-C). These structures are similar to those found by Yang [16] in his study of SA516 Gr. 70.

The fine-grained HAZ, in Figure 4.4, not having reached temperatures above the grain-coarsening temperature and having formed at a lower cooling rate than the CGHAZ, features the same microstructure as the PM but with a finer grain structure. The grains in this area have undergone grain refinement.

Micrographs for the other welding speeds and locations are represented in Appendix B.

4.1.2 Effect of Welding Speed on Microstructure

An increase in welding speed correlates with higher cooling rates. High cooling rates (or low heat input) allow less time for grain growth and therefore increased welding speed results in finer microstructures in both the weld metal and heat-affected zone as is

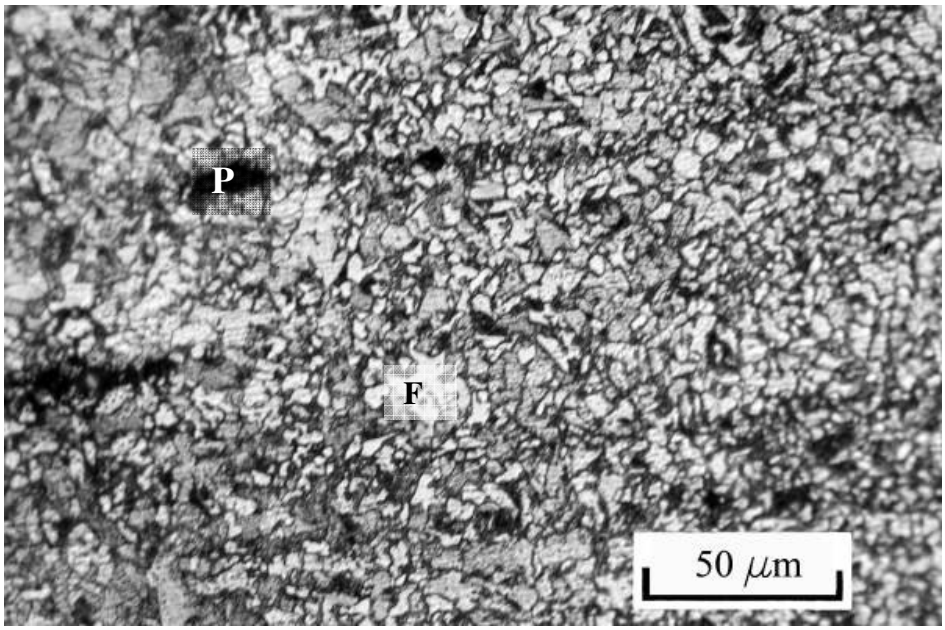

Figure 4.4. FGHAZ SA516 Gr. 70 microstructure at 12.3mm/s. P = pearlite, F = ferrite.

apparent in Figures 4.5 (a) to (c), and Figure 4.5 (d) to (f) respectively. The cooling curve in Figure 2.4 shows that high cooling rates allow for formation of less proeutectoid ferrite and more acicular ferrite, bainite, or martensite. In Figure 4.5 increased welding speed appears to reduce both the amount and texture of the grain boundary ferrite (GF) and have a corresponding increase in the AF microstructure within the WM. These results agree with those of Smith *et al*. [14].

In the HAZ, increased welding speed also resulted in finer grain structures as well as an increase in the amount of low temperature transformation products (i.e. bainite). Huang *et al*. [17] also found a finer grain structure with increased welding speed.

The reduction of the prior austenite grain size with increasing welding speed, or decreasing heat input is more evident from the HAZ /WM boundary structure shown in Figure 4.6 (a) - (c) than in either the WM or HAZ micrographs from Figure 4.5. The grains next to the fusion boundary (or the coarse-grained HAZ) become finer with increasing welding speed. This is consistent with the theory that the lower the heat input the higher the cooling rate and thus the finer the grain structure that develops.

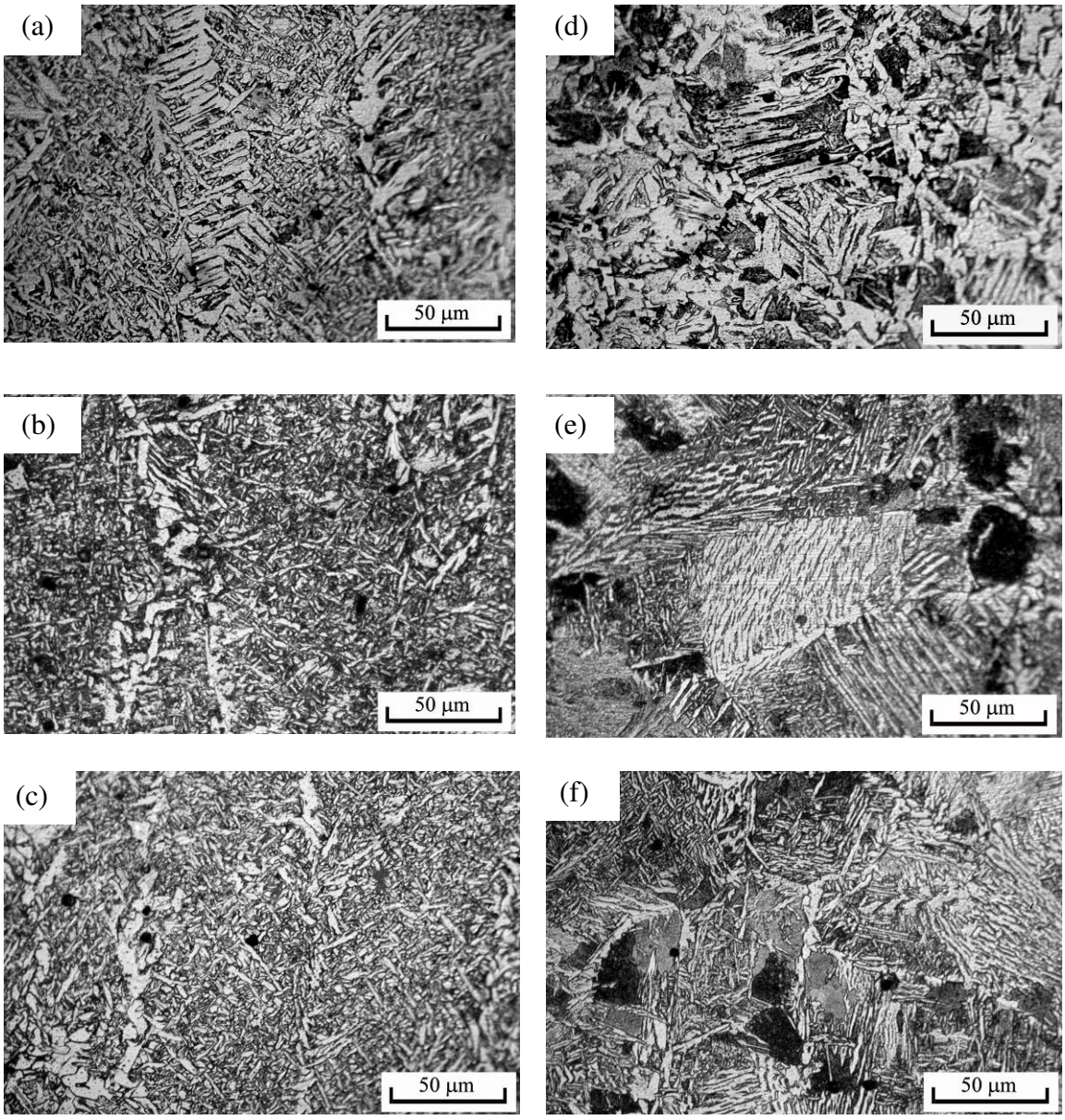

Figure 4.5. Comparison of WM grain size between the three weld speeds (a), (b), and (c), are the weld metal for 9.3, 12.3 and 15.3 mm/s welds respectively. (d), (e) and (f), are the three corresponding weld speeds for the HAZ.

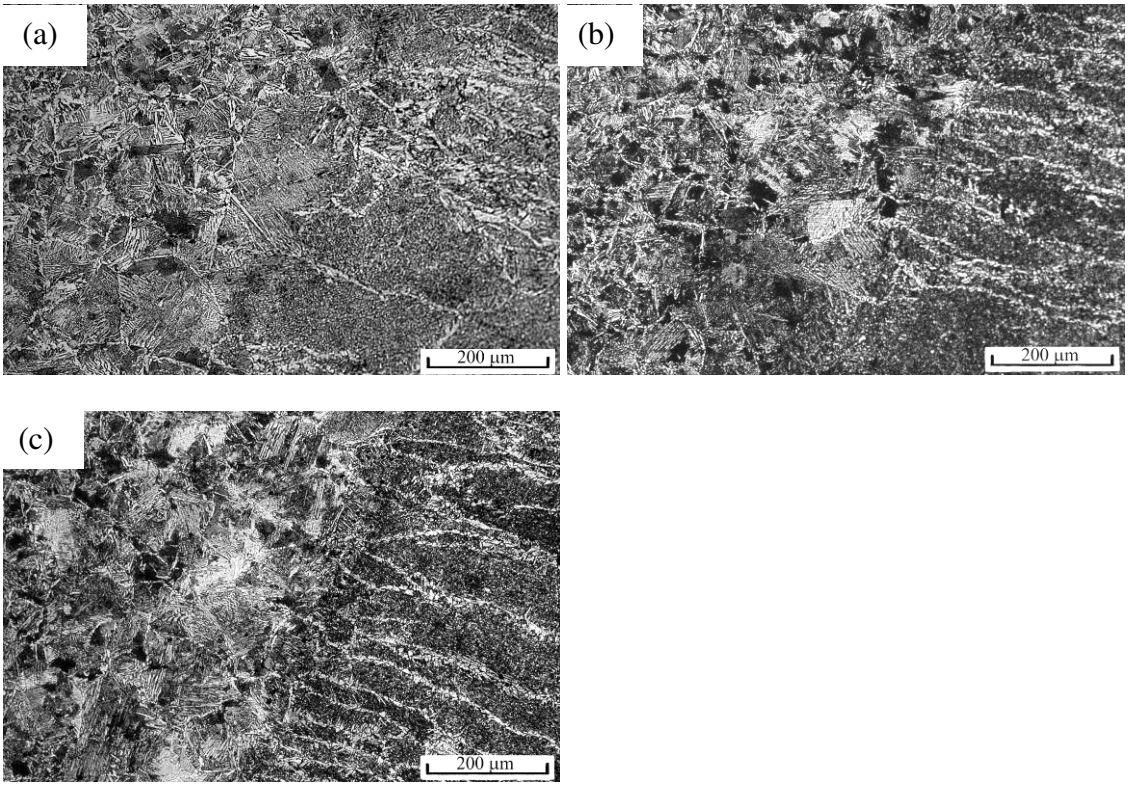

Figure 4.6. Comparison of grain size between the three weld speeds as seen from the HAZ/WM boundary. (a) 9.3 mm/s, (b) 12.3 mm/s, (c) 15.3 mm/s.

4.2 Effect of Welding Speed on the Transverse Hardness of SA516 Weldments

Microhardness measurements were taken across the three weld zones to gain an understanding of the variations in hardness between them. Hardness measurements from the parent metal (PM), the heat-affected zone (HAZ) and the weld metal (WM) are shown in Figure 4.7. Some overlap of data can be seen in the figure due to the curvature of the weld and the heat-affected zone.

It is apparent from this figure that the highest hardness values were located in the HAZ at the weld interface boundary, followed by the WM, the HAZ next to the PM boundary, and then the PM. This trend in the hardness traverse is true for each of the three welding speeds. Murti *et al*. [62], Ahmed *et al.* [45], and Yang [16] also found the highest hardness to be in the HAZ at the weld interface. Güral *et al.* [57], in their study of MIG welded AISI 1010 weldments, found contradictory results with the highest hardness values in the weld metal, then the PM, and the lowest in the HAZ. Their

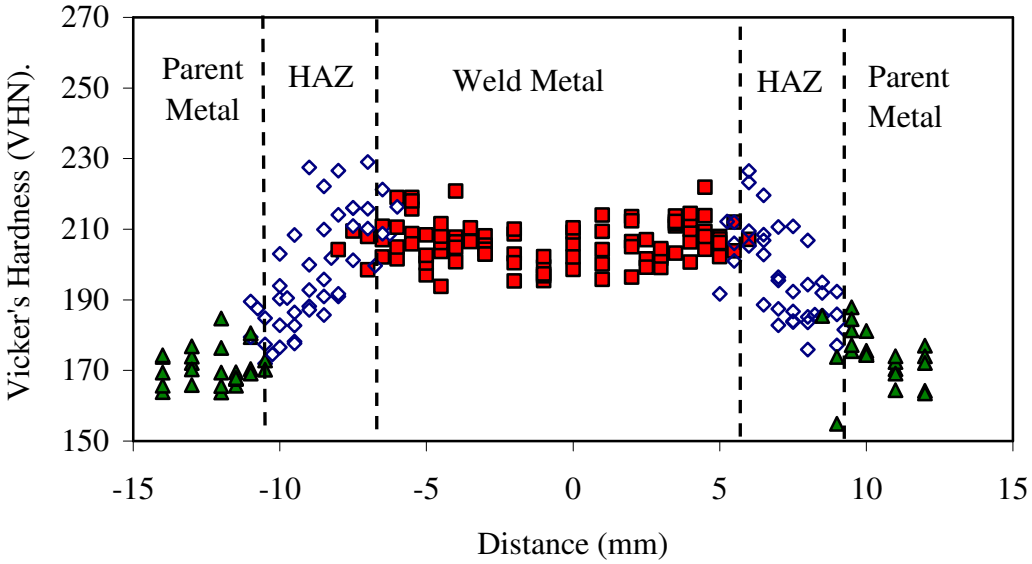

Figure 4.7. 1st Pass weld hardness plot for 9.3 mm/s welding speed.

opposing results, i.e. highest hardness in the WM, were mainly due to the difference in carbon content between their parent metal and weld metal and the difference in microstructures that developed. In the WM they saw formation of WF, AF, and some bainite whereas the HAZ mostly consisted of coarse equi-axed ferrite grains with no martensite.

Within the weld interface and the CGHAZ, the material reached temperatures above the grain coarsening temperature. This caused the austenite grains within this area to grow with growth depending upon the time spent above the grain coarsening temperature. High cooling rates cause heat to dissipate rapidly along the fusion line resulting in the formation of low temperature transformation products, such as bainite and/or martensite, to be formed within the prior austenite grains. These low temperature transformation products have high hardness. Therefore the bainite (and possibly M-A-C) in the CGHAZ explains the high values found near the weld interface.

The contrast in the hardness between the WM, PM, and the FGHAZ are also due to the difference in microstructure contained therein. The parent metal consists of soft, coarse-grained ferrite with harder bands of pearlite. The FGHAZ has the same microstructure type as the PM but has a finer grain size. Since larger grains have less resistance to

indentation than smaller grains of the same microstructure this explains the higher hardness of the FGHAZ. The combination of AF, WF, and GF in the WM has higher hardness due mostly to the large proportion of AF. Acicular ferrite with its interlocking nature gives the weld metal high strength and toughness.

4.2.1 Comparison of Hardness between the First and Second Pass Welds

There are only small differences between the average hardness values of the first and second pass welds for each welding speed, see values in Table 4.1. For example, for both the HAZ and WM of the 15.3 mm/s welding speed, comparison of Figures 4.8 and 4.9 indicates an increase in average hardness of 7 VHN from the first to the second pass welds. Figures 4.10 and 4.11 show that for 12.3 mm/s the average HAZ hardness reading between the first and second pass welds varied by only 3 VHN while there was no apparent difference in the average WM hardness. The slightly higher hardness in the HAZ in the first pass 12.3 mm/s weld may be due to its higher cooling rate compared to that of the second pass which saw increased heating of the plate from the incident preheat of the first pass. As mentioned previously, higher cooling rates increase the likelihood of forming hard structures such as lower bainite and martensite and produce a finer microstructure.

It must be noted that the average hardness values in Table 4.1 average all values in the WM or HAZ. As the HAZ consists of a combination of CGHAZ and FGHAZ the highest hardness in the CGHAZ near the weld interface does not stand out. For this reason the maximum HAZ hardness values have also been included. The WM having consistently high hardness through the zone has a higher average hardness.

4.2.2 Variation of Hardness with Welding Speed

The variation in hardness of the SA516 Gr. 70 steel with welding speed was studied by examining the data plotted in Figures 4.7, 4.8, and 4.10 and listed in Table 4.2. A change in welding speed from 9.3 to 12.3 mm/s increased the mean hardness values for both the HAZ and WM by 15 VHN. Upon further increase, from 12.3 to 15.3 mm/s, there were slight decreases of 6 and 5 VHN in the mean hardness values of the HAZ and

Table 4.1. Variation of hardness for 1st and 2nd pass welds with welding speed.

	Average Weld Zone Hardness (VHN)		
Weld (Speed)	**PM**	**HAZ**	**WM**
1st Pass Weld (15.3 mm/s)	170 ± 9	207± 21	216 ±7
2nd Pass Weld (15.3 mm/s)	170 ± 10	214± 21	223 ± 10
1st Pass Weld (12.3 mm/s)	178 ± 12	213 ± 18	221 ± 10
2nd Pass Weld (12.3 mm/s)	174 ± 8	210 ± 23	221 ± 9

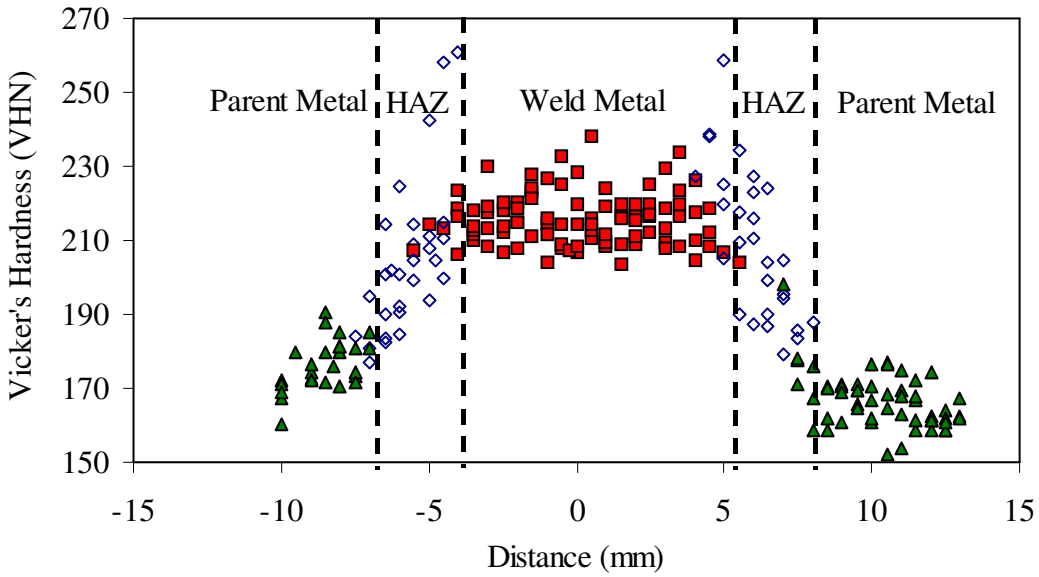

Figure 4.8. 1st Pass weld hardness plot for 15.3 mm/s welding speed.

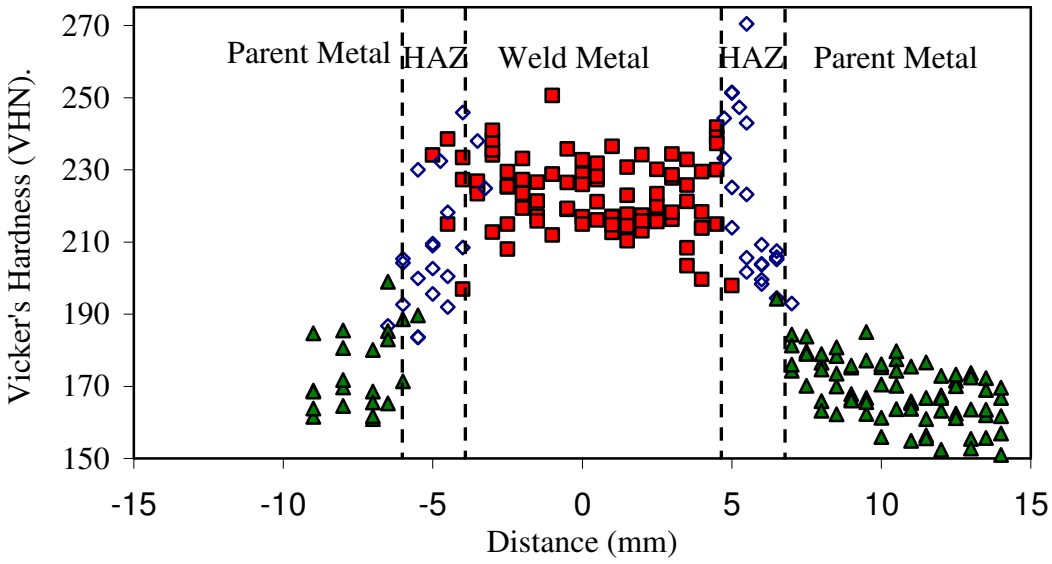

Figure 4.9. 2nd Pass weld hardness plot for 15.3 mm/s welding speed.

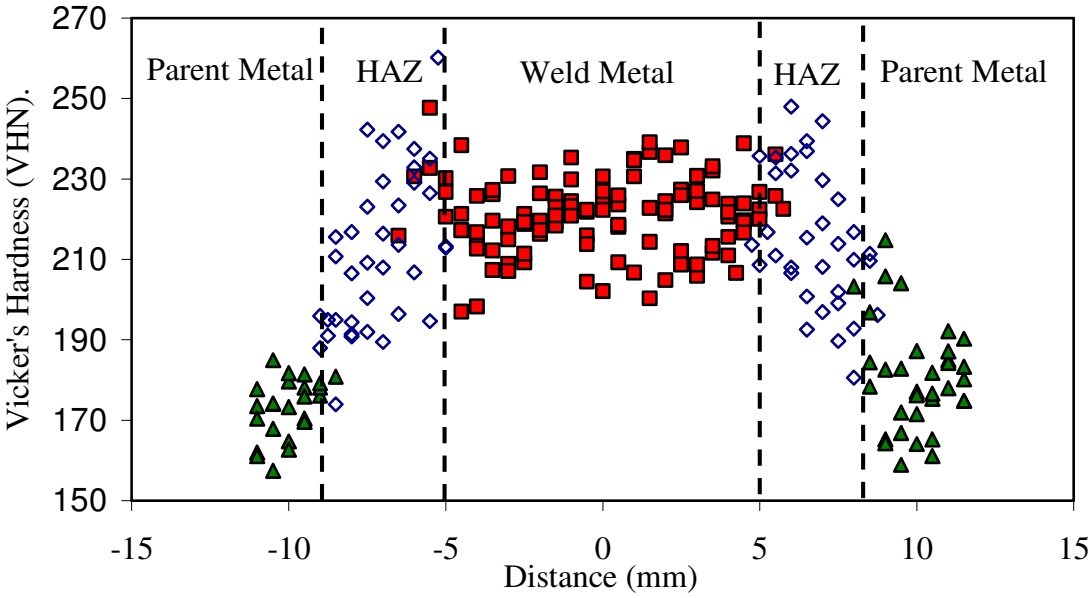

Figure 4.10. 1st Pass weld hardness plot for 12.3 mm/s welding speed.

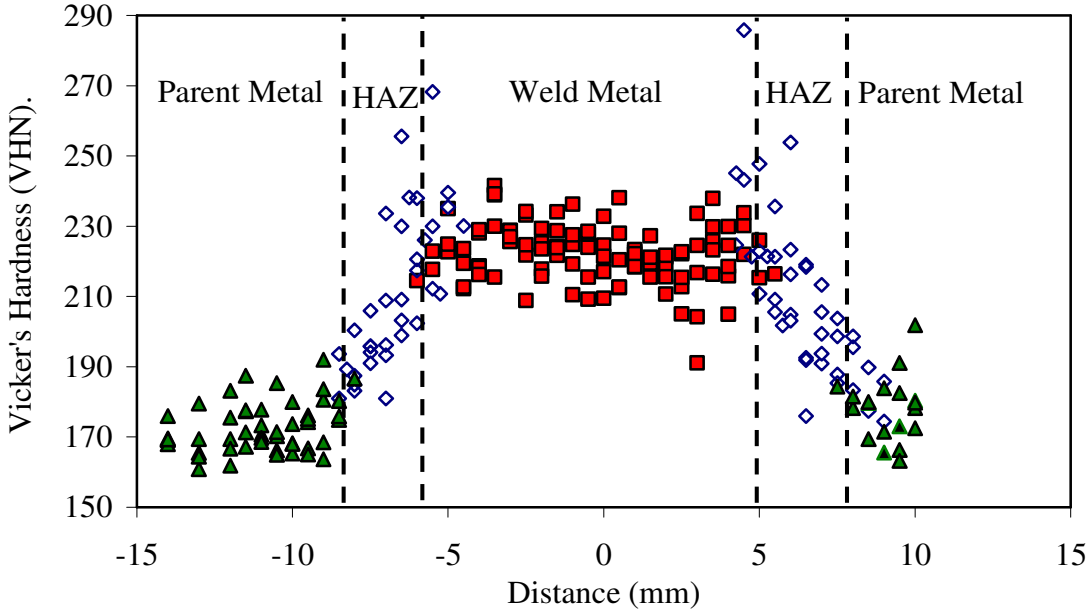

Figure 4.11. 2nd Pass weld hardness plot for 12.3 mm/s welding speed.

Table 4.2. Summary of 1st Pass hardness data for varying welding speeds.

		Average Hardness (VHN)			
Speed (mm/s)	**Heat Input (kJ/mm)**	**PM**	**HAZ**	**WM**	**Max. HAZ Hardness (VHN)**
9.3	2.6	172 ± 6	198 ± 15	206 ± 6	229
12.3	2	178 ± 12	213 ± 18	221 ± 10	260
15.3	1.6	170 ± 9	207 ± 21	216 ± 7	261

WM respectively as shown in Table 4.2. The intermediate welding speed had average hardness values slightly higher than the other two speeds in both the WM and HAZ. However, consistent with Murti *et al.* [62] the maximum HAZ hardness increased with welding speed. This leads to the conclusion that although the changes in hardness were generally small the hardness tends to increase with increased welding speed (or lower heat input) as is consistent with the results of Yang [16], Vercesi *et al.* [84] and McGrath *et al.* [3].

The increased proportion of AF in the weld metal at the expense of GF with higher welding speeds would explain the corresponding rise in hardness. AF with its interlocking nature and acicular structure has higher hardness than GF. Similarly, due to the higher cooling rates with faster welding speeds the higher proportion of bainite and or martensite forming the in HAZ explains the higher hardness.

Murti *et al*. [62] observed a similar trend of increased hardness in the HAZ and WM with increased welding speed as was shown in Table 2.1. In other words they saw a decrease in the hardness with increased heat input. The opposite, however, was found by Sundaram *et al*. [54] who observed a slight increase in the hardness of the HAZ with increased heat input or slow welding speed. The reason for the discrepancy is because at high heat inputs they encountered an increase in lath martensite-type structure and acicular ferrite and decreased polygonal ferrite than in the low heat inputs.

Bhole *et al*. [42] also found the general trend of increased hardness with faster welding speeds (or lower heat inputs). They attributed the decrease in the maximum HAZ hardness with increased heat input to the formation of high temperature transformation products such as PF, WF, and upper bainite.

4.3 Tensile Properties of SA516 Weldments

Typical stress strain curves for the three different welding speeds are shown in Figure 4.12. Figures 4.13 and 4.14 illustrate the calculated yield strength (YS), tensile strength (TS), and ductility (% elongation) for each of the three welding speeds. These values were averaged from the three specimens tested for each welding speed and for the unwelded parent metal. All but one of the specimens tested failed in the parent metal and therefore the results indicate the tensile properties of the parent metal. This suggests that the WM overmatched the tensile strength of the PM, as is the desired result, and that the HAZ has not sufficiently deteriorated such that its properties are weaker than that of the PM. As fracture is expected to occur at the weakest point this implies that the connecting material is stronger in tension than the material it connects. The remaining specimen failed in the WM. This specimen had a large lack of penetration hole in the weld, which weakened the joint and caused the failure to occur at this location. Each of the specimens broke due to ductile fracture. Typical fracture specimens showing lack of penetration defects that were present in the welds and the location of fracture are shown in Figure 4.15. Additional stress-strain data can be found in Appendix A.

Figure 4.13 clearly shows very little variation in both the 0.2% yield and tensile strengths of the three welding speeds. Yield strengths were between 319 MPa and 336 MPa, which is a 17 MPa difference. Tensile strengths varied from 539 MPa and 543 MPa a 4 MPa difference. As the specimens broke in the PM these values reflect the parent metal of the welded joint and therefore are very close to the unwelded parent metal values. The yield strength and the tensile strength are within 8 MPa and 6 MPa respectively of the unwelded parent metal values.

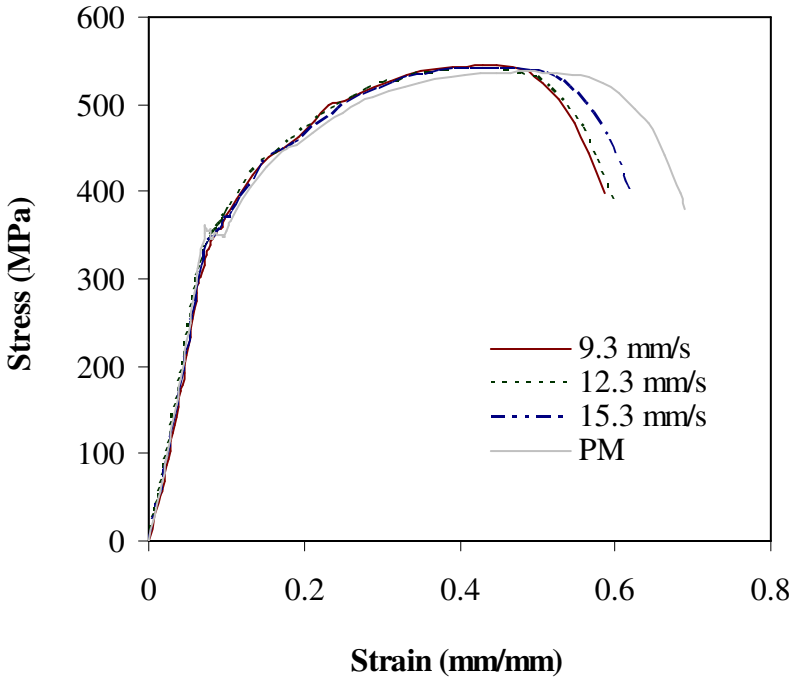

Figure 4.12. Typical stress-strain curves.

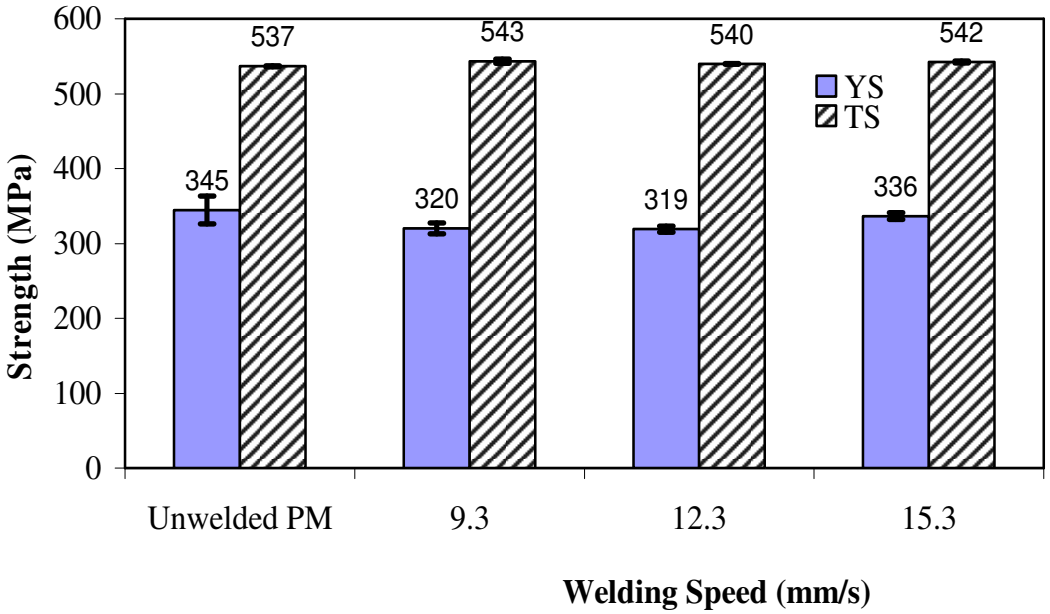

Figure 4.13. Yield and tensile strength as a function of welding speed.

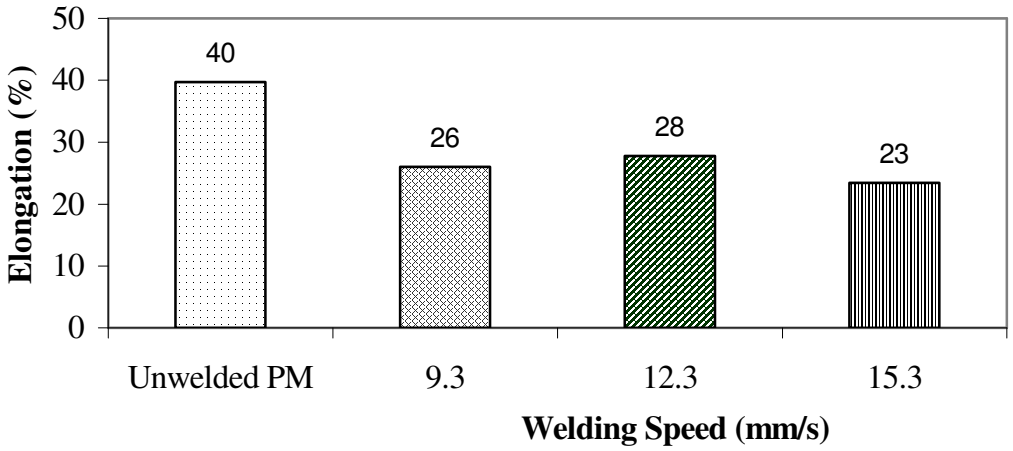

Figure 4.14. % Elongation (50.8 mm gauge length) as a function of welding speed compared to unwelded PM. *Individual data were not available.

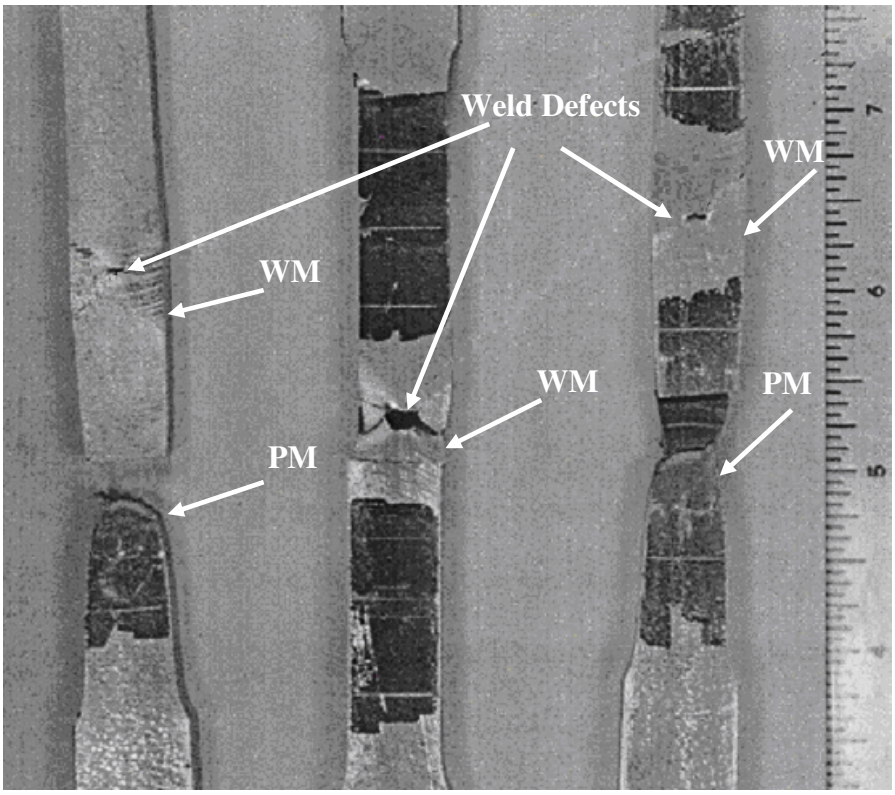

Figure 4.15. Examples of broken tensile specimens showing weld defects.

Figure 4.14, however, reveals a loss in ductility from 40% to 28% elongation between the unwelded, parent metal specimens and the 12.3 mm/s specimens. Elongation within the 50.8 mm gauge length reflects the ductility of all three weld zones as all three

participate in the plastic deformation before fracture. The hard microstructures contained within the HAZ and the WM would account for the lower ductility of the welded specimens.

Other than the specimen that broke in the WM, the lack of penetration defects in the high welding speed specimens did not have much effect on the tensile results. The gaps in the weld material weaken the bond between the two joined components. However, as the specimens broke in the PM the WM was stronger than the PM despite these defects.

4.4 Impact Toughness of SA516 Weldments

4.4.1 Charpy Impact Curves of the Weld Zones with Temperature

The absorbed energies obtained from the Charpy impact testing at temperatures ranging from -190 ˚C to 97 ˚C for PM specimens and those notched in the WM and in the HAZ are shown in Figures 4.16 – 4.18 for each of the three welding speeds studied. As expected, the energy absorbed to failure decreased with lower test temperatures. The variation of energy absorbed followed the characteristic "S" shaped curve. Large error bars shown in the curves, especially in the PM, are likely due to variations in the test temperatures that occurred when the specimens were broken. Large error bars in the 12.3 mm/s and 15.3 mm/s may also be caused by the effect of the lack of penetration and porosity weld defects present in some of the specimens. In the case of the HAZ, the scatter of results may be due to the uncertainty of the exact location of the notch tip. For this reason there was no way to ensure that the specimen would break in the CGHAZ rather than the FGHAZ.

For each temperature, the WM specimens broke at lower energy than those of the HAZ and PM. This implies the WM had lower toughness than both of the other two zones. The HAZ, normally expected to be the zone of the lowest toughness, had higher toughness than both the WM and PM. Similar trends were found between all of the three welding speeds. Therefore, opposed to literature [3, 41, 54], the WM, and not the HAZ, was the most brittle zone of this weldment. These results correlate with those found by Yang [16] for SA516 Gr. 70 for 700A, 35 V and 5.9 mm/s.

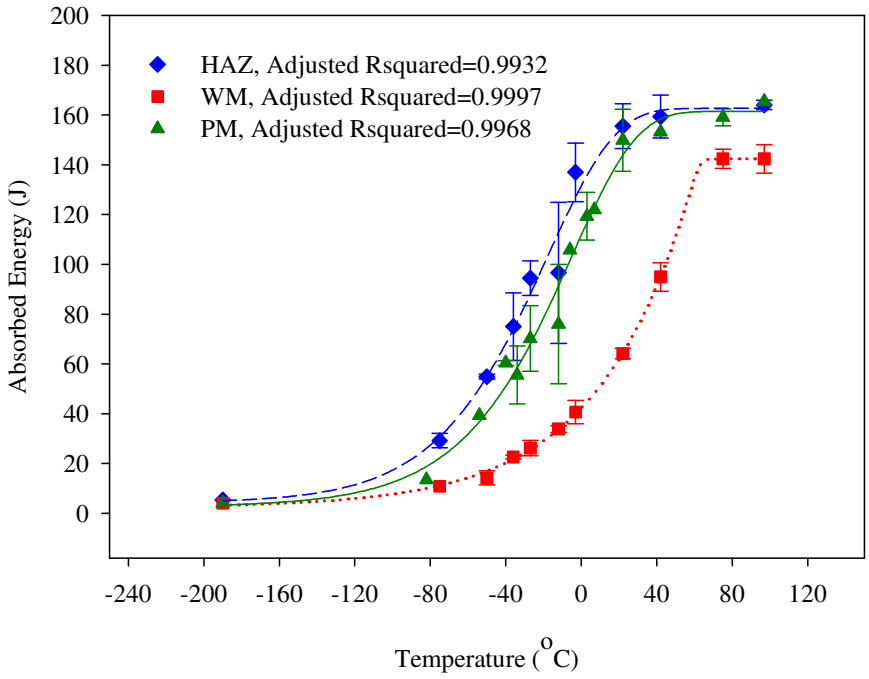

Figure 4.16. Charpy impact curves for the 9.3 mm/s welding speed.

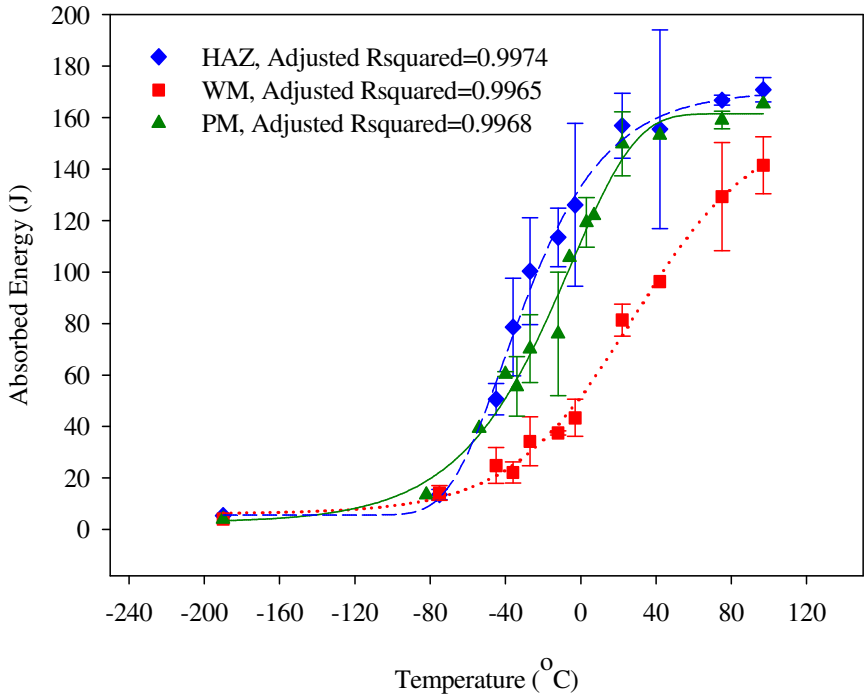

Figure 4.17. Charpy Impact Curves for 12.3 mm/s welding speed.

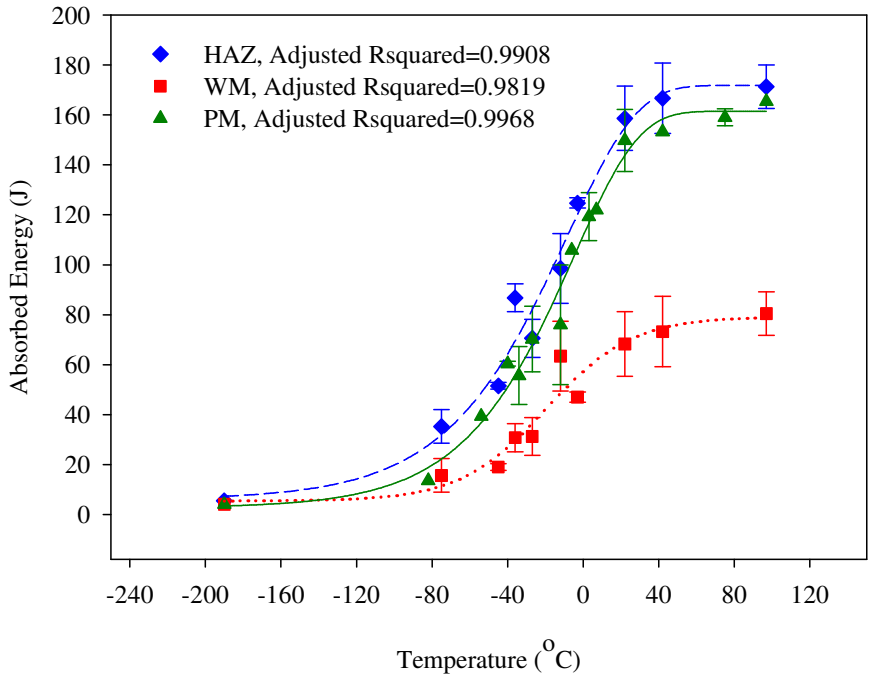

Figure 4.18. Charpy Impact Curves for 15.3 mm/s welding speed.

The high toughness of the specimens notched in the HAZ can be explained by the various microstructures contained within the notch fracture path. Due to the curvature of the HAZ and its varying size with welding speed the amount of CGHAZ, FGHAZ, and even PM that participates in the notch fracture path varies. The CGHAZ, having high strength, would be expected to have low toughness while the FGHAZ, with its softer, refined grain structure would have high toughness. The location where the V-notch is cut therefore plays an important role on the toughness data obtained [71]. The notch cutting criteria was to include as much of the HAZ as possible as it was impractical to make the effort to cut the notches in an exact location. Therefore there was no guarantee that the V-notch would include the location of highest hardness found in the hardness tests. If the notch happened to be within the softer, tougher, fine-grained HAZ the toughness reading would be expected to be higher than that of the WM. As mentioned previously, variations in the notch location would account for scatter in the toughness data for the HAZ.

The toughness of the weld zones depend largely on the microstructure that develops during welding. As discussed previously, both the WM and the HAZ contain a conglomeration of microstructures, which develop during the fusion process. The weld metal formed from a combination of the PM and the melted electrode and the resulting microstructure was a columnar structure of GF and AF. If the fracture path encounters GF the large homogenous grains give very little resistance to crack propagation. Acicular ferrite, on the other hand, with its interlocking nature causes the crack to continuously reinitiate and provides excellent resistance to crack growth and therefore excellent toughness. Therefore for good weld toughness it is desired to obtain as much AF within the WM as possible during the welding process.

In theory, the stronger (or harder) the material, the lower its toughness. However, if the increase in strength is accompanied by a smaller grain size the strength and toughness can be increased simultaneously. Generally, the WM is expected to be stronger than the PM and tougher than both the HAZ and the PM. With a high proportion of AF the WM would be expected to be both strong and tough. However, Figures 4.16 to 4.18 show that neither of these expectations transpired. The highest hardness values were found in the HAZ, as discussed in Section 4.2, which, according to theory, would normally correlate with the lowest toughness. As a general observation, for each temperature tested, more energy was absorbed by the HAZ than both the weld and the parent metal. These findings prove that it is not accurate enough to merely study the hardness or tensile data to make a conclusion about the toughness behaviour of the material.

4.4.2 Ductile-to-Brittle Transition Temperature

The Impact Transition Temperature (ITT) for the PM, WM, and the HAZ for each welding speed was determined graphically by the average energy method as demonstrated in Figure 3.4. The results of ITT for each zone with respect to welding speed are plotted as shown in Figure 4.19. In the graph, the lowest temperature indicates the best ITT in that the behaviour of the specimens in that zone, or at that welding speed changed from brittle to ductile fracture at a lower temperature.

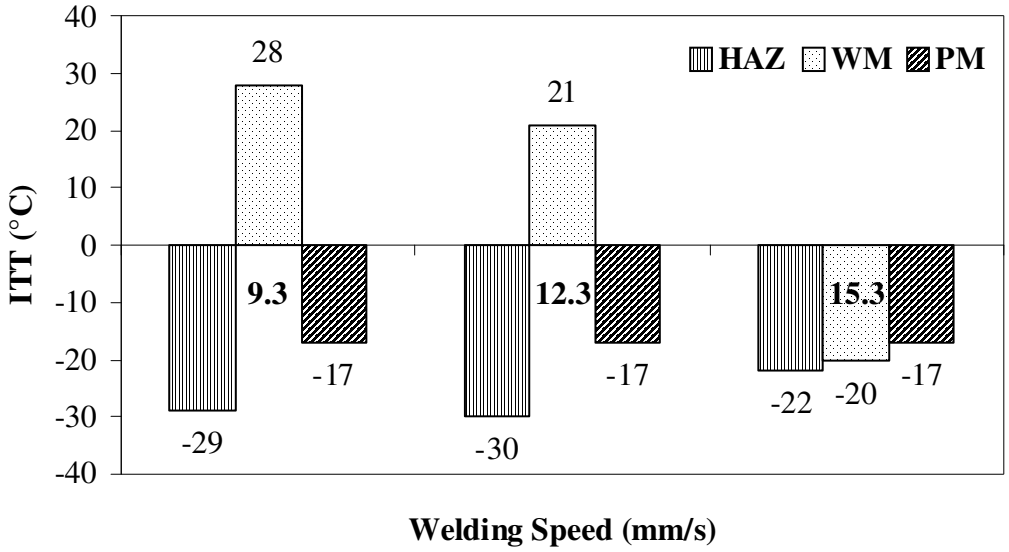

Figure 4.19. ITT as a function of welding speed.

Figure 4.19 clearly indicates that the ductile-to-brittle transition behaviour of the WM was far inferior to that of the other zones with the temperature of transition being above 20 ˚C for both the 9.3 and 12.3 mm/s welding speeds. The lower toughness of the weld metal material has been revealed through not only the inferior ITT but also in the absorbed energy values of previous graphs. This implies the deposited metal as the limiting parameter. The WM ITT values are clearly higher than those of the HAZ for all welding speeds. This graph also suggests that, according to the ITT, the fastest welding speed is superior as it provides a weld that will behave in a ductile manner for both the HAZ and the WM down to –20 ˚C unlike the other two welding speeds. At this speed the DBTT of the weld metal is also superior to the parent metal, which had a transition temperature of –17 ˚C.

Looking at the ITT as an indication of the ductile-to-brittle behaviour in each weld zone as a function of welding speed, the ITT of the HAZ marginally increases with increased welding speed while that of the WM steadily decreases. This means that the weld metal ITT was more acceptable when welded with a faster welding speed. Although the HAZ slightly reduced it still had good low temperature toughness at the faster welding speeds.

The fixed energy method was also used to determine the ductile-to-brittle temperature. This temperature was determined graphically from Figures 4.16 to 4.18 by finding the temperature corresponding to an average absorbed energy 27 J. The results are shown in Figure 4.20. The T_{27J} for the HAZ increased between 9.3 to 12.3 mm/s and then decreased from 12.3 to 15.3 mm/s. For the WM, the T_{27J} steadily dropped with speed. These results agree with that of the ITT in that the 15.3 mm/s welding speed shows the best DBTT behaviour.

4.4.3 Satisfaction of Minimum Requirements for Impact Toughness

The minimum requirement requested by Hitachi for impact toughness for pressure vessels was 27 J (20 ft-lbs) at –30 ˚C (for plates 20 to 31 mm thick) [85]. Figure 4.21 illustrates the resulting trend for impact energy at –30 ˚C with respect to welding speed for the WM and the HAZ specimens. All cases, with the exception of the weld metal at 9.3 mm/s, satisfied this requirement as seen in the figure. With an increase in welding speed, the energy absorbed at –30 ˚C of the WM specimens increased linearly while the absorbed energy of the HAZ specimen fell following a slight rise.

4.4.4 Effect of Temperature on Toughness

A drop in temperature caused the specimens to become brittle and absorb less energy. Specimens, at very low temperatures, broke without involving any plastic deformation. The resulting fracture surface of the broken specimen was smooth with its original form retained, indicating the characteristics of brittle behaviour. Figure 4.22 (a) shows this behaviour with a typical specimen broken at –190 ˚C. On the other hand, specimens broken at high temperatures absorbed considerably high energy and behaved in a ductile manner, deforming plastically before fracture. Figure 4.22 (c) shows the typical fracture surface of a specimen broken at a temperature of 97 ˚C. The fracture surface was dull and rough and portrayed the extension of shear lips on the edges, as evidence of plastic deformation. Finally, specimens broken close to the transition temperature, at –27 ˚C, shown in Figure 4.22 (b) revealed a nearly equal mixture of both ductile and brittle fracture. Additional fracture surface photographs are located in Appendix C.

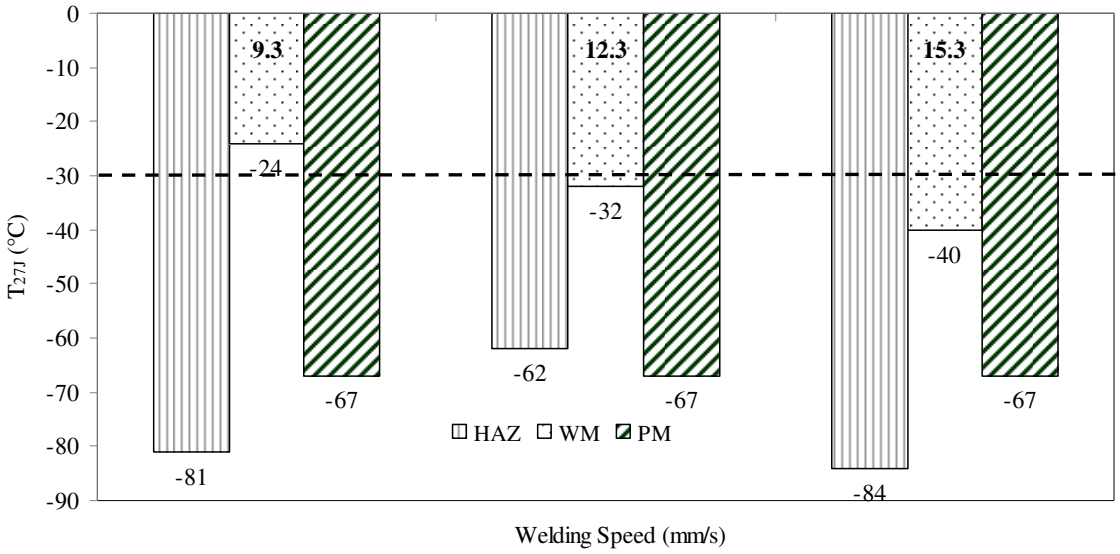

Figure 4.20. Fixed Energy T_{27J} DBTT as a function of welding speed.

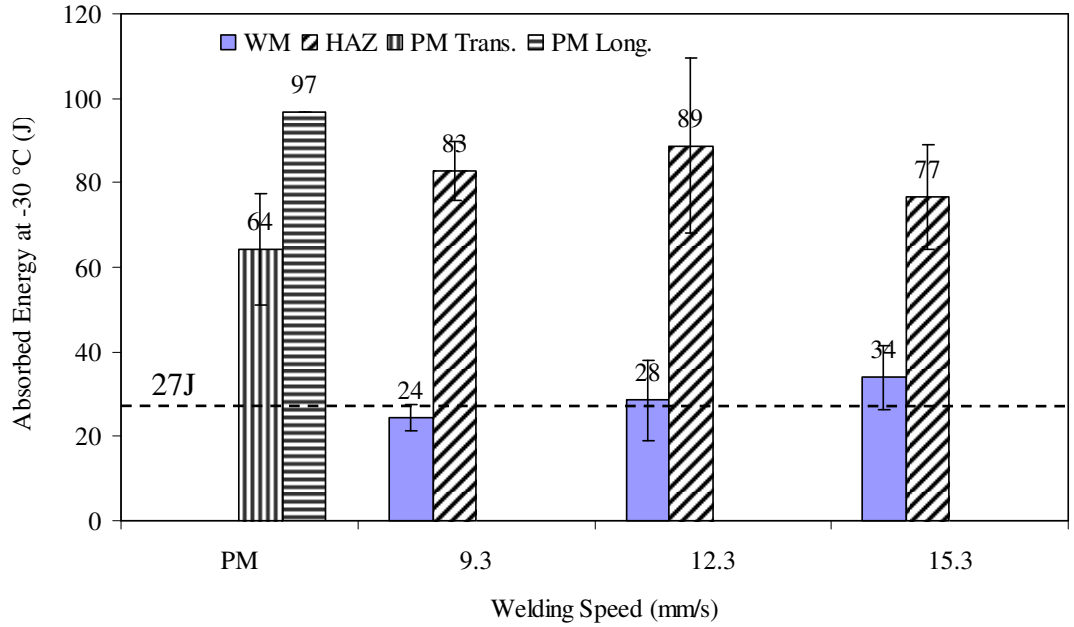

Figure 4.21. Energy absorbed at –30 ˚C with respect to welding speed. Hitachi requirements specify 27J. *Only one sample was tested for the PM cut longitudinal to the rolling direction at this temperature.

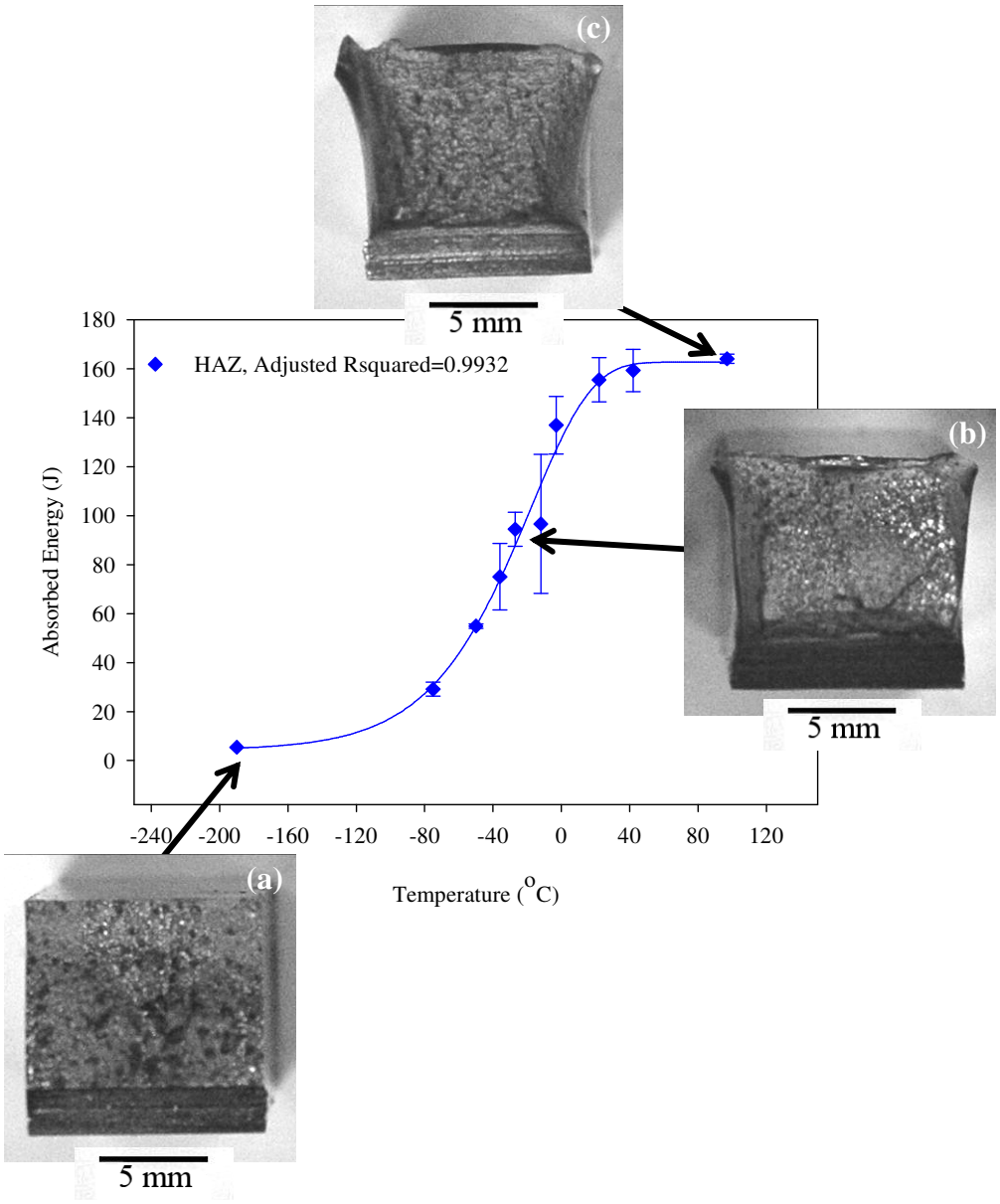

Figure 4.22. Typical Charpy impact curve of specimens notched in the HAZ and corresponding fractographs of specimens broken at (a) –190 ˚C, (b) –27 ˚C, and (c) 97 ˚C.

The scanning electron microscope (SEM) displayed a more resolved picture of each fracture surface as compared to the optical microscope, enabling more accurate characterization of the fracture mechanism. Figure 4.23 (a) – (e) are SEM micrographs correlating to the same temperature, welding speed and notch location to the fracture surfaces shown previously in Figure 4.22 (a) - (c). Similar micrographs for the other two welding speeds can be found in Appendix D.

(a)

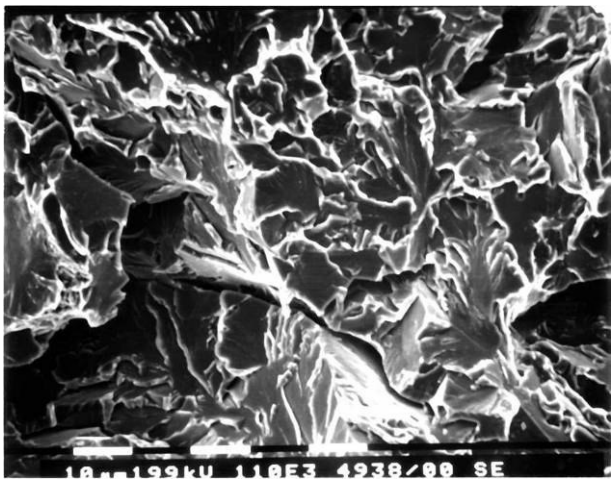

(b)

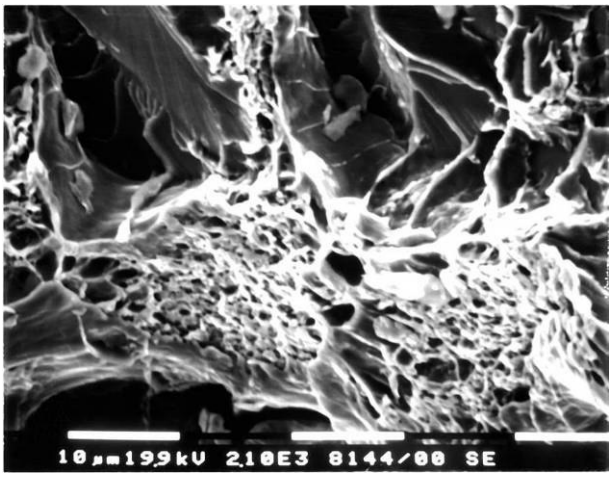

(c)

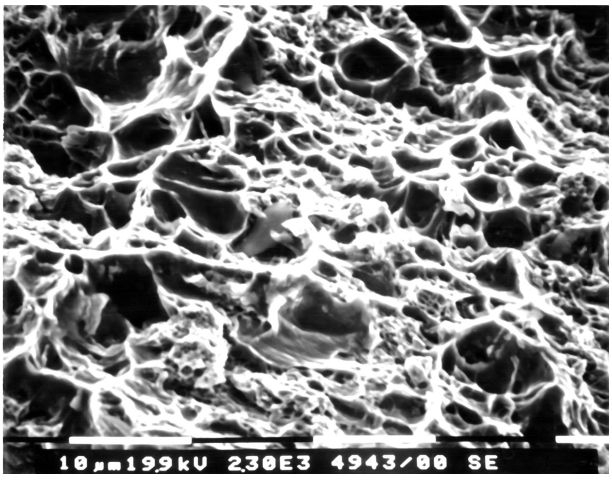

Figure 4.23. Typical SEM fractographs for 9.3 mm/s weld specimens notched in the HAZ (a) Brittle fracture at –190 ˚C showing cleavage fracture and cracks; (b) Mixed fracture at –27 ˚C; (c) Ductile fracture at 97 ˚C revealing dimples.

Figure 4.23 (a) shows brittle fracture observed for heat-affected zone specimens broken at –190 ˚C and a welding speed of 9.3 mm/s. The mechanism of this brittle fracture, called cleavage, incorporates river patterns, which are the ridges seen on the facets. Cracks can also be seen in the lower half of this picture, which were interspersed over the fracture surface.

Upon observation of Figure 4.23 (b), the combination of smooth cleavage and rough microvoid coalescence characterizes the mixed fracture, which occurred in specimens broken at the transition zone temperatures. This mechanism is sometimes called quasi-cleavage. The evidence of plastic deformation can be seen clearly in Figure 4.23 (c) with the rough dimpled surface. Microvoids, initiating at non-metallic inclusions, in the ductile material expanded and joined until they eventually ruptured upon fracture. This is the mechanism of fracture known as microvoid coalescence. Figure 4.24 shows an example of an inclusion particle in the 15.3 mm/s WM. Many of the inclusions were very small and so were not clear at the magnifications available. The SEM used did not have Energy Dispersive X-Ray Spectroscopy (EDS) capabilities to determine the chemistry of the inclusions.

The unusual tearing structure shown in Figure 4.25 was not an isolated case but was spotted on many of the fracture surfaces for each of the three welding speeds and the two notch locations. It appears as though pieces of material had been torn out of the fracture surface and are lying randomly on the surface. The mechanism that caused this structure is unknown.

4.4.5 Effect of Orientation on Toughness

Figure 4.26 illustrates the anisotropic properties of the parent metal with the differences in toughness of specimens cut from the transverse and longitudinal directions. The toughness of the parent metal was evidently higher in the longitudinal direction than in the transverse due to the rolling direction. This correlates with the results found by Robino *et al*. [40].

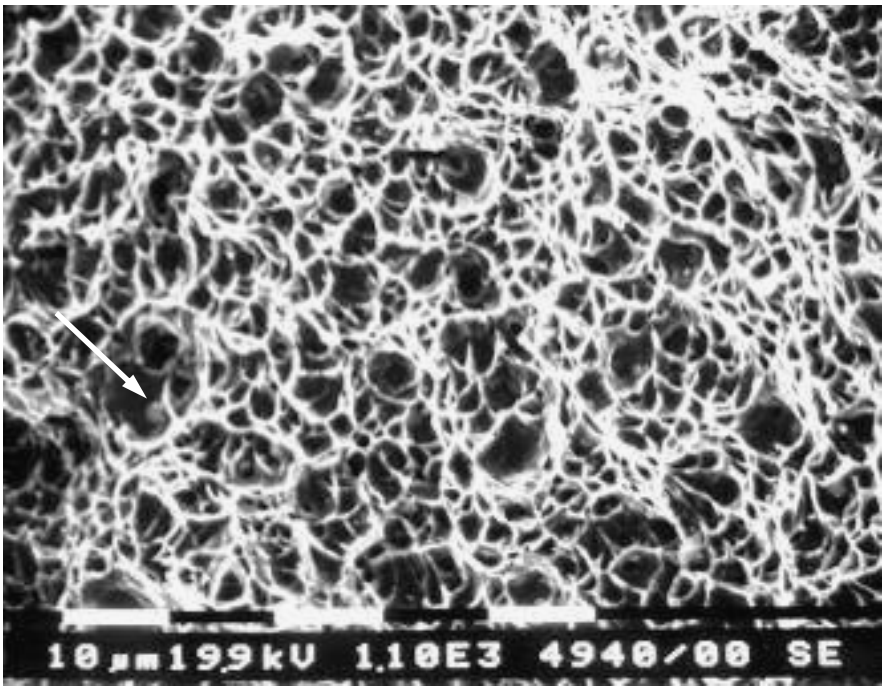

Figure 4.24. SEM micrograph showing an example of an inclusion particle in the 15.3 mm/s WM.

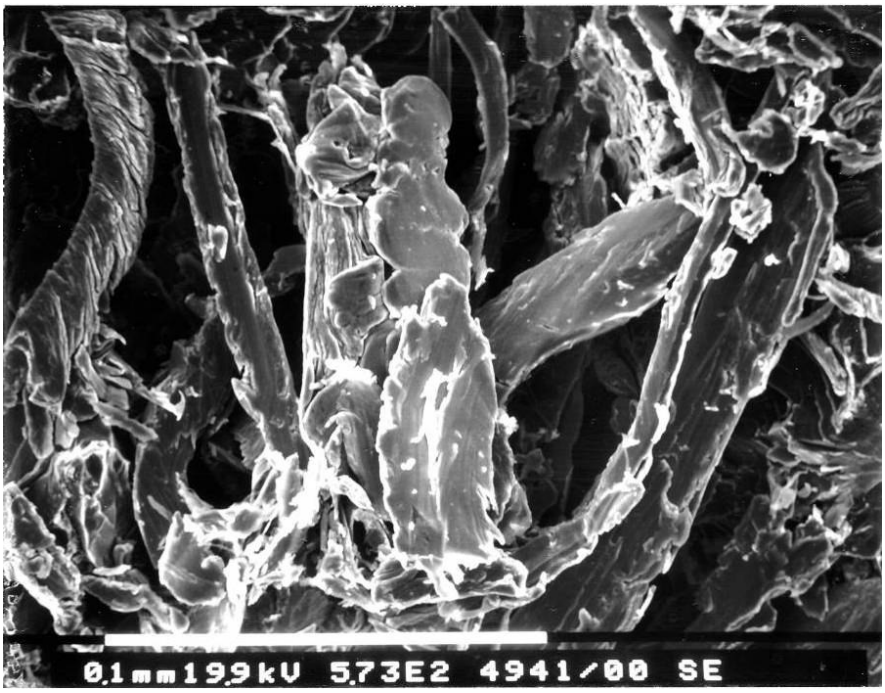

Figure 4.25. Unusual tearing seen in –190 ˚C HAZ specimen at 9.3 mm/s welding speed (not an isolated case).

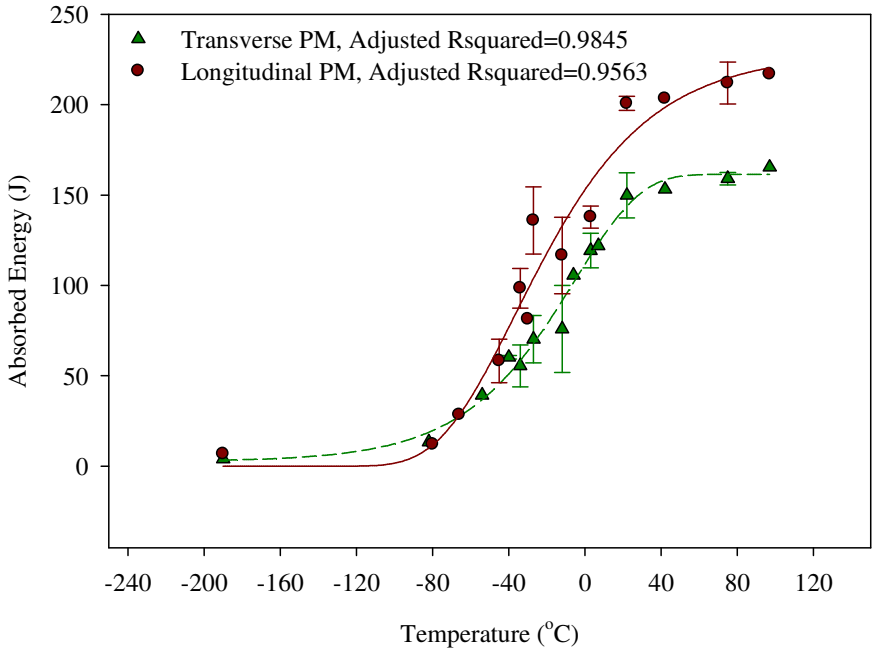

Figure 4.26. Comparison of the Charpy impact behaviour of the longitudinal and transverse orientations of parent metal.

ITT for the transverse specimens was -17 ˚C while the longitudinal specimens had a lower transition temperature of -23 ˚C. This confirms the superiority of the low temperature toughness in the longitudinal direction.

4.4.6 Effect of Welding Speed on Impact Toughness

The effect of welding speed on the toughness of the HAZ and the WM are shown in Figures 4.27 and 4.28 respectively. Table 4.3 provides a summary of the toughness data with respect to welding speed. With an increase in welding speed there was only a 9 J rise in the upper shelf energy of the Charpy impact curve between the fastest and the slowest welding speed specimens notched in the HAZ. This implies that the welding speed did not have a notable affect on the Charpy impact curve of samples from the HAZ. A rise in impact toughness, however minor, agrees with what has been found in literature of increased toughness with decreased heat input (normally correlating with faster welding speeds) [3, 14, 21, 28, 42, 45, 46, 70]. This decrease has been credited to the subsequent coarsening of the WM and HAZ microstructures (or increased grain size)

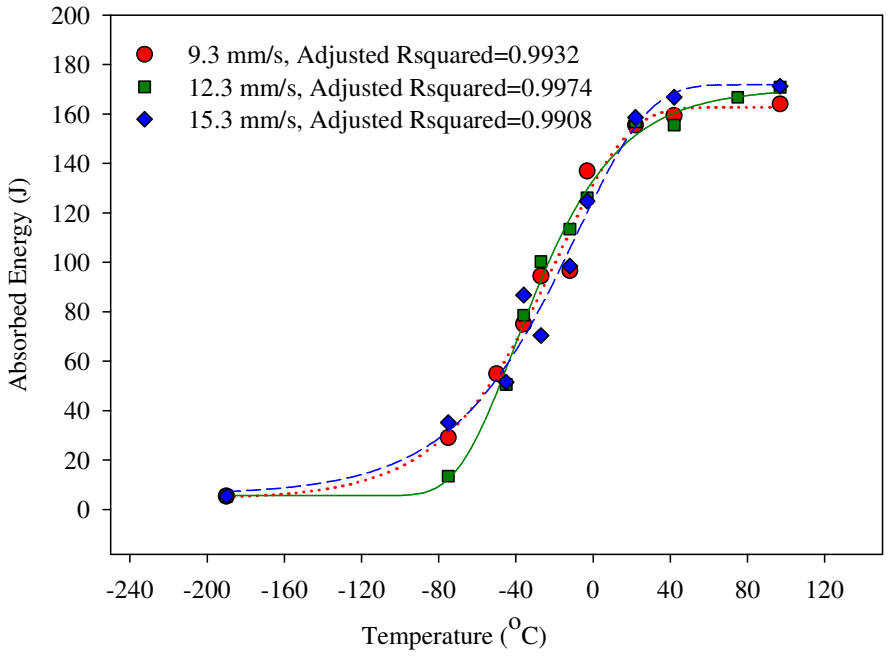

Figure 4.27. Effect of welding speed on the HAZ impact toughness.

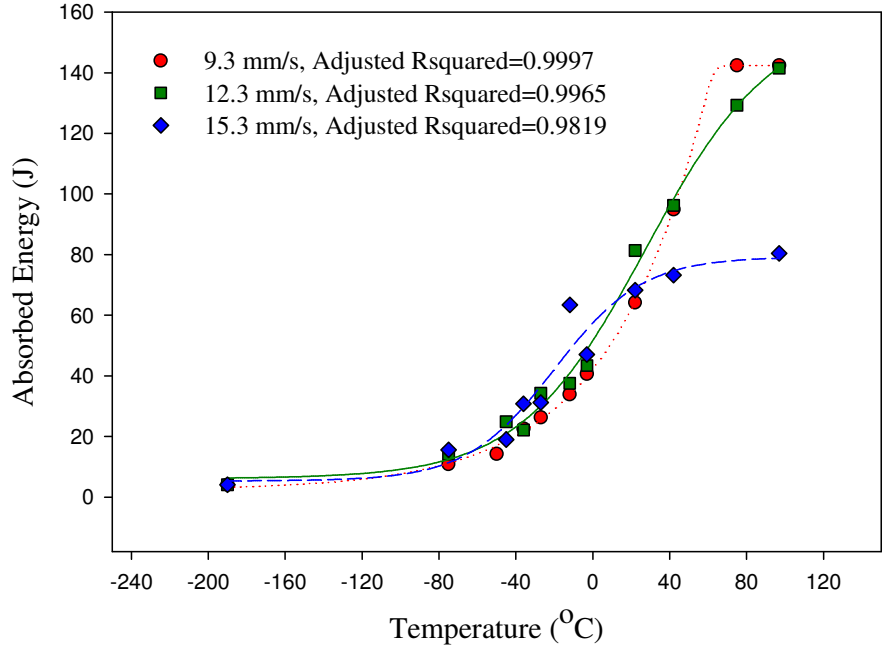

Figure 4.28. Effect of welding speed on the WM impact toughness.

Table 4.3. Summary of toughness results for SA516 Gr. 70 at varying speeds.

Welding Speed (mm/s)	Upper shelf Energy (J)		ITT (°C)			T_{27J} (°C)		
	HAZ	WM	HAZ	WM	PM	HAZ	WM	PM
9.3	163	142	-29	28	-17	-81	-24	-67
12.3	169	141	-30	21	-17	-62	-32	-67
15.3	172	79	-22	-20	-17	-84	-40	-67

with additional heat input [14, 45, 46]. For example, Murray *et al*. [12] found an apparent reduction in the impact toughness with increased heat input whereas at 6 kJ/mm the toughness values were below minimum specifications unlike the 1 kJ/mm ones that were acceptable.

Figure 4.28 shows the effect of welding speed on the WM Charpy impact toughness. The change with speed is much more visible in this zone with a 63 J drop in upper shelf energy between the intermediate and fastest welding speeds. The reason for this drop is still under speculation but is likely, at least in part, due to the lack of penetration defects observed in the 15.3 mm/s welding speed specimens. This graph suggests that the WM toughness improved with increased heat input resulting from the slower welding speed. Similarly, Sundaram *et al.* [54] found trends of higher toughness with increase energy input. However, this result is the opposite of most literature, which describe the impact toughness to decrease with increased heat input [13, 14, 16, 26, 28, 42, 46, 72]. It is possible that the defects found in many of the specimens notched in the WM of the faster welding speeds may contribute to misleading results.

Although there was a 62 J drop in the upper shelf energy of the impact curves of the WM between the 12.3 and 15.3 mm/s welding speeds, Table 4.3 and Figure 4.28 show that there was also a 41 °C improvement of the ITT. The ITT behaviour of both the 9.3 and 12.3 mm/s specimens was very poor with the transition from ductile to brittle being over 20 °C.

4.5 Lateral Expansion of SA516 Weldments

The data obtained from lateral expansion measurements for the 9.3 mm/s welding speed are shown as a percentage with respect to temperature in Figure 4.29. The plotted data nearly mirrors that of the Charpy impact curves displaying very similar trends. The Charpy and lateral expansion measurements are not exactly the same because they are accomplished by two different methods, each involving measurement errors. For example, the measurements of the lateral expansion were dependent upon the amount of pressure applied to the callipers while taking the reading.

Comparing the lateral expansion curves with respect to welding speed, in Figures 4.30 and 4.31, to those for the Charpy impact, in Figures 4.27 and 4.28, it can be seen that the graphs show similar trends. The large drop in the upper temperature lateral expansion results for the WM specimens between the 12.3 and 15. 3 mm/s welding speeds is consistent with what was seen in the Charpy impact curves. Much like the impact curves the lateral expansion curves for the HAZ did not vary significantly with welding speed; only a minor drop occurs in the high temperature expansion measurements between the 9.3 mm/s and the 15.3 mm/s but this time the 12.3 mm/s had the lowest high temperature measurement.

The transition temperatures were determined by the same method as was used for the Charpy curves but finding the temperature of the average lateral expansion as opposed to the average energy. These values are compared graphically with those of the Charpy method in the next section. Lateral expansion data for the other welding speeds and for the method not used for this thesis are included in Appendix E.

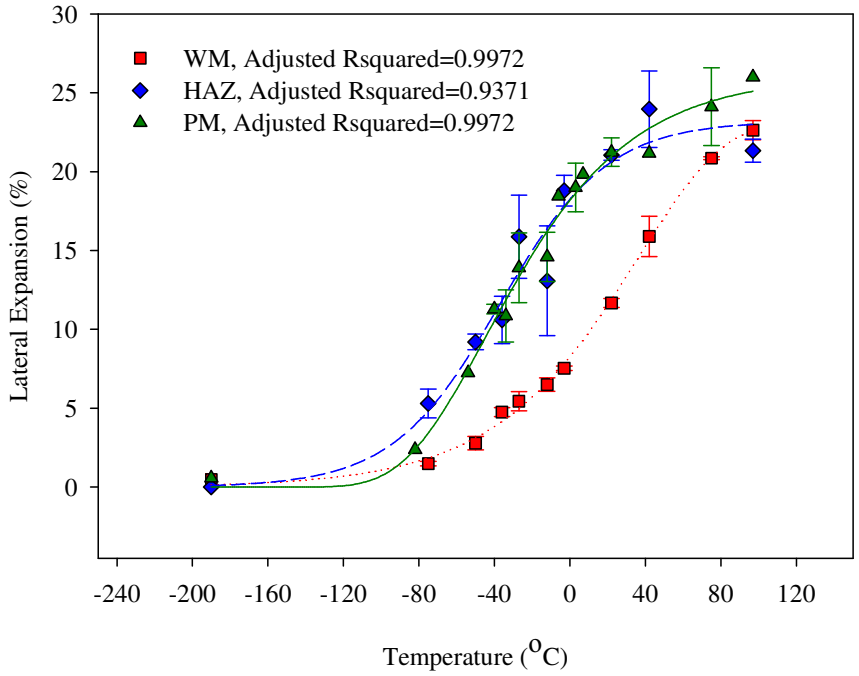

Figure 4.29. Lateral expansion for 9.3 mm/s weld speed.

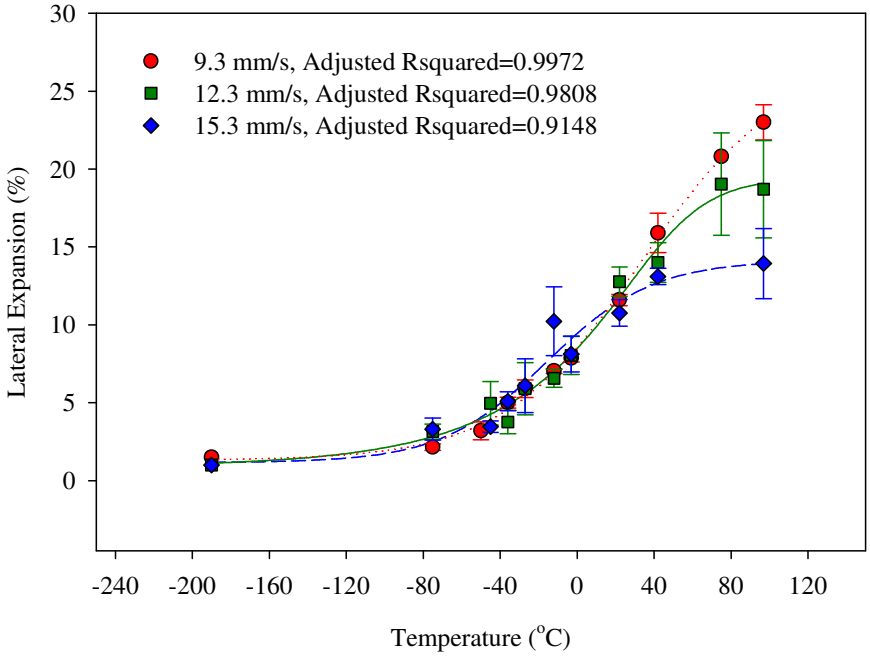

Figure 4.30. Effect of welding speed on lateral expansion of the WM.

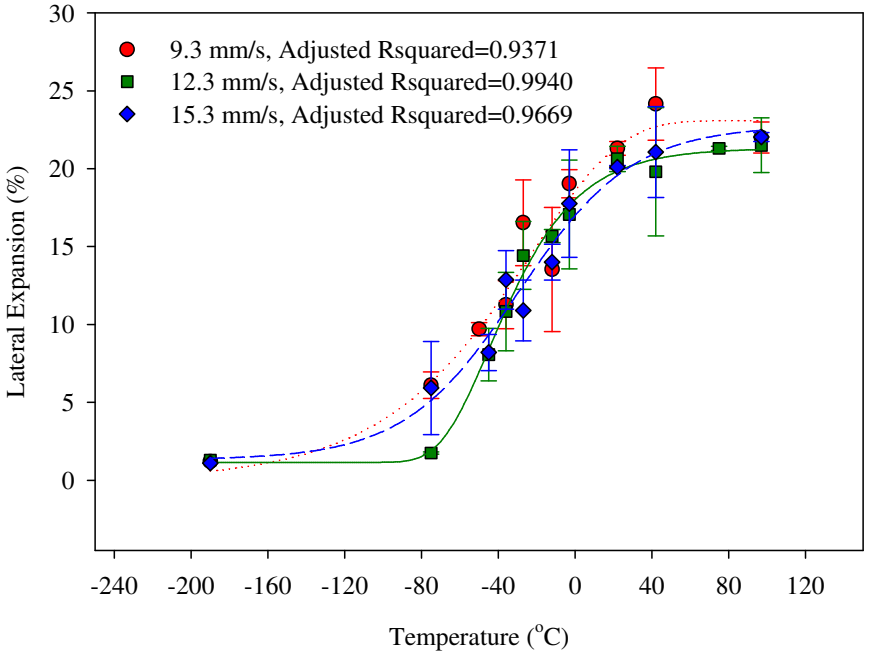

Figure 4.31. Effect of welding speed on lateral expansion of the HAZ.

4.6 Comparison of DBTTs of Charpy and Lateral Expansion Methods

The Charpy and the Lateral Expansion results are compared in Figure 4.32 for verification. The lateral expansion results exhibit a similar trend to those of the Charpy. Discrepancies in the results of the two methods may be accounted for by the fact that inconsistencies are inevitable in both methods such as the amount of pressure applied to the calipers in the lateral expansion measurements.

4.7 Defects Observed in SA516 Weldments

Lack of penetration, non-metallic inclusions, and porosity defects were found in the specimens welded at 12.3 and 15.3 mm/s. The most common defects observed were lack of penetration, which occurred particularly in the 15.3 mm/s specimens that were notched in the weld metal. Examples of a typical lack of penetration defects are shown in Figure 4.33. The breakdown of proportion of specimens containing defects and the locations of the notch are displayed in Figure 4.34. A total of 21% and 59% of the specimens welded at 12.3 mm/s and 15.3 mm/s respectively contained defects that were visible on the fracture surface. A total of 27 out of 30 of the 15.3 mm/s specimens

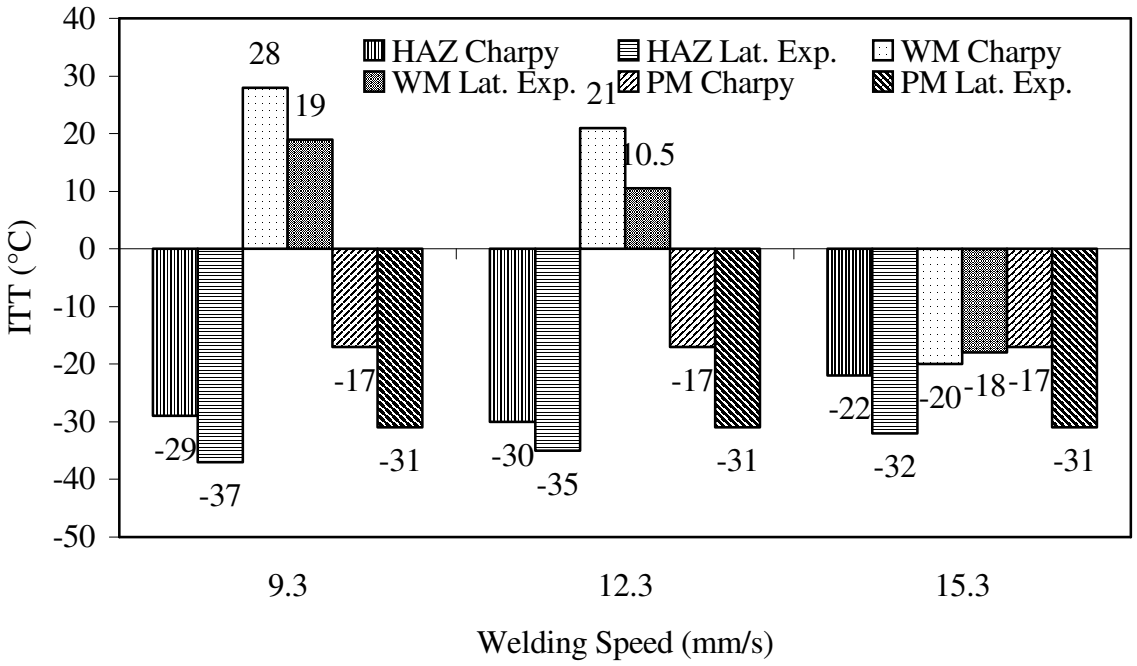

Figure 4.32. Comparison of ITT as a function of welding speed for the two methods.

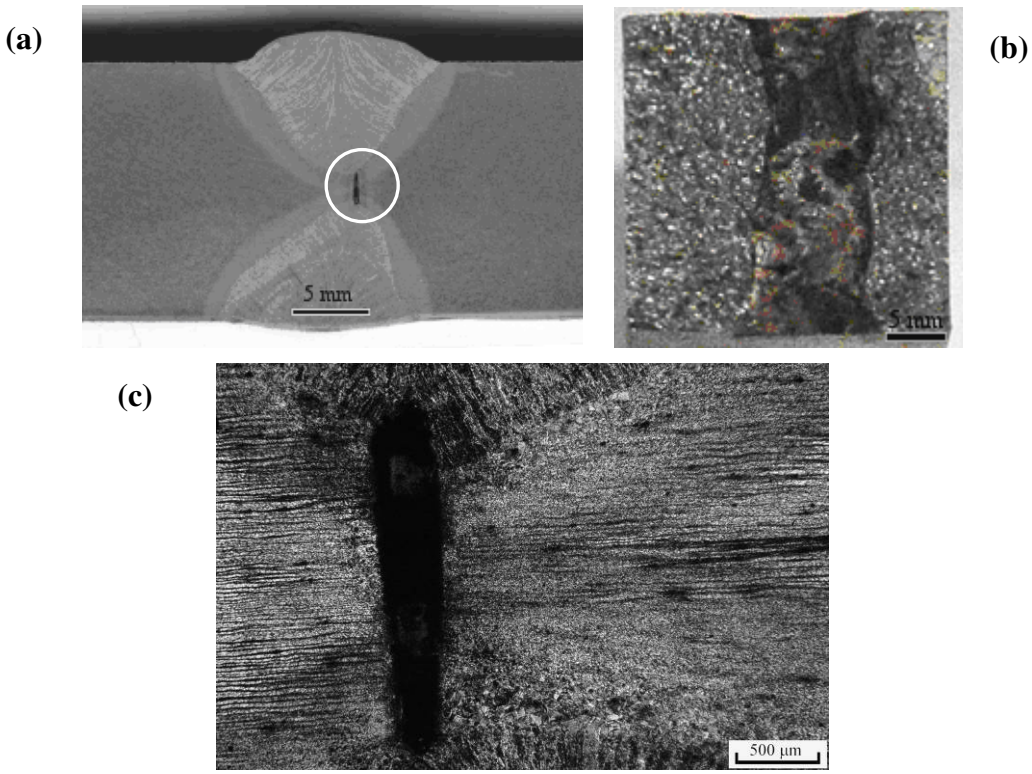

Figure 4.33. Examples of Lack of Penetration Defects from the 15.3 mm/s welding speed. (a) Macrograph, (b) fracture surface broken at –190 ˚C, (c) micrograph.

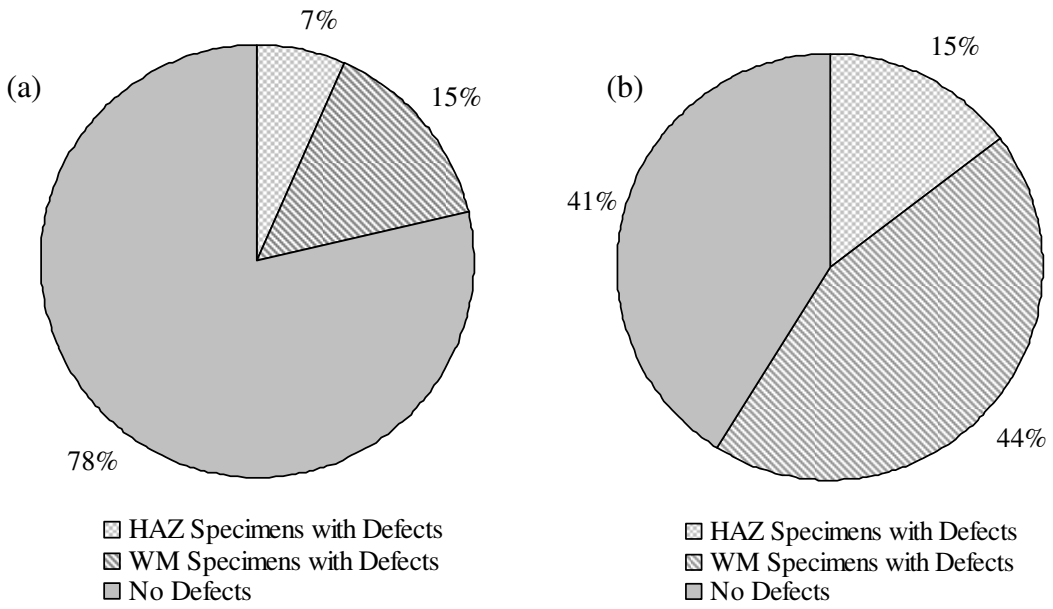

Figure 4.34. Breakdown of defective specimens in the (a) 12.3 mm/s and (b) 15.3 mm/s welding speeds specimens.

notched in the weld metal contained defects (44% of all 15.3 mm/s specimens) as well as 9 out of 31 of the specimens notched in the HAZ (15% of all 15.3 mm/s specimens). Of the specimens welded at 12.3 mm/s, 21% contained defects including 4 out of 31 of the specimens notched in the HAZ (7% of all 12.3 mm/s specimens) and 9 out of 61 of the specimens notched in the WM (15% of all 12.3 mm/s specimens).

Despite the defects found in the 15.3 mm/s specimens, they still showed good toughness values as compared to the slower welding speeds. In this case, the direction of the hole made it similar to two thin specimens tested beside each other with each absorbing a portion of the energy. Had the defect been in the other direction, perpendicular to breaking direction, a more obvious effect would have been seen in the energy values.

The slowest speed having enough time to obtain full penetration did not have lack of penetration defects. Slower welding speeds allow more time for the fusion process and increase the filler metal deposition rate to fill the gap. In contrast, faster welding speeds lower the deposition rate allowing less filler metal melting and increase the chance of lack of penetration defects.

As a large percentage of the specimens (i.e. 27 out of 30 (or 90%) of the weld metal notched specimens welded at 15.3 mm/s) had defects it was impossible to disregard these. The lack of penetration defects did not have an obvious affect on the results obtained during testing of the faster welding speeds.

4.8 Effect of Welding Speed on the Weld Geometry of SA516 Weldments

The penetration, bead width, HAZ size, and reinforcement were studied with respect to the welding speed at the fixed amperage and voltage of 700 A and 35 V, respectively. The first pass weld of each plate (or top weld) was welded from room temperature. However, the second pass weld (bottom weld) was welded with a much higher interpass temperature as the plate was flipped and welded without allowing it to return to 20 ºC. The variations in the initial temperatures account for differences in the geometry of the 1^{st} and 2^{nd} pass weld deposits.

Scans of the three welds after being ground, polished and etched and the HAZ traced are shown in Figure 4.35 with the first pass welds on the top. These pictures were used to measure the weld bead geometry. It must be noted that due to machining limitations the weld geometry measurements in this section are taken from one representative sample not averaged across the whole plate.

In both the 12.3 and 15.3 mm/s welds a lack of penetration is evident, as a gap existed between the deposited metal of the two passes. However, the 9.3 mm/s weld had good penetration and was superior from that viewpoint. The reduction in the size of the HAZ is unmistakable with higher welding speed as is predicted in the literature [16, 58, 45, 67, 74, 75].

The penetration (P), bead width (B), reinforcement (R) and heat-affected zone size (w) were all measured for each of the three welding speeds. The resulting measurements from the 1^{st} and 2^{nd} pass welds are listed in the corresponding graphs. It must be noted that this data assumes that the measurements are uniform along the length of the plate.

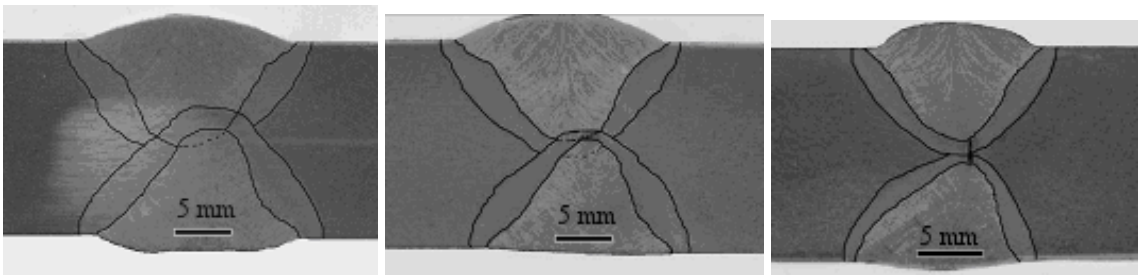

a) 9.3 mm/s b) 12.3 mm/s c) 15.3 mm/s

Figure 4.35. Scans of the three welds with the HAZs traced.

Consistent with other studies [16, 68, 76, 77, 78], the penetration and bead width decreased with increased welding speed as demonstrated in Figures 4.36 and 4.37 respectively. Faster welding speeds result in less filler metal melting and therefore a lower metal deposition rate per unit length of weld. A notable difference was found between the geometry measurements of the first and second pass welds, which can be accounted for by the difference in the temperature of the plates when they were welded. The first pass weld was welded from room temperature, while the second pass weld was still hot. Heating the plate before welding aids in electrode deposition and increases spreading, aiding in penetration and widening the weld bead. Because of this, instead of the constant (nearly linear) decline in the penetration depth with speed as in the first pass weld, the penetration of the second pass weld appears to decrease at a much slower rate. Thus, it would seem that preheating the plates before welding would lessen the chance of the incomplete penetration found at the high weld speeds.

Figure 4.38 reveals a noticeable effect of welding speed on the size of the heat-affected zone. With an increase in speed, the size of the heat-affected zone reduced appreciably due to less time for heat to radiate through the joint to the surrounding material. The faster welding speed therefore resulted in a narrower region of the parent metal that was heat-affected than that of the slower speed.

The effect of changes in welding speed on the weld reinforcement is shown in Figure 4.39. With less time allowed for electrode melting per length of weld, the height of weld reinforcement is generally shorter the faster the welding speed. The interpass temperature of the second pass weld caused the weld bead to spread out resulting in

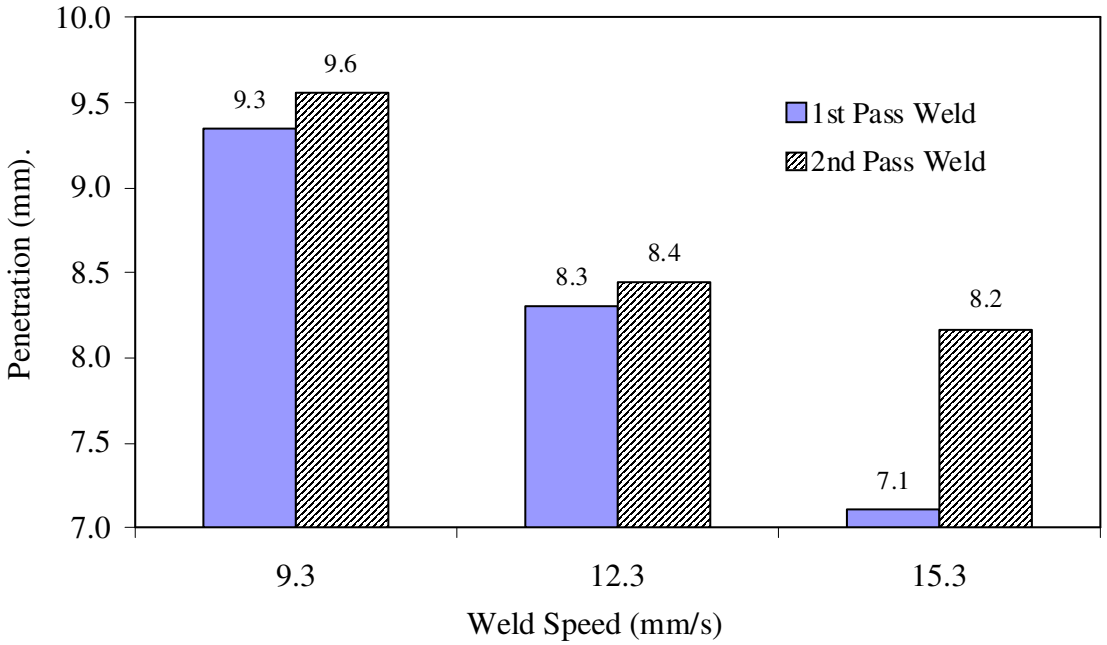

Figure 4.36. Effect of weld speed on joint penetration.

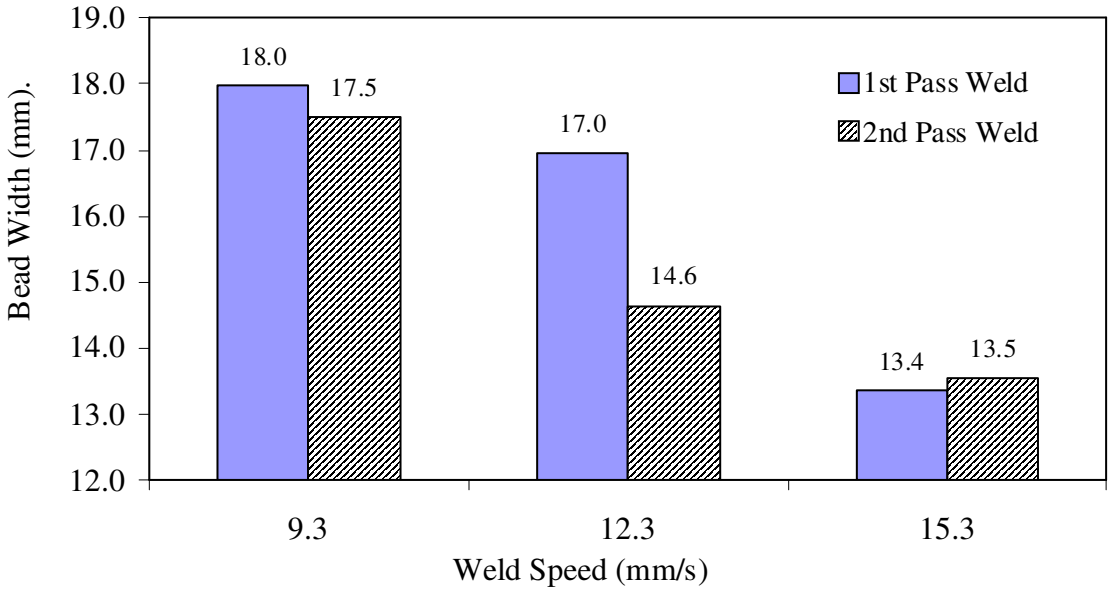

Figure 4.37. Effect of weld speed on bead width.

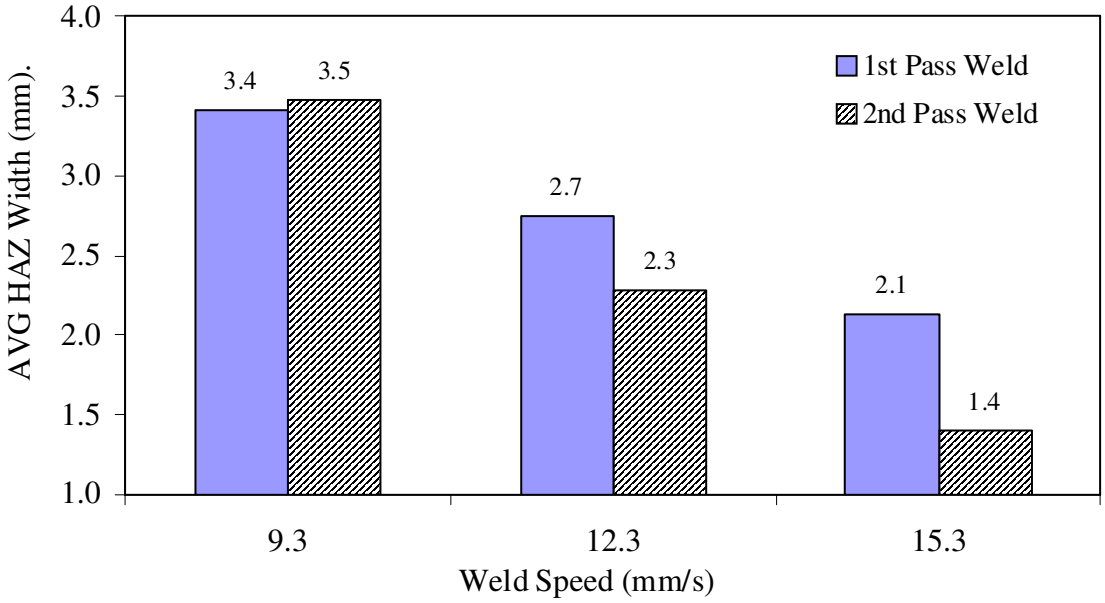

Figure 4.38. Effect of weld speed on HAZ size.

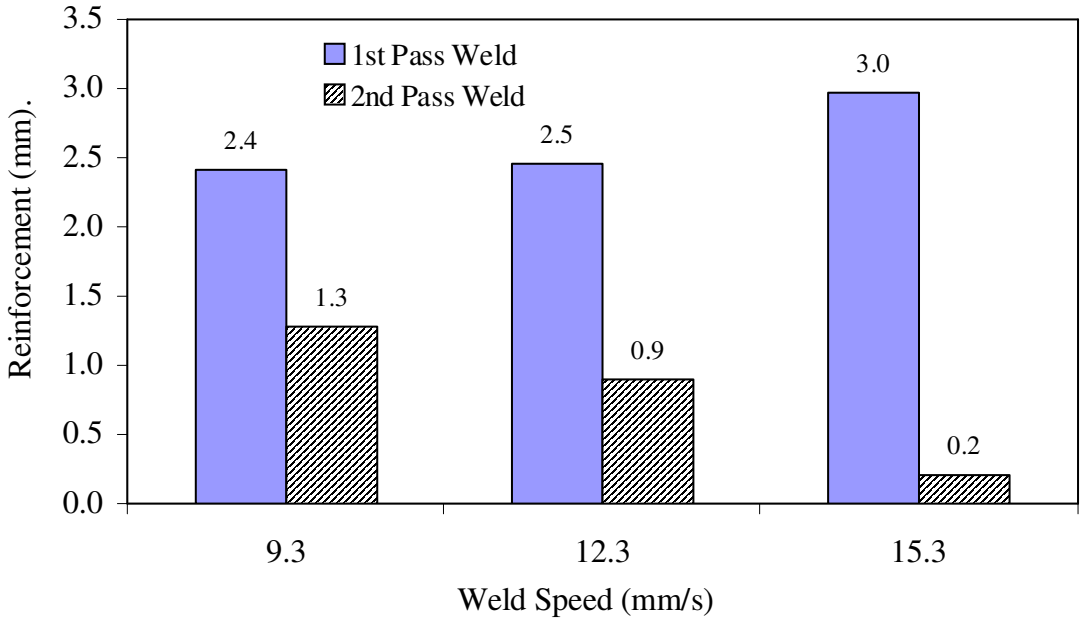

Figure 4.39. Effect of weld speed on reinforcement height.

shallower weld reinforcement. Decreased reinforcement with increased speed agrees with the literature [16, 68, 75, 76, 77].

5 CONCLUSIONS AND RECOMMENDATIONS

5.1 Conclusions

In this study 17 mm thick sheets of SA516 Grade 70 steel were welded at heat inputs of 1.6, 2.0 and 2.6 kJ/mm correlating with welding speeds of 15.3, 12.3 and 9.3 mm/s. The effect of welding speed on the weld quality and mechanical properties were assessed through hardness measurements, Charpy V-notch testing, lateral expansion measurements, and tensile testing. Fractography was performed using optical and scanning electron microscopy in order to correlate the mechanism of fracture with the impact toughness values. Based on the results obtained from the tests, measurements, and observations the following conclusions can be drawn.

1. For each welding speed the highest hardness values were found in the coarse-grained heat-affected zone immediately adjacent to the weld metal while the lowest hardness was found in the parent metal. The intermediate welding speed (12.3 mm/s) had the highest average hardness in each of the three weld zones. The maximum hardness rose by 32 VHN with an increase in welding speed from 9.3 to 15.3 mm/s.

2. For all welding speeds the heat-affected zone had higher impact toughness than both the weld metal and parent metal. The weld metal consistently had lower toughness than either of the other two zones making it the limiting factor of the welded joint. The HAZ not only had the highest toughness but also the best ductile-to-brittle transition behaviour. Welding speed appeared to have little affect on the notch toughness of the heat-affected zone with only a 9 J rise in the upper shelf energy and an 7 °C rise in the impact transition temperature (ITT) between the slowest and fastest welding speeds. Welding speed had more influence on the WM with a 63 J drop in the upper shelf energy but also a 48 °C improvement of the ITT between the 9.3 and 15.3 mm/s welding speeds. All

cases but the 9.3 mm/s specimen notched in the WM satisfied Hitachi's requirement for 27 J at -30 °C.

3. All tensile specimens but one broke in the parent metal (PM). The specimen that did not break in the PM had a large lack of penetration defect in the weld metal, which weakened the joint causing it to break in that location. Fracture occurring in the PM implies that the WM and the HAZ had better tensile properties than that of the PM. Since the specimens broke in the PM the yield and tensile strength values indicate that of the PM and are therefore within the same range as the unwelded parent metal.

4. Increased welding speed appeared to reduce the grain size and amount of grain boundary ferrite in the weld metal microstructure while increasing the proportion of acicular ferrite. The increased speed also appeared to reduce the prior austenite grains and increase the amount of low temperature transformation products with high hardness such as bainite. Finer grain structures in the HAZ and WM produced with the faster welding speeds can be attributed to less time for grain growth.

5. The slowest speed (9.3 mm/s) obtained full penetration and therefore did not have lack of penetration defects found in both of the faster welding speeds. A total of 59% of the 15.3 mm/s specimens and 22% of the 12.3 mm/s specimens had incomplete penetration and/or porosity defects. Theoretically, lack of penetration defects in a weld would weaken the joint; however the results show that the defective specimens generally still had adequate toughness. For example, the 15.3 mm/s notched in the weld metal, having defects in 90% of the specimens tested, still had an impact transition temperature of -20 °C or a T_{27J} of -40 °C.

6. The fastest weld speed (15.3 mm/s) produced incomplete penetration defects but had the narrowest heat-affected zone and exhibited better impact transition temperatures than the other two welding speeds for both the weld metal and heat-affected zone specimens.

7. Increased welding speed generally resulted in a reduction in penetration, bead width, HAZ width, and reinforcement.

5.2 Recommendations

1. Energy Dispersive X-Ray Spectroscopy (EDS) should be used to identify the composition of the inclusions found in fracture surface dimples. This information would be useful for studying the fracture properties. Measuring the size of these inclusions would also be informative.

2. It would be useful to assess the strength and elongation properties of the weld metal (WM) zone individually. In order to do this, tensile specimens should be cut from the WM along the welding direction. In this way the strength properties of the weld could be compared to that of the parent metal.

3. The effect of welding parameters on the heat-affected zone could also be studied separately to get a clearer picture of the properties in this zone. Due to the small size of the HAZ this would likely require HAZ simulation similar to that performed by the variety of researchers cited in this thesis [3, 17, 21, 43, 49, 51-53, 55].

4. In order to more accurately compare the effect of welding speed on the microstructures the grain sizes within the WM and HAZ as well as the proportions of AF and other structures should be measured. This data would allow a more accurate assessment of the changes in mechanical properties of the different zones with respect to the welding parameters.

REFERENCES

1. R.D. Thomas Jr., 1977, "Submerged-Arc Welding of HSLA Steels", *Metal Progress,* Vol. 111, No. 4, pp 30-36.

2. B. Basu and R. Raman, 2002, "Microstructural Variations in a High-Strength Structural Steel Weld under Isoheat Input Conditions", *Welding Journal*, pp. 239-S – 248-S.

3. J.T. McGrath, J.A. Gianetto, R.F. Orr, and M.W. Letts, 1986, "Factors Affecting the Notch Toughness Properties of High Strength HY80 Weldments", *Canadian Metallurgical Quarterly*, Vol. 25, No. 4, pp. 349-356.

4. R.B. Lazor and H.W. Kerr, 1980, "The Effects of Nickel and Titanium on Submerged Arc Welds in HSLA Steels"*, Pipeline and Energy Plant Piping: Design and Technology*, pp. 141-149.

5. N.H. Croft, J.M. Gray, and A.J. DeArdo, 1984, "Submerged Arc Weld Metal Toughness in Microalloyed Linepipe Steels – The Effects of Post Weld Heat Treatment", *HSLA Steels, Technology & Applications: Conference Proceedings of International conference on Technology and Applications of HSLA Steels*, Philadelphia, Pennsylvania, pp. 897-913.

6. J.F. Lancaster, 1999, *Metallurgy of Welding*, Abington Publishing, Cambridge, England, pp. 130-247.

7. C.B. Dallam, S. Liu, and D.L. Olson, 1985, "Flux Composition Dependence of Microstructure and Toughness of Submerged Arc HSLA Weldments", *Welding Journal*, Vol. 64, No. 5, pp. 140-s - 151-s.

8. S.S. Babu, 2004, "The Mechanism of Acicular Ferrite in Weld Deposits", *Current Opinion in Solid State and Materials Science 8*, pp. 267-278.

9. M. Eroglu and M. Aksoy, 2000, "Effect of Initial Grain Size on Microstructure and Toughness of Intercritical Heat-Affected Zone of a Low Carbon Steel"*, Materials Science and Engineering*, Vol. A286, pp. 289-297.

10. P. Deb, K.D. Challenger, and A.E. Therrien, 1987, "Structure-Property Correlation of Submerged-Arc and Gas-Metal-Arc Weldments" in *HY-100 Steel, Metallurgical Transactions A: Physical Metallurgy & Materials Science*, Vol. 18A, No. 6, pp. 987-999.

11. N.D. Pandey, A. Bharti, and S.R. Gupta, 1994, "Effect of Submerged Arc Welding Parameters and Fluxes on Element Transfer Behaviour and Weld-Metal Chemistry", *Journal of Materials Processing Technology*, Vol. 40, pp. 195-211.

12. A. Murray, J. Norrish, and J. Billingham, 1996, "Assessing Offshore Submerged Arc Weld Metals", *Welding & Metal Fabrication*, Vol. 64, No. 7, pp. 267-274.

13. M. Vilpas, H. Tihekari, and R. Karppi, 1985, *Mechanical properties of SMA- and SA-welded joints for quenched and tempered high-strength steel N-A-EXTRA 70*, Espoo, VTT, Tutkimuksia (Research)/Technical Research Centre of Finland; Research Reports 363, pp. 1-26.

14. N.J. Smith, J.T. McGrath, J.A. Gianetto, and R.F. Orr, 1989, "Microstructure/Mechanical Property Relationships of Submerged Arc Welds in HSLA 80 Steel", *Welding Journal*, Vol. 68, No. 3, pp. 112-120.

15. T.U. Marston and W. Server, 1978, "Assessment of Weld Heat-Affected Zones in a Reactor Vessel Material", *Journal of Engineering Materials and Technology*, Vol. 100, No. 3, pp.267-271.

16. Y. Yang, 2008, "The Effect of Submerged Arc Welding Parameters on the Properties of Pressure Vessel and Wind Turbine Tower Steels", Thesis (M.Sc.), University of Saskatchewan, Saskatoon, Saskatchewan.

17. H. Huang, W. Tsai, and J. Lee, 1994, "The Influences of Microstructure and Composition on the Electrochemical Behavior of A516 Steel Weldment", *Corrosion Science*, Vol. 36, No. 6, pp. 1027-1038.

18. D.V. Dorling, P.E.L.B. Rodrigues, and J.H. Rogerson, 1976, "A Comparison of the Toughness of Self-Shielded Arc and Submerged-Arc Weld Metals in C-Mn-Nb Steels: Part 1. Effect of Consumables and Process Variables on Weld Metal Toughness", *Welding and Metal Fabrication*, Vol. 44(6), pp. 419-423.

19. J.T. McGrath, R.S. Chandel, R.F. Orr, and J.A. Gianetto, 1988, "Microstructure/Mechanical Property Relationships in Thick-Section C-Mn Narrow-Groove Welds: With a Careful Control of Welding Wire Chemistry and Flux Basicity, Optimum Strength and Toughness were Achieved in Pressure Vessel Steel", *Welding Journal*, V. 67, No. 9, pp. 196-201.

20. J.M. Aurrecoechea, B. Qain, and A.W. Pense, 1987, "The Fracture Behavior of ASTM A737 Grade B and Grade C Microalloyed Steel Weldments", *Welding Research Council Bulletin*, pp. 23-32.

21. J. Liao, K. Ikeuchi, and F. Matsuda, 1998, "Toughness Investigation on Simulated Weld HAZs of SQV-2A pressure vessel steel", *Nuclear Engineering and Design*, Vol. 183, pp. 9-20.

22. J.T. McGrath, R. S. Chandel, R.F. Orr, and J.A. Gianetto, 1989, "A Review of Factors Affecting the Structural Integrity of Weldments in Heavy Wall Reactor Vessels", *Canadian Metallurgical Quarterly*, Vol. 28, No. 1, pp. 75-83.

23. Precision Grinding, Inc., 2009, A516 Steelplate.com., website cited ASTM specifications, http://www.a516steelplate.com/, [Accessed January 10, 2010].

24. J.H. Yoon, B.S. Lee, Y.J. Oh, and J.H. Hong, 1999, "Effects of Loading Rate and Temperature on J-R Fracture Resistance of an SA516-Gr. 70 Steel for Nuclear Piping", *International Journal of Pressure Vessels and Piping*, Vol. 76, pp. 663-670.

25. Oakley Steel Limited, 2009, *ASTM / ASTM A / SA 516 – Home*. http://www.oakleysteel.co.uk/asme_sa_516.htm, [Accessed January 10, 2010].

26. E. Keehan, L. Karlsson, H.O. Andren, and H.K.D.H. Bhadeshia, 2005, "Understanding Mechanical Properties of Novel High Strength Steel Weld Metals Through High-Resolution Microstructural Investigations", *Proceedings of the 7th International Conference on Trends in Welding Research,* Callaway Gardens Resort, Pine Mountain, Georgia, USA, pp. 969-974.

27. Metals Handbook: Properties and Selection: *Irons, Steels and High-Performance Alloys*, 1990, Vol. 1, ASM International, Materials Park, OH, pp. 389-423.

28. W. Wang and S. Liu, 2002, "Alloying and Microstructural Management in Developing SMAW Electrodes for HSLA-100 Steel", *Welding Journal*, Vol. 81, No. 7, pp. 132-s - 145-s.

29. J.R. Davis, 2001, *Alloying: Understanding the Basics*, ASM International, Materials Park, Ohio, USA, pp. 193-206.

30. K.E. Dorschu, and R.D. Stout, 1961, "Some factors affecting the notch toughness of steel weld metal", *Welding Journal*, pp. 97-s-105-s.

31. Farag, Mahmoud M., 1997, *Materials Selection for Engineering Design*, Upper Saddle River, NJ, Prentice Hall, pp. 40-41, 95-97.

32. Bull, Steve, 1997, "Steels", Staff Personal Home Pages University of Newcastle, http://www.staff.ncl.ac.uk/s.j.bull/mmm211/STEEL/sld033.htm, [Accessed January 10, 2010].

33. The Lincoln Electric Company, 1994, Arc-Welding Fundamentals, http://www.lincolnelectric.com/knowledge/articles/content/arcweldfund.asp , [Accessed January 10, 2010].

34. Clark, Donald S., Varney, and Wilbur R., 1952, *Physical Metallurgy for Engineers,* D. Van Nostrand Company Inc., Princeton, New Jersey, pp. 81-99, 462-478.

35. Metals Handbook, 1971, *Welding and Brazing*, Vol. 6, American Society for Metals, Metals Park, Ohio, pp. 1, 2, 24, 25, 46, 47, 58, 59, 77-79, 207-210.

36. ESDEP, Fabrication and Erection Lecture 3.3: Principles of Welding, http://www.fgg.uni-lj.si/kmk/esdep/master/wg03/l0300.htm, [Accessed January 10, 2010].

37. The ESAB Group, 1998, ESAB University, Lesson 2 – Common Electric Arc Welding Processes, http://www.esabna.com/EUWeb/AWTC/Lesson2_31.htm , [Accessed January 10, 2010].

38. WikiAnswers, 2009, Submerged Arc Welding. http://www.answers.com/submerged+arc+welding&r=67, [Accessed January 10, 2010].

39. Bavaria Schweisstechnik, Submerged Arc Welding – Wire/Flux (EN/AWS), http://www.subarcflux.com/web/index.php, [Accessed January 10, 2010].

40. C.V. Robino. R. Varughese, A.W. Pense, and R. C. Dias, 1988, "The Fracture Behavior of A588 Grade A and A572 Grade 50 Weldments", *Welding Research Council Bulletin*, Issue 330, pp. 1-10.

41. S.K. Sen, S.K. Dhua, D. Mukherjee, S. Mishra, and B.B. Rath, 1993, "Toughness and Microstructural Characteristics in Submerged Arc Welded HSLA-80 Grade Steel", *Key Engineering Materials*, Vol. 84-85, pp. 602-626.

42. S. D., Bhole and J. Billingham, 1983, "Effect of Heat Input on HAZ Toughness in HSLA Steels", *Metals Technology*, Vol. 10, No. 9, pp. 363-367.

43. W. Lei, Y. Su and M. Yao, 1996, "Dynamic Fracture Behaviour of Simulated Weld Heat Affected Zone of a High Strength Low Alloy Steel", *Steel Research*, Vol. 67, No. 12, pp. 555-557.

44. I. De S Bott, 2003, "High Grade Steel Development", *Materials Science Forum*, Vol. 426, No. 2, pp. 1463-1468.

45. N.U. Ahmed and J.M. Yellup, 1988, "The Effect of High Heat Input Welding on the HAZ Toughness of Three Nb-Ti Based HSLA Steels", *Materials Forum*, Vol. 12, pp. 62-72.

46. J. Neves and A. Loureiro, 2004, "Fracture Toughness of Welds – Effect of Brittle Zones and Strength Mismatch", *Journal of Materials Processing Technology*, Vol. 153-154, pp. 537-543.

47. M. Gräf and K. Niederhoff, undated, "Properties of HAZ in Two-Pass Submerged Arc Welded Large-Diameter Pipe", *Europipe*, Germany, http://www.bergpipe.com/files/ep_tp_29_00_en.pdf, pp. 1-14, [Accessed January 10, 2010].

48. A. Price, 2001, "Significant System Parameters Influencing HAZ Properties in 9% Ni Steel", *Science and Technology of Welding and Joining*, Vol. 6, No. 4, pp. 255-260.

49. S. Lee, B.C. Kim, and D. Kwon, 1992, "Correlation of Microstructure and Fracture Properties in Weld Heat-Affected Zones of Thermomechanically Controlled Processed Steels", *Metallurgical Transactions A*, Vol. 23A, pp. 2803-2816.

50. W. Burget and J.G. Blauel, 1990, "Fracture Toughness of Manual Metal-Arc and Submerged-Arc Welded Joints in Normalized Carbon-Manganese Steels", *Fatigue and Fracture Testing of Weldments*, *ASTM STP 1058*, pp. 272-299.

51. A. Moitra, P.R. Sreenivasan, P. Parameswaran, and S.L. Mannan, 2002, "Dynamic Deformation and Fracture Properties of Simulated Weld Heat Affected Zone of 9Cr-1Mo Steel from Instrumented Impact Tests", *Materials Science and Technology*, Vol. 18, pp. 1195-1200.

52. B.C. Kim, S. Lee, N.J. Kim, and D.Y. Lee, 1991, "Microstructure and Local Brittle Zone Phenomena in High-Strength Low-Alloy Steel Welds", *Metallurgical Transactions A: Physical Metallurgy Materials Science*, Vol. 22A, pp. 139-149.

53. S. Lee, B.C. Kim, and D.Y. Lee, 1989, "Fracture Mechanism in Coarse Grained HAZ of HSLA Steel Welds", *Scripta Metallurgica*, Vol. 23, No. 6, pp. 995-1000.

54. P. Sundaram, R.K. Pandey, and A.N. Kumar, 1987, "Effect of the Welding Process and Heat Input on the Fracture Toughness of Welded Joints in High Strength Low Alloy Steel", *Materials Science and Engineering*, Vol. 91, pp. 29-38.

55. JY Koo and A. Ozekcin, 1987, "Local Brittle Zone Microstructure and Toughness in Structural Steel Weldments", *Welding Metallurgy of Structural Steels*, Vol. 22-26, pp. 119-135.

56. J.X. Zhang and Y.W. Shi, 1997, "The Effect of Welding Mechanical Heterogeneity on Fracture Toughness Feature of Base Metal", *Int. J. Pres. Ves. & Piping*, Vol. 72, pp. 199-202.

57. A. Gural, B. Bostan, and A.T. Özdemir, 2005, "Heat Treatment in Two Phase Region and its Effect on Microstructure and Mechanical Strength after Welding of a Low Carbon Steel", *Materials and Design*, pp. 1-7.

58. C.S. Lee, R.S. Chandel, and H.P. Seow, 2000, "Effect of Welding Parameters on the Size of Heat Affected Zone of Submerged Arc Welding", *Materials and Manufacturing Processes*, Vol. 15, No. 5, pp. 649-666.

59. Horwitz, H., 1979, *Welding Principles and Practice*, Houghton Mifflin Company, Boston, USA, pp.93, 482 - 570.

60. V. Tsegelsky, c. 1963, *The Electric Welder (A Manual)*, B. Kuznetsov , trans., Foreign Languages Publishing House, Moscow, pp. 89.

61. D.W. Moon, R.W. Fonda, and G. Spanos, 2000, "Microhardness Variations in HSLA-100 Welds Fabricated with New Ultra-Low-Carbon Weld Consumables", *Welding Journal*, pp. 278-s-285-s.

62. V.S.R. Murti, P.D. Srinivas, G.H.D. Banadeki, and K.S. Raju, 1993, "Effect of Heat Input on the Metallurgical Properties of HSLA Steel in Multi-Pass MIG Welding", *Journal of Materials Processing Technology*, Vol. 37, pp. 723-729.

63. TWI Ltd., 2004, Defects/imperfections in welds - porosity http://www.twi.co.uk/content/jk42.html, World Centre for Materials Joining Technology, [Accessed January 10, 2010].

64. BB Welding Services, 2009, NDE Test Specimens, http://www.bbweldingservices.co.uk/Test_Specimens/test_specimens.htm, [Accessed January 10, 2010].

65. ASM International, 2000, *ASM Handbook Volume 8: Mechanical Testing and Evaluation,* ASM International, Materials Park, Ohio, pp. 596-604.

66. W.H. Funk, 1968, Welding of Heat Treated Carbon Steel Plate, In American Society for Metals (Ed.), *Welding high strength steels*, American Society for Metals, Metals Park, Ohio, pp. 13-17.

67. V. Gunaraj and N. Murugan, 2002, "Prediction of Heat-Affected Zone Characteristics in Submerged Arc Welding of Structural Steel Pipes", *Welding Journal*, pp. 94-s-98-s.

68. V. Gunaraj and N. Murugan, 1999, "Application of Response Surface Methodology for Predicting Weld Bead Quality in Submerged Arc Welding of Pipes", *Journal of Materials Processing Technology*, Vol. 88, Iss. 1-3, pp. 266-275.

69. P. Yongyuth, P.K. Ghosh, P.C. Gupta, A.K. Patwardhan, and S. Prakash, 1992, "Influence of Macro/Microstructure on the Toughness of 'All Weld' Multipass Submerged Arc Welded C-Mn Steel Deposits", *ISIG International*, Vol. 32, No. 6, pp. 771-778.

70. R.S. Funderburk, 1999, "Key Concepts in Welding Engineering: A Look at Heat Input", *Welding Innovation*, Vol. 16, No. 1, Online Version, http://www.jflf.org/pdfs/papers/keyconcepts2.pdf , [Accessed January 10, 2010].

71. H. B. Cary, 1998, *Modern Welding Technology*, Fourth Edition, Prentice Hall, New Jersey, pp. 454, 470.

72. P.K. Ghosh, P.K. Singh, and N.B. Potluri, 1998, "Fracture Properties of Multipass Submerged Arc Weld of HSLA Steel Produced by Using Flux Cored Filler Wire", *ISIJ International*, Vol. 38, No. 12, pp. 1379-1386.

73. Wulff, Taylor and Shaler, 1952, *Metallurgy for Engineers Casting, Welding and Working*, John Wiley & Sons, New York, pp. 441-457.

74. K.Y. Benyounis, A.G. Olabi, and M.S.J. Hashmi, 2005, "Effect of Laser Welding Parameters on the Heat Input and Weld-Bead Profile", *Journal of Materials Processing Technology*, Vol. 164-165, pp. 978-985.

75. *Welding Handbook: Welding Processes*, 1987, Vol. 2, American Welding Society, Miami, FL, pp. 5-6, 212-215.

76. N. Murugan and V. Gunaraj, 2005, "Prediction and Control of Weld Bead Geometry and Shape Relationships in Submerged Arc Welding of Pipes", *Journal of Materials Processing Technology*, Vol. 168, pp. 478-487.

77. V. Gunaraj and N. Murugan, 2000, "Prediction and Optimization of Weld Bead Volume for Submerged Arc Process – Part 1", *Welding Research Supplement*, pp. 286-s – 294-s.

78. Lincoln Electric Company, 1973, "*Lincoln Procedure Handbook of Arc Welding*", 12th Edition, Lincoln Electric Company, Cleveland, Ohio, Section 6.3.

79. E. Karadeniz, U. Ozsarac, and C. Yildiz, 2005, "The Effect of Process Parameters on Penetration in Gas Metal Arc Welding Processes", *Materials and Design*, pp. 1-8.

80. ESAB Submerged Arc Fluxes, OK Flux 10.72, AWS A5.17; Classes F7A6-EM12K-H8; CWB-SCA 48-01; Class F49A5-EM12K, 2005.

81. Annual Book of ASTM Standards, 1997, *Metals Test Methods and Analytical Procedures,* Section 3, Vol. 03.01, A 370-97a, ASTM International, PA, USA, pp. 107-159.

82. Annual Book of ASTM Standards, 1993, *Metals Test Methods and Analytical Procedures,* Section 3, Vol. 03.01, E 23-93a, ASTM International, Easton, USA, pp. 206-224.

83. American Welding Society, 2002, *Structural Welding Steel Code – Steel*, ANSI / AWS D1.1/D1.1M, Annex III, pp. 273.

84. J. Vercesi and E. Surian, 1998, "The Effect of Welding Parameters on High-Strength SMAW All-Weld-Metal- Part 2: AWS E10018-M and E12018-M", *Welding Research Supplement*, pp. 164-s-171-s.

85. Impact testing requirements provided by Hitachi, 2004, “Quality Specification”, source confidential.

APPENDIX A. Tensile Data

The stress vs strain curves for the three welding speeds are shown in Figures A.1 through A.7. The tensile strength and 0.2% yield strength were calculated from these curves. The three 9.3 mm/s test specimens were labelled RC1, RC3, and RC6. The three 12.3 mm/s test specimens were labelled GC2, GC4, and GC5. The three 15.3 mm/s test specimens were labelled AC7, AC8, and AC9. The three parent metal test specimens cut in the transverse direction were labelled YC10, YC11, and YC12 and cut in the longitudinal direction YD13, YD14, and YD15.

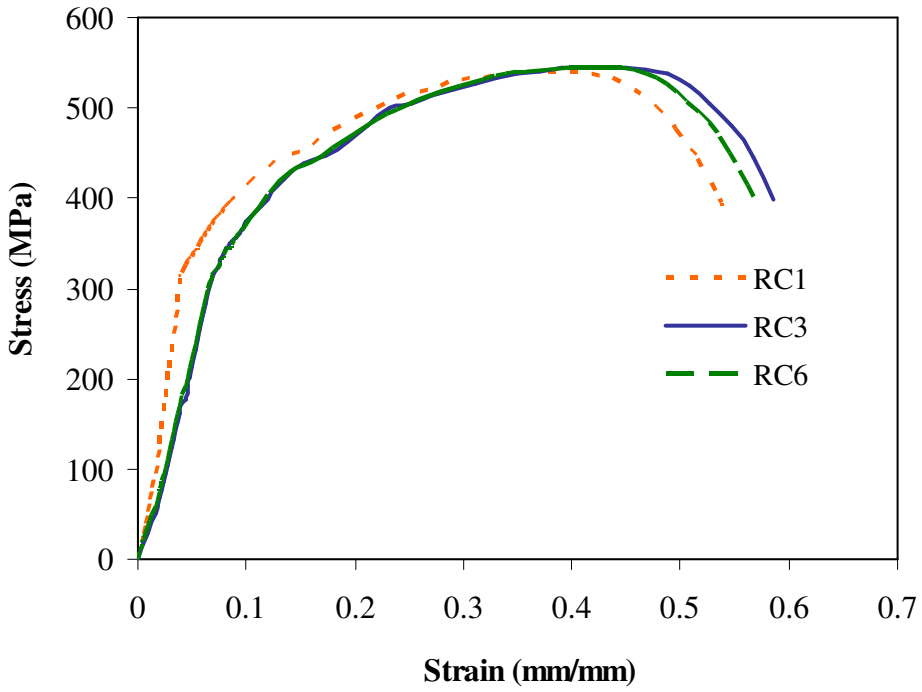

Figure A.1. Stress-Strain Curves for the 3, 9.3 mm/s welding speed specimens.

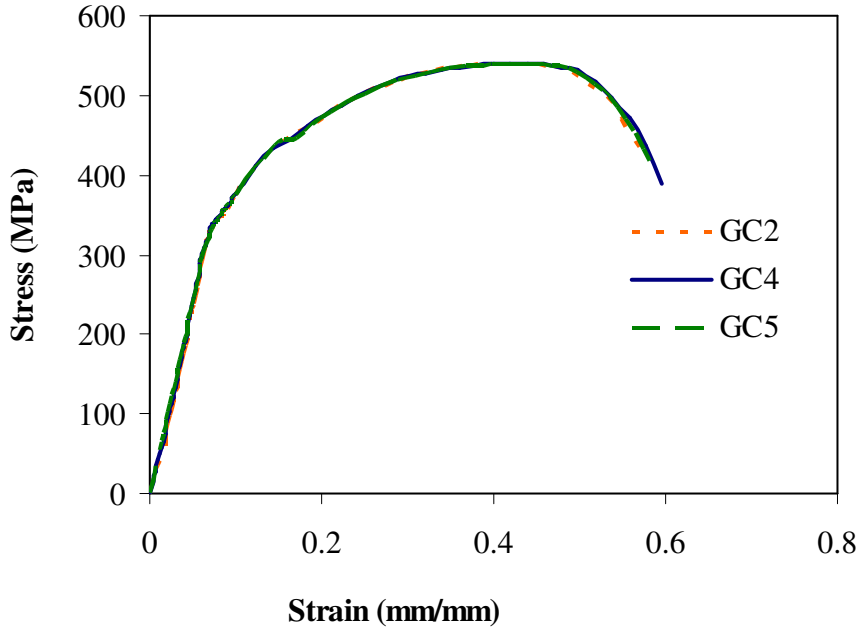

Figure A.2. Stress-Strain Curves for the 3, 12.3 mm/s welding speed specimens.

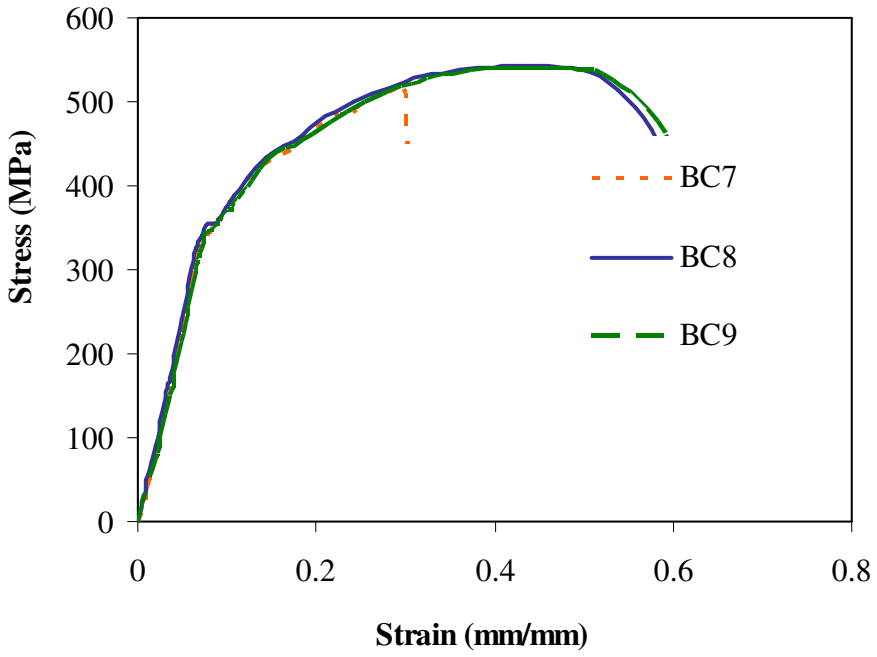

Figure A.3. Stress-Strain Curves for the 3, 15.3 mm/s welding speed specimens.

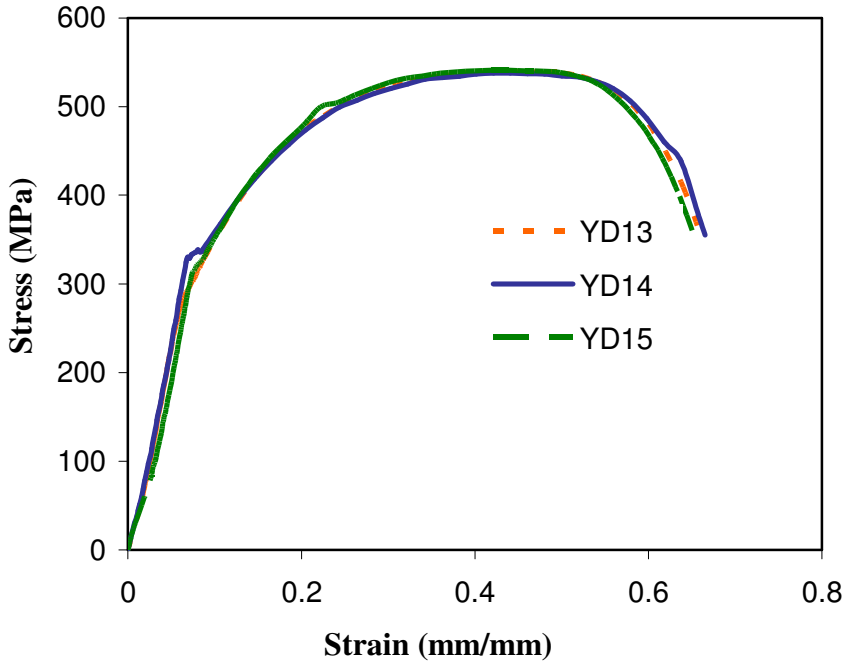

Figure A.4. Stress-Strain Curves for the 3 longitudinally cut PM specimens.

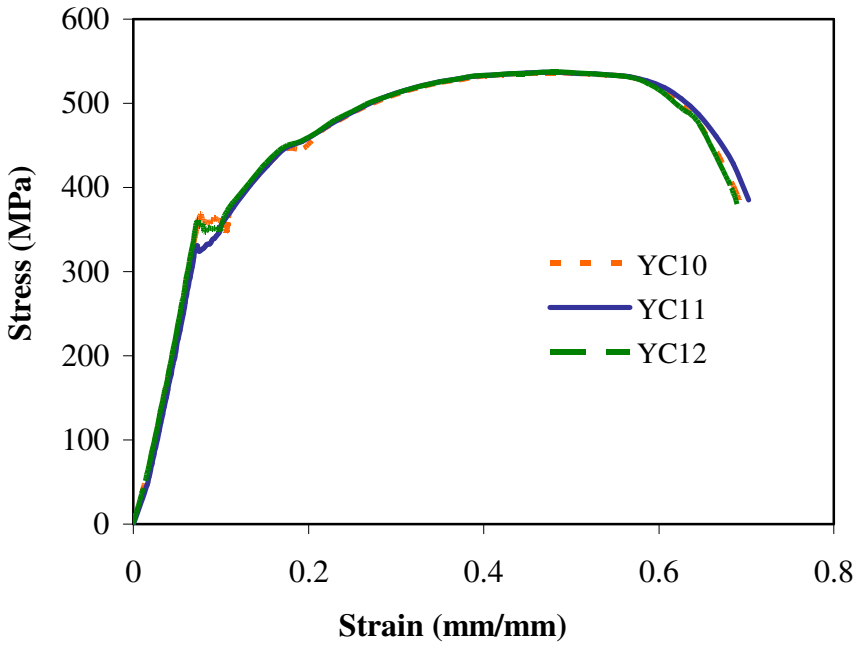

Figure A.5. Stress-Strain Curves for the 3 transverse cut PM specimens.

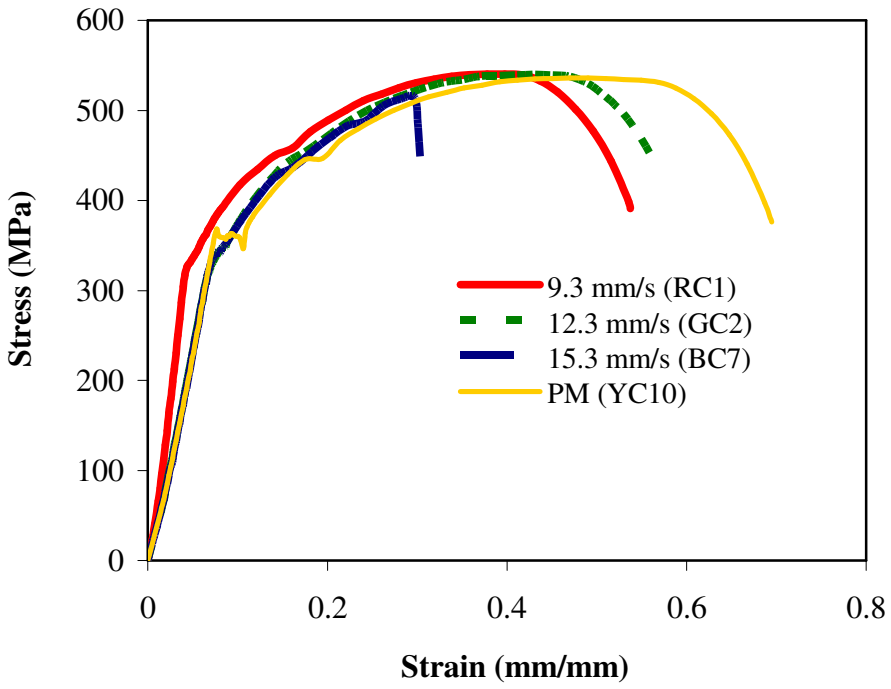

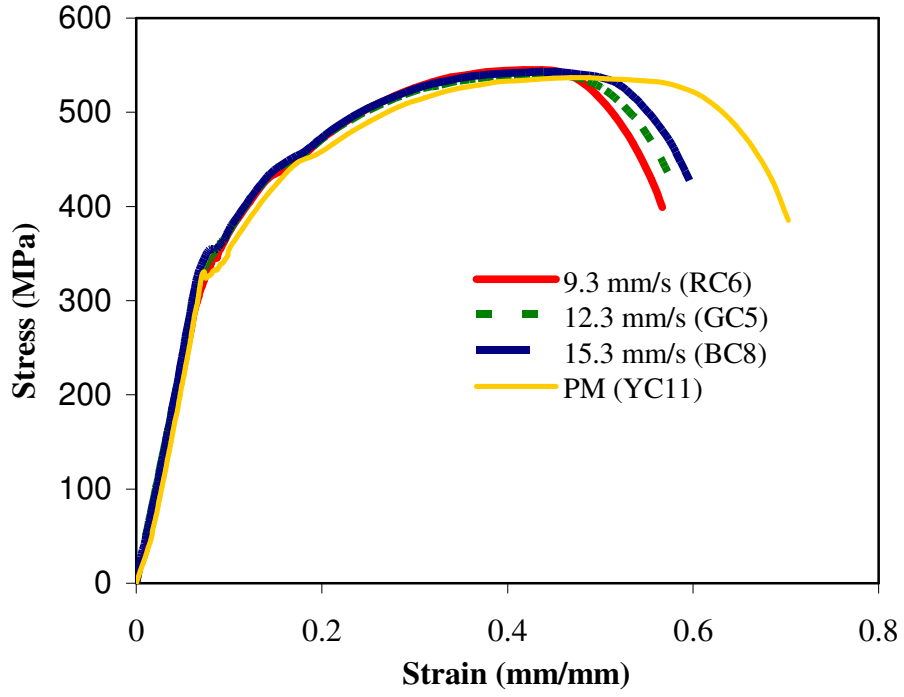

Figure A.6. Stress-Strain Curves comparing the 3 welding speed specimens.

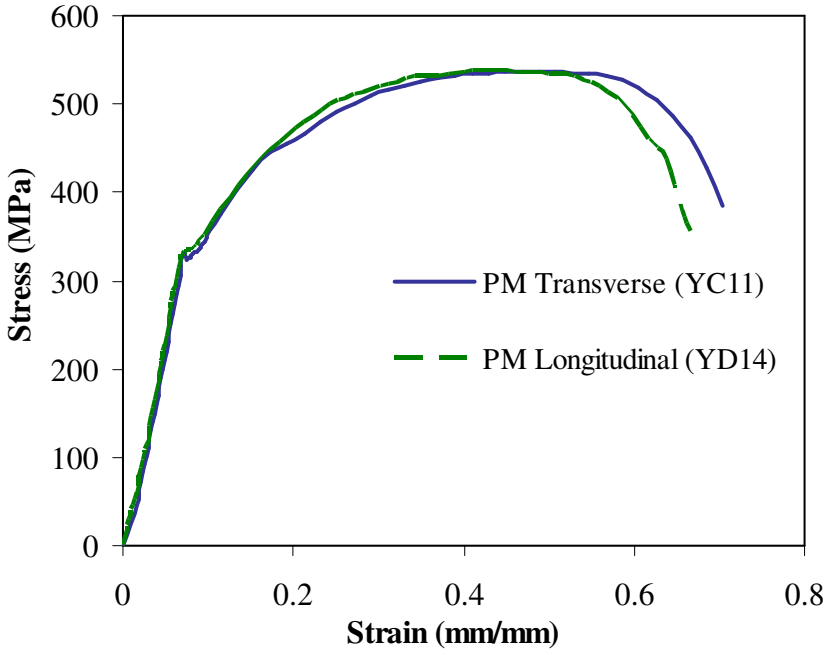

Figure A.7. Stress-Strain Curves for the transverse and longitudinal specimens.

APPENDIX B. Optical Micrographs of Weld Zones

Figures B.1 through B.18 show the micrographs taken for the different zones of the welds for each of the three welding speeds.

9.3 mm/s Welding Speed:

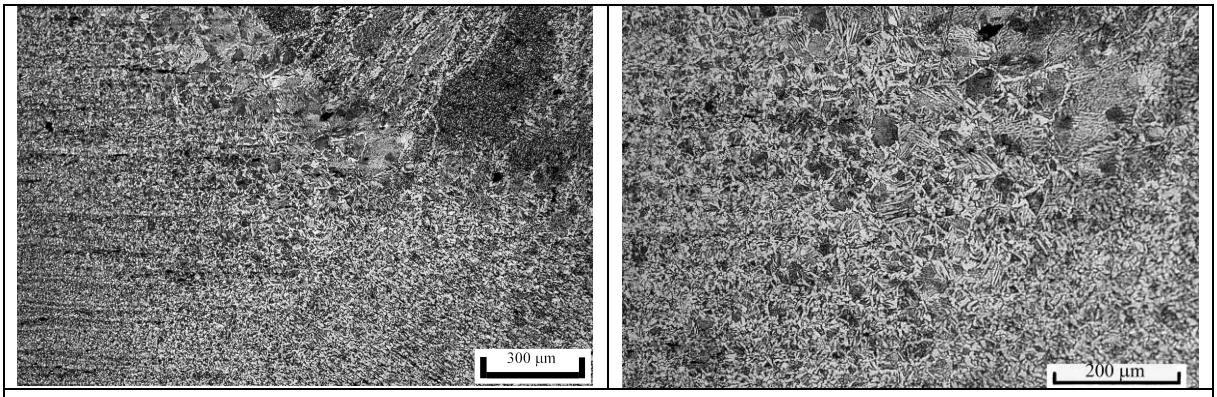

Figure B.1. HAZ 9.3 mm/s welding speed.

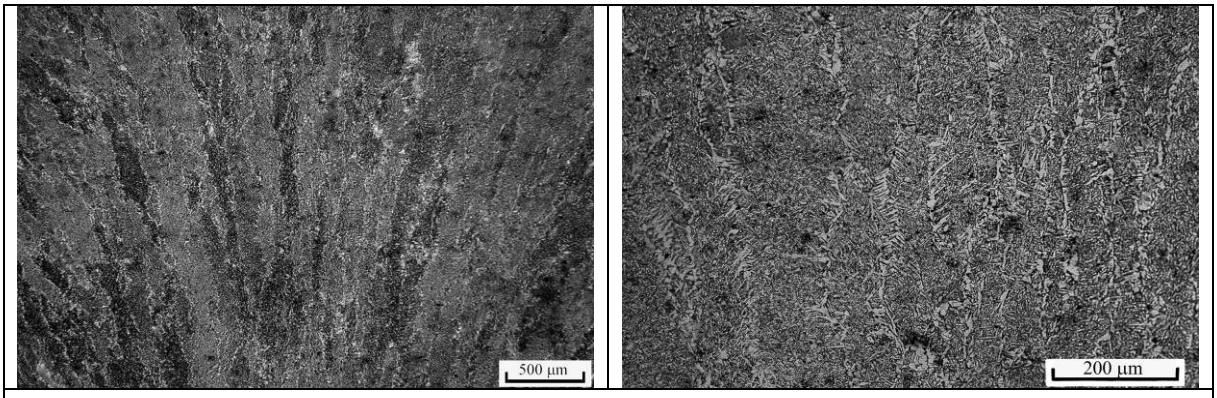

Figure B.2. WM 1st pass for 9.3 mm/s welding speed.

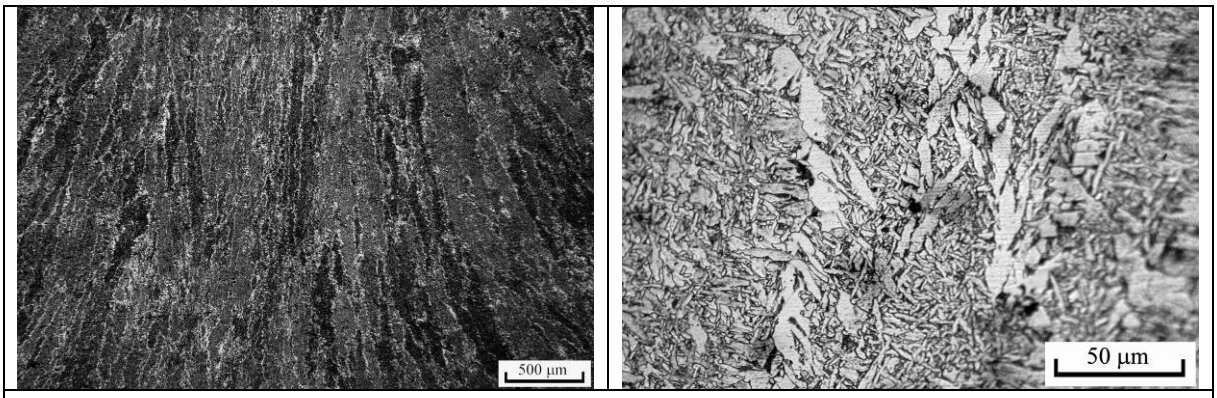

Figure B.3. WM 2nd pass for 9.3 mm/s welding speed.

Figure B.4. Interface between the 1st and 2nd pass welds for 9.3 mm/s welding speed.

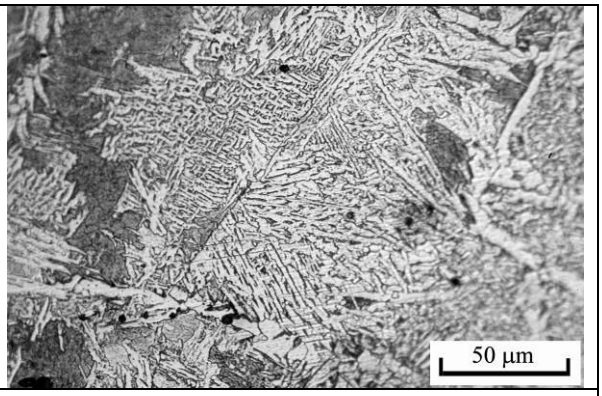

Figure B.5. Interface between the WM and HAZ for 9.3 mm/s welding speed.

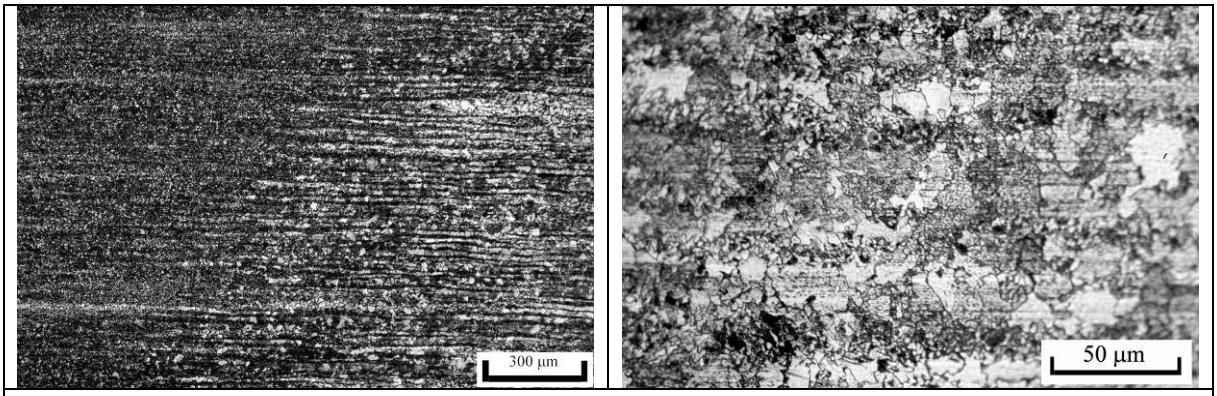

Figure B.6. Interface between the HAZ and PM for 9.3 mm/s welding speed.

12.3 mm/s Welding Speed.

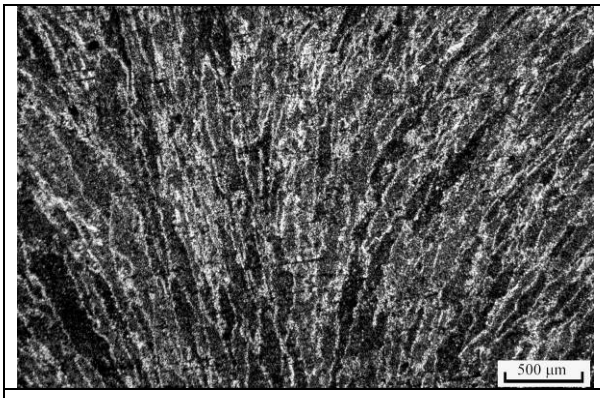

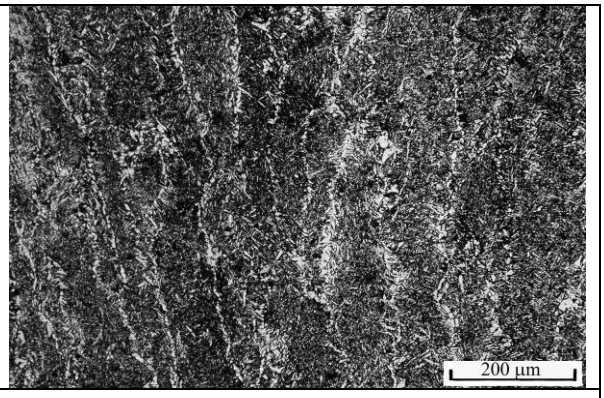

Figure B.7. WM 1st pass for 12.3 mm/s welding speed.

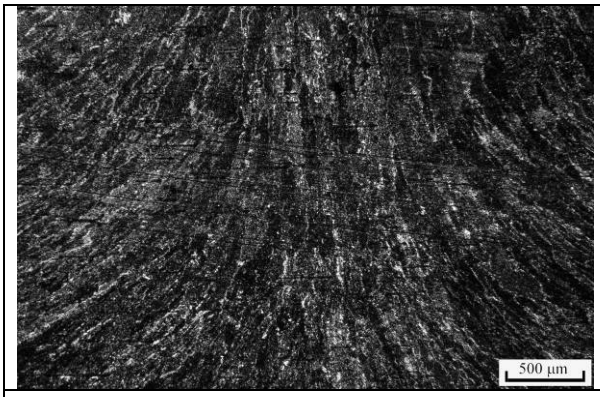

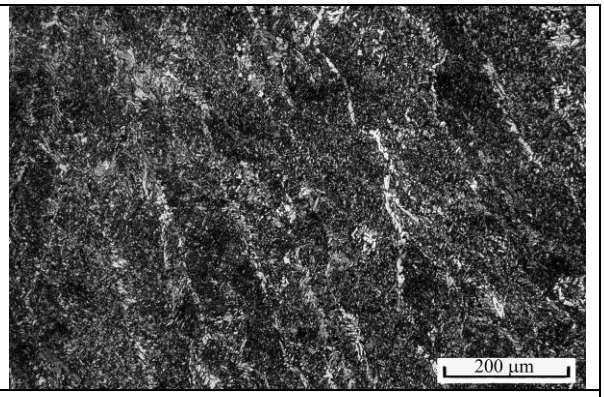

Figure B.8. WM 2nd pass for 12.3 mm/s welding speed.

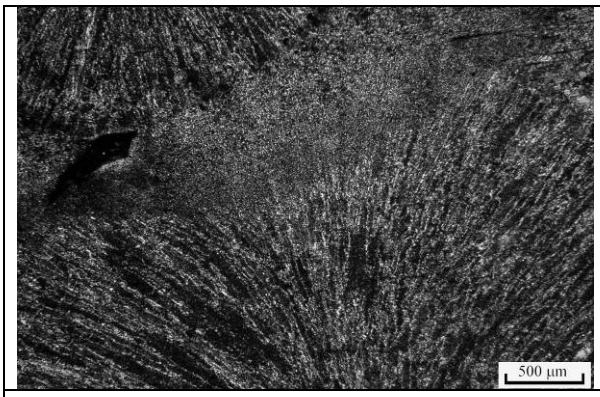

Figure B.9. Interface between the 1st and 2nd pass welds for 12.3 mm/s welding speed.

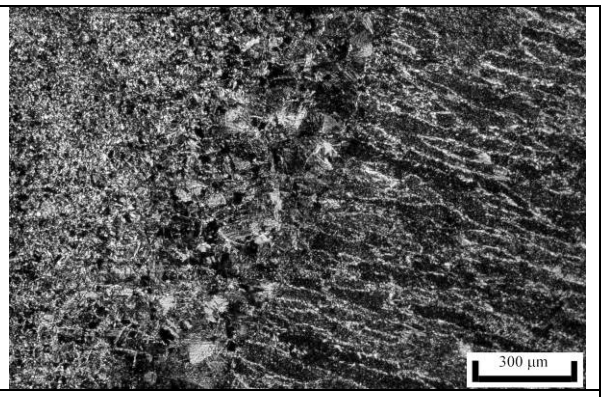

Figure B.10. Interface between the WM and HAZ for 12.3 mm/s welding speed.

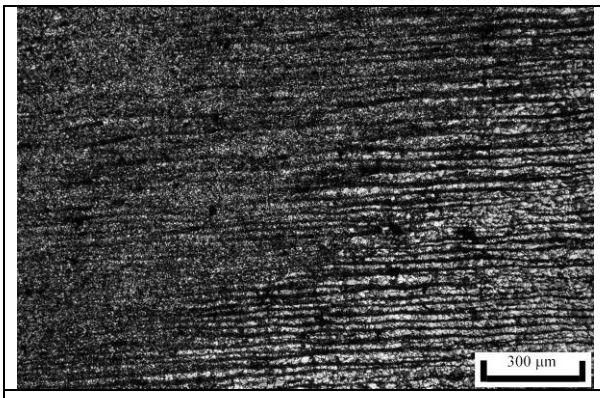

Figure B.11. Interface between the HAZ and PM for 12.3 mm/s welding speed.

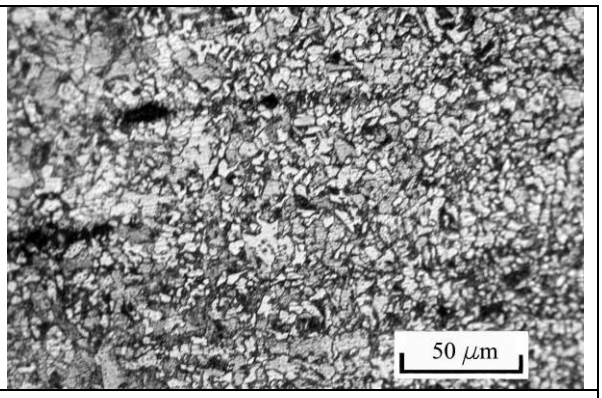

Figure B.12. Fine grained HAZ for the 12.3 mm/s welding speed.

15.3 mm/s Welding Speed.

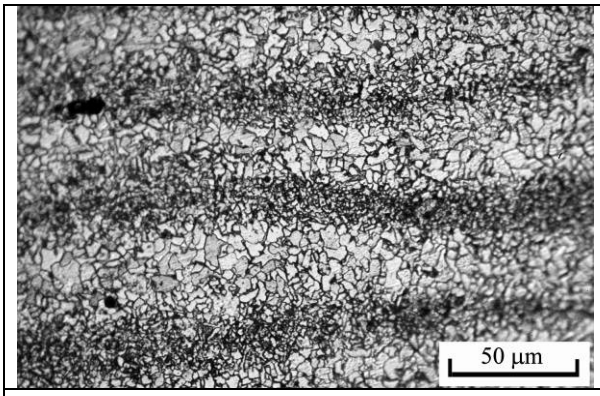

Figure B.13. Fine-grained HAZ 15.3 mm/s welding speed.

Figure B.14. Interface between the 1st and 2nd pass welds for 15.3 mm/s welding speed.

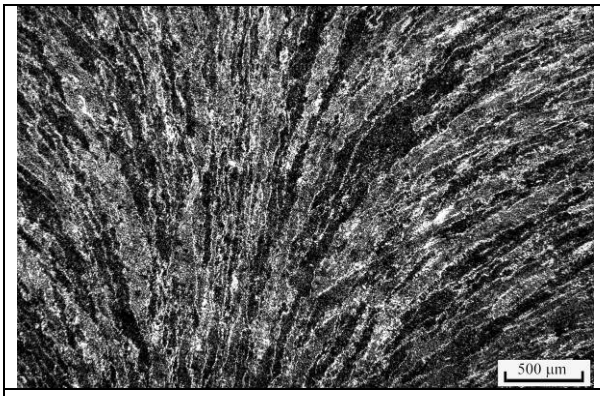

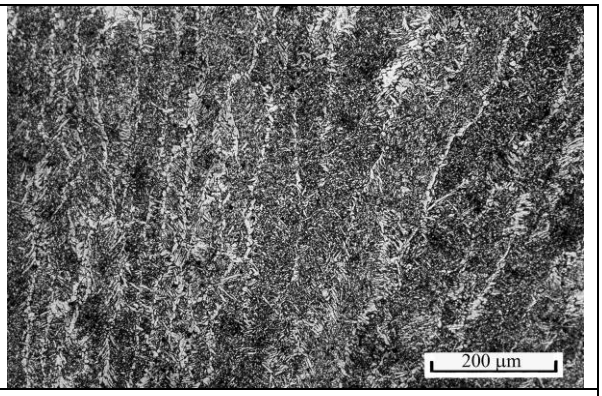

Figure B.15. WM 1st pass for 15.3 mm/s welding speed.

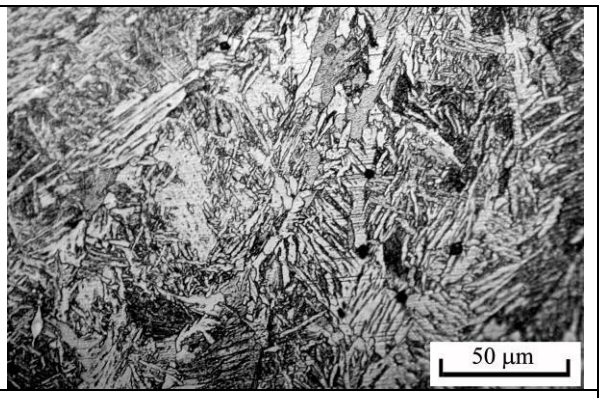

Figure B.16. WM 2nd pass for 15.3 mm/s welding speed.

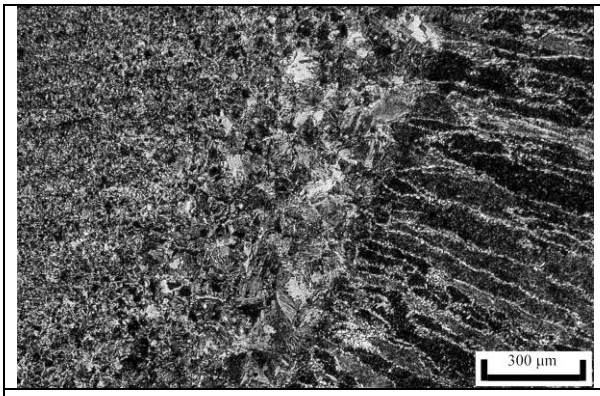

Figure B.17. Interface between the WM and HAZ for 15.3 mm/s welding speed.

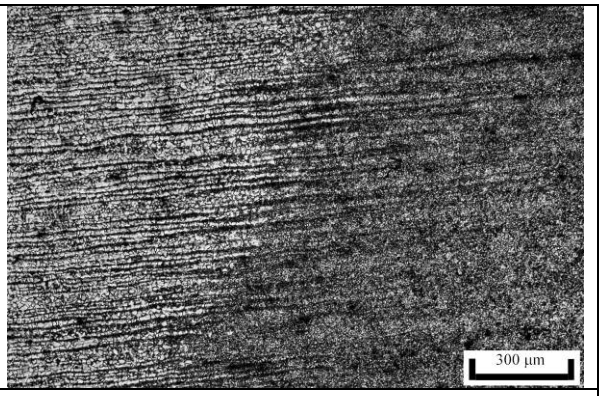

Figure B.18. Interface between the HAZ and PM for 15.3 mm/s welding speed.

APPENDIX C. Charpy Fracture Surface Photographs

Charpy fracture surface photographs are shown in Figures C.1 – C.6 for welding speeds 9.3 mm/s, 12.3 mm/s, and 15.3 mm/s for specimens notched in the WM and the HAZ. Specimens representing ductile fracture, mixed fracture, and brittle fracture are shown.

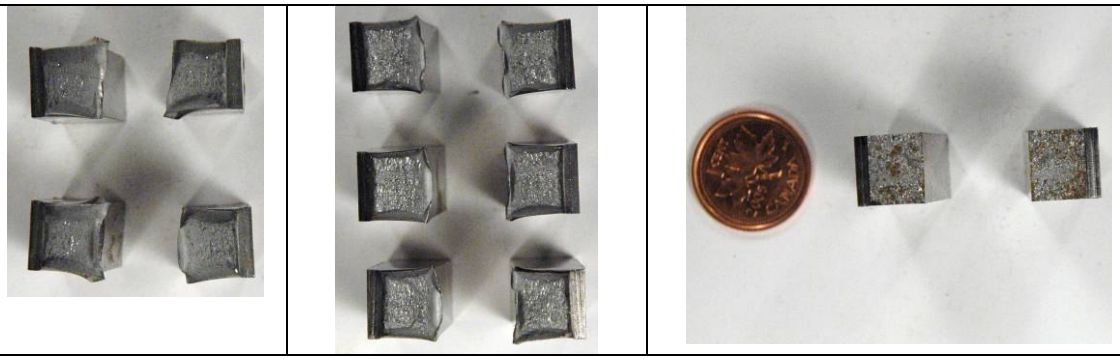

Figure C.1. 9.3 mm/s specimens, notched in the WM, broken at 97°C, 22°C and – 190°C.

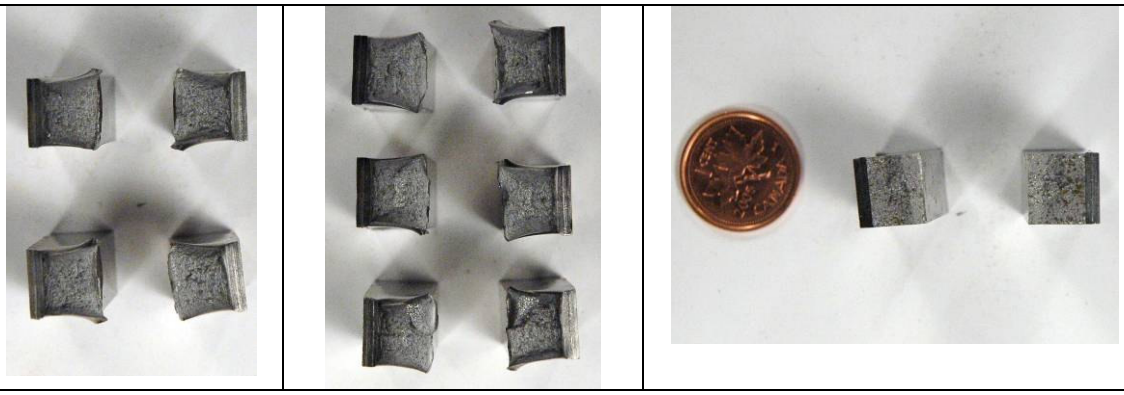

Figure C.2. 9.3 mm/s specimens, notched in the HAZ, broken at 97°C, 22°C and – 190°C.

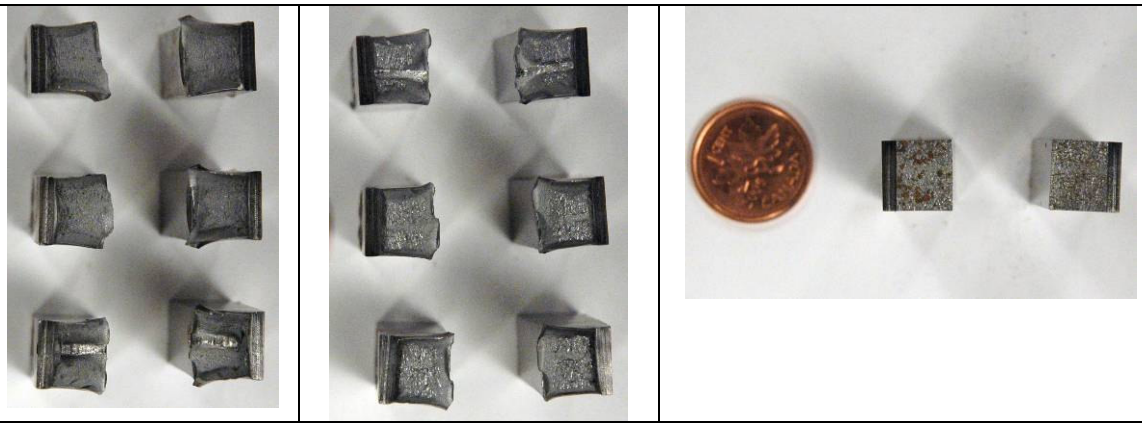

Figure C.3. 12.3 mm/s specimens, notched in the WM, broken at 97°C, 22°C and – 190°C.

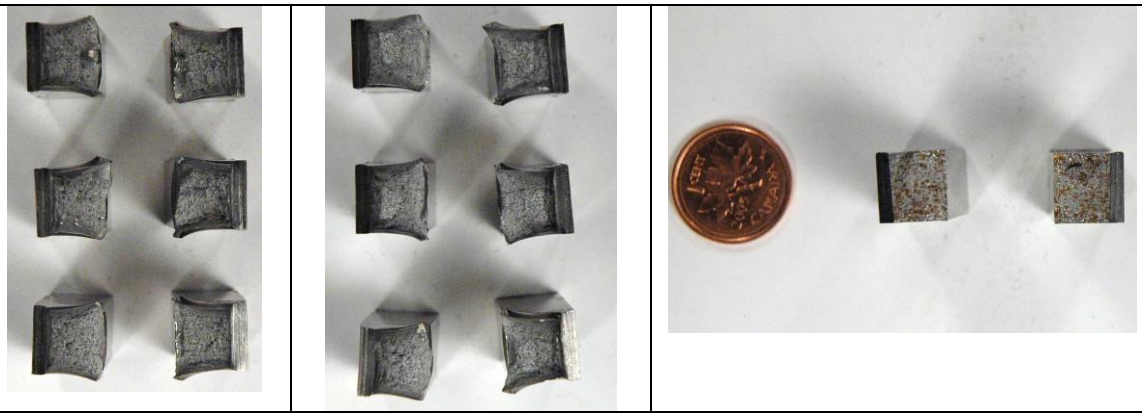

Figure C.4. 12.3 mm/s specimens, notched in the HAZ, broken at 97°C, 22°C and – 190°C.

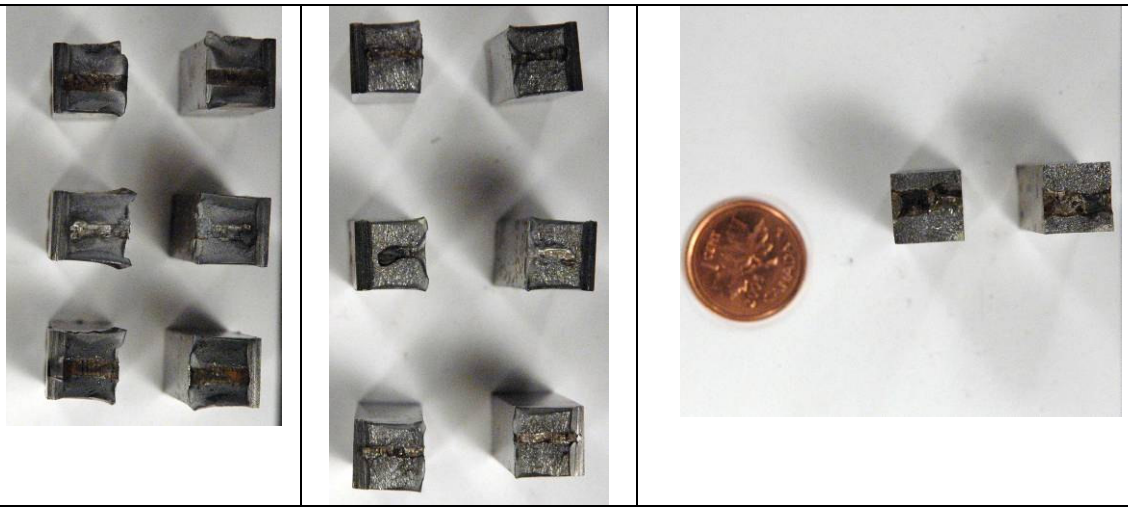

Figure C.5. 15.3 mm/s specimens, notched in the WM, broken at 97°C, -27°C and – 190°C.

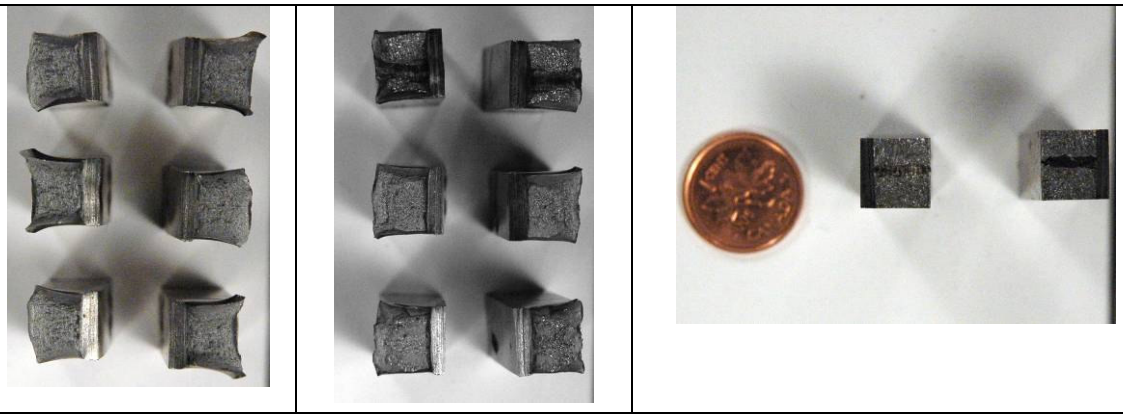

Figure C.6. 15.3 mm/s specimens, notched in the HAZ, broken at 97°C, -27°C and – 190°C.

APPENDIX D. SEM Fractographs

SEM Fractographs of the fracture surfaces of the Charpy specimens notched in the HAZ and specimens notched in the WM of the 9.3, 12.3, and 15.3 mm/s welding speeds are displayed in Figures D.1 – D.6. Figures D.1 and D.4 show ductile fracture, Figures D.2 and D.5 show mixed fracture and Figures D.3 and D.6 show brittle fracture.

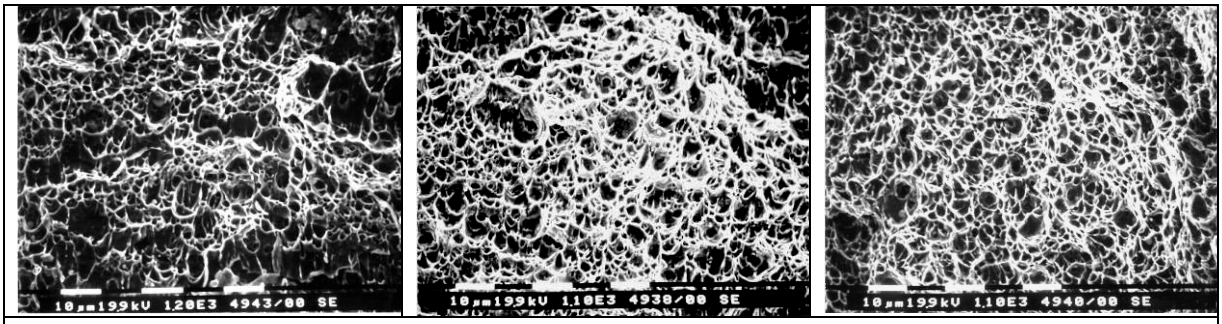

Figure D. 1. Ductile fracture with dimples for WM at 97˚C for 9.3 mm/s, 12.3 mm/s, and 15.3 mm/s welding speeds.

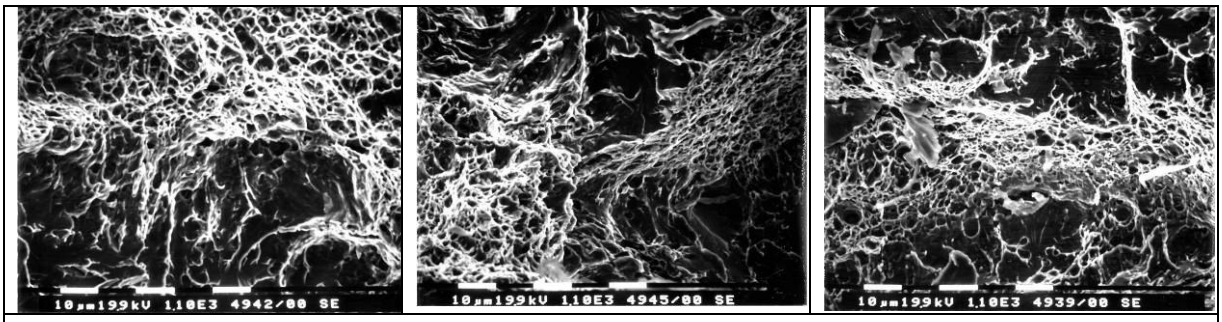

Figure D.2. Mixed fracture with quasi-cleavage for WM 9.3 mm/s and 12.3 mm/s at 22 ˚C and 15.3 mm/s at -27˚C.

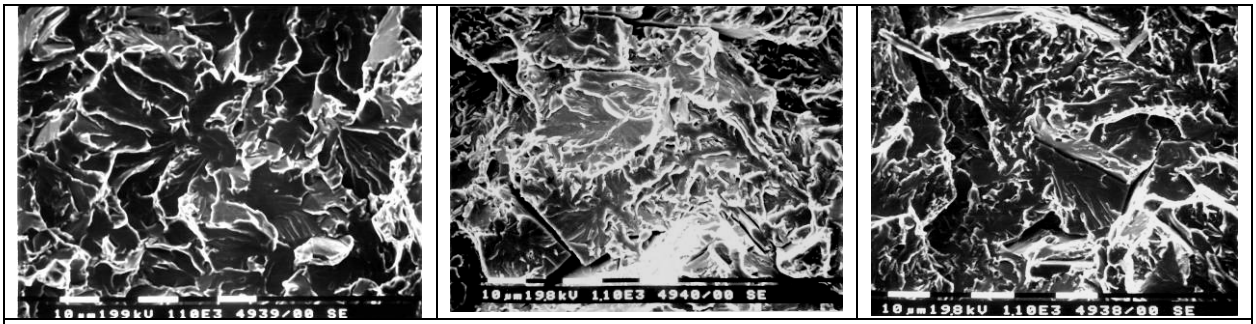

Figure D.3. Brittle fracture with cleavage and cracks for WM at -190˚C for 9.3 mm/s, 12.3 mm/s and 15.3 mm/s welding speeds.

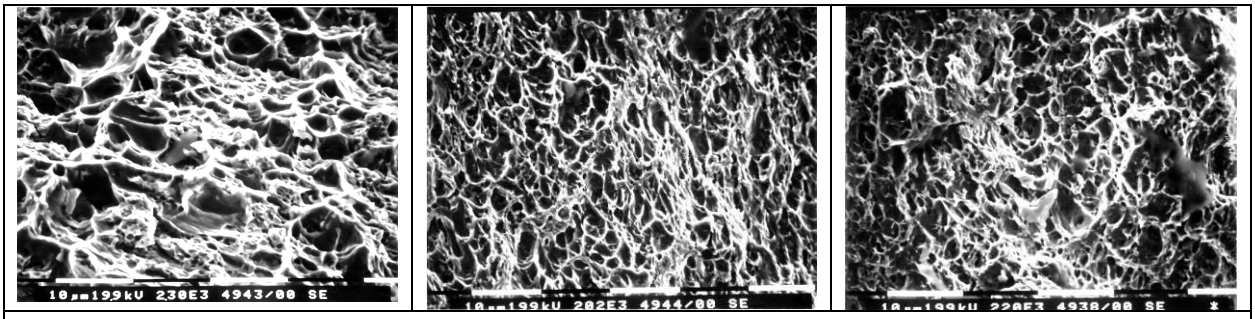

Figure D.4. Ductile fracture for HAZ at 97˚C for 9.3 mm/s, 12.3 mm/s and 15.3 mm/s welding speeds.

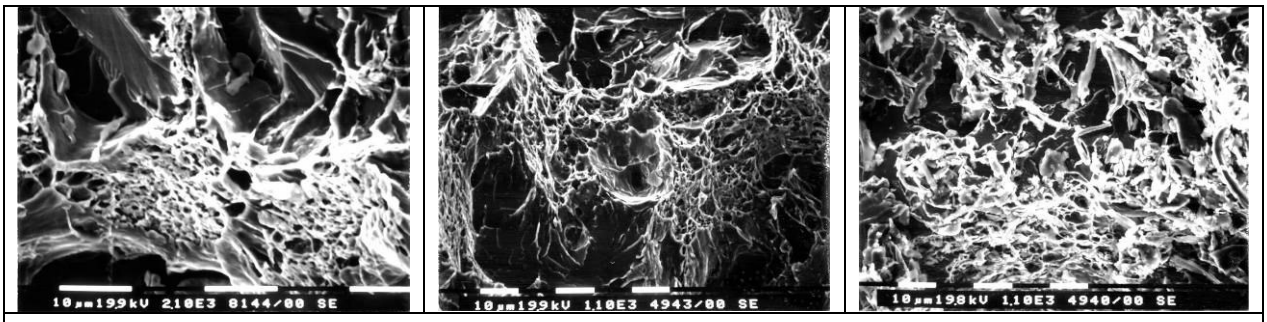

Figure D.5. Mixed fracture for HAZ at -27˚C for 9.3 mm/s, 12.3 mm/s and 15.3 mm/s welding speeds.

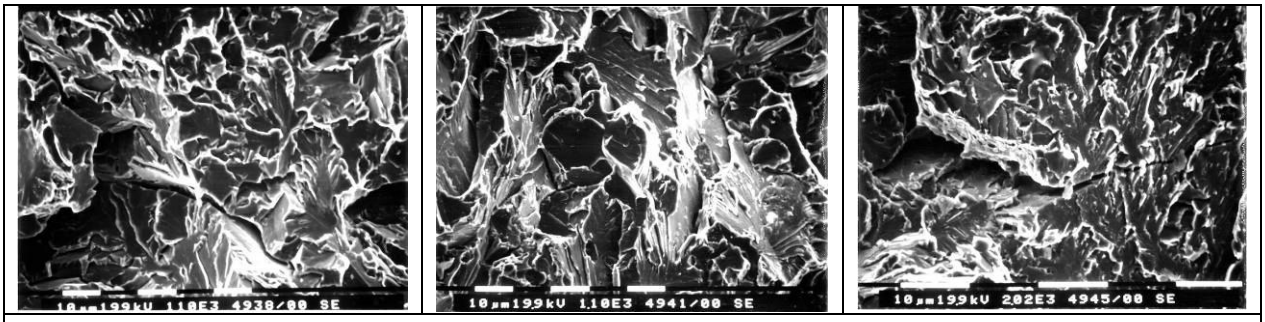

Figure D.6. Brittle fracture for HAZ at -190˚C for 9.3 mm/s, 12.3 mm/s and 15.3 mm/s welding speeds.

APPENDIX E. Lateral Expansion Data

Lateral expansion results for the 12.3 and 15.3 mm/s welding speeds are displayed in Figures E.1 and E.2. Data from the alternate lateral expansion method, Method 2 described in Section 3.3.4, which was ignored due to difficulty obtaining accurate measurements, are shown in Figures E.3 – E.7 for each of the three welding speeds.

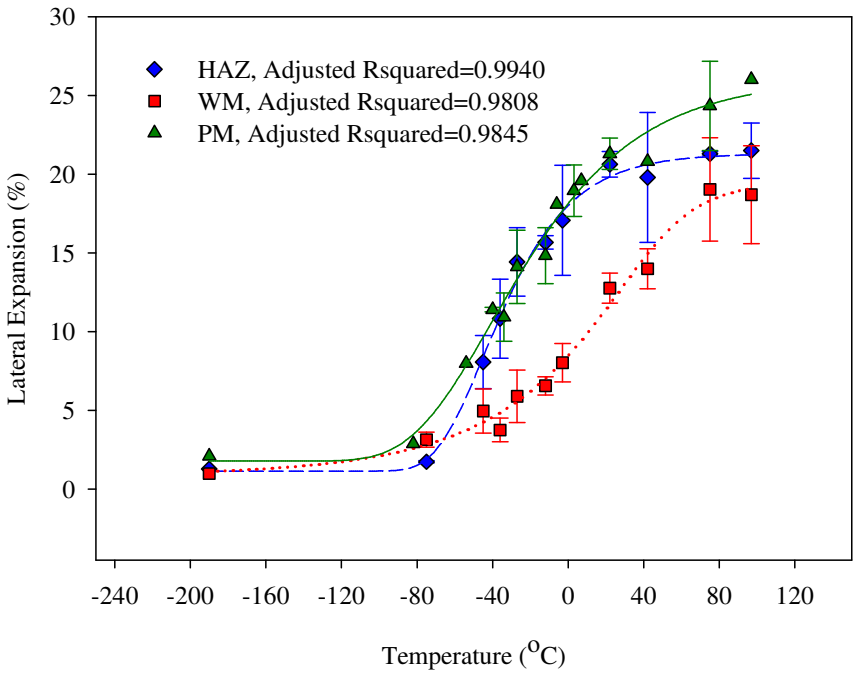

Figure E.1. Lateral expansion for 12.3 mm/s welding speed using Method 1.

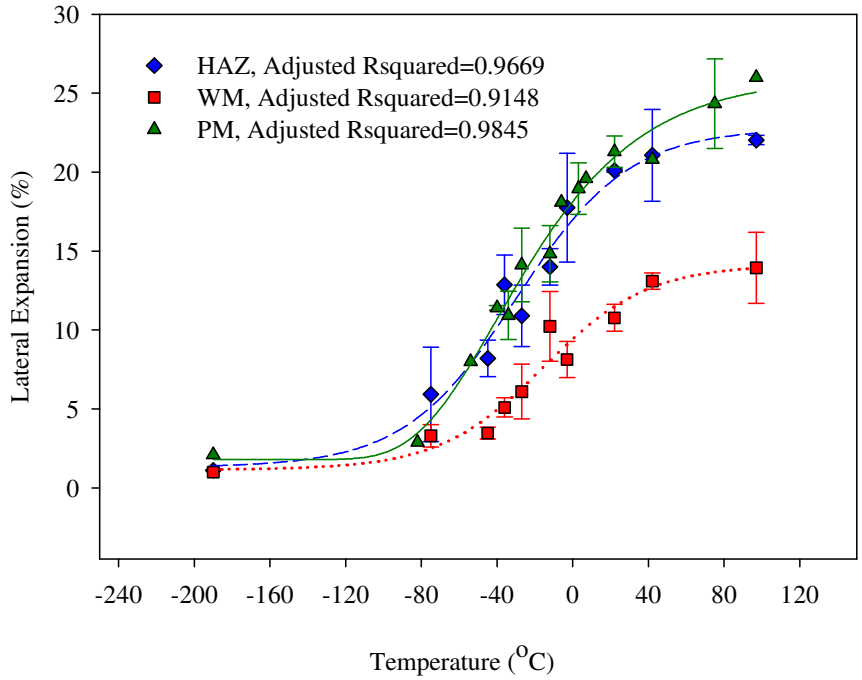

Figure E.2. Lateral Expansion for 15.3 mm/s welding speed using Method 1.

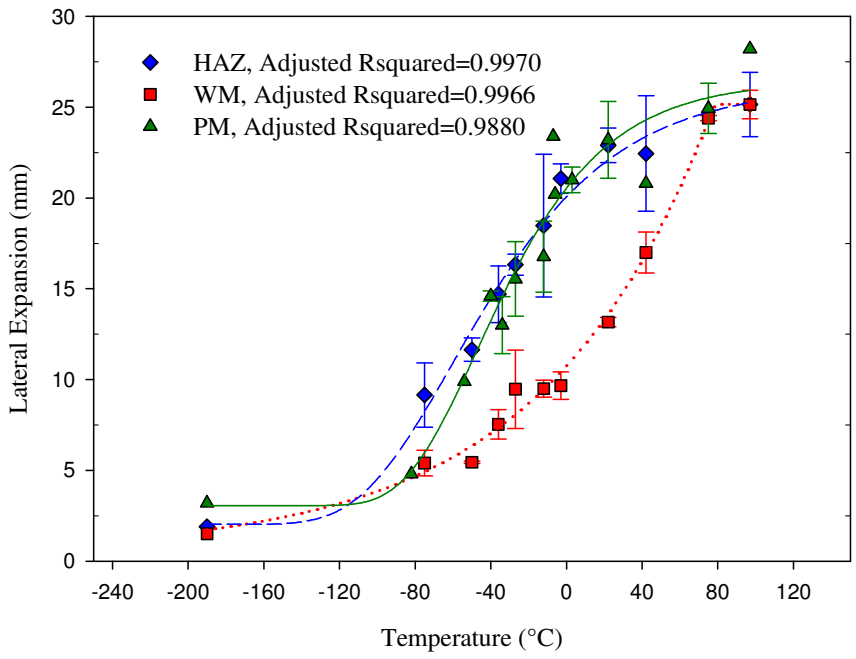

Figure E.3. Lateral Expansion for 9.3 mm/s welding speed using Method 2.

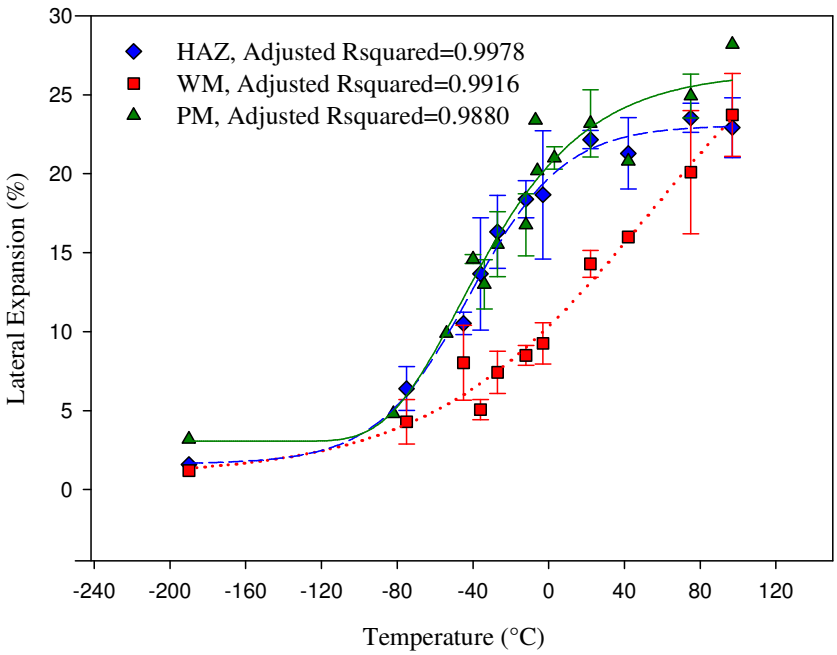

Figure E.4. Lateral Expansion for 12.3 mm/s welding speed using Method 2.

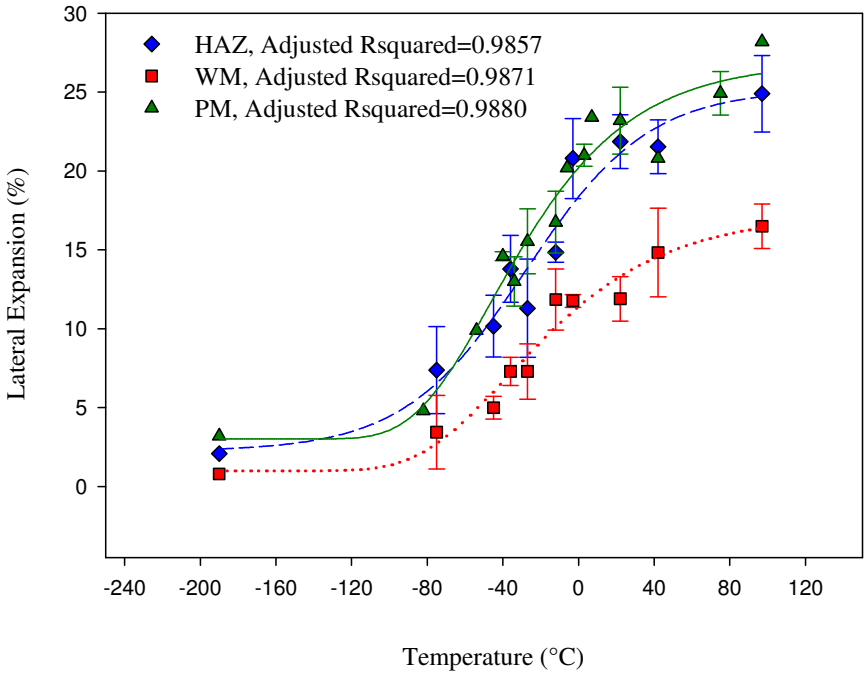

Figure E.5. Lateral Expansion for 15.3 mm/s welding speed using Method 2.

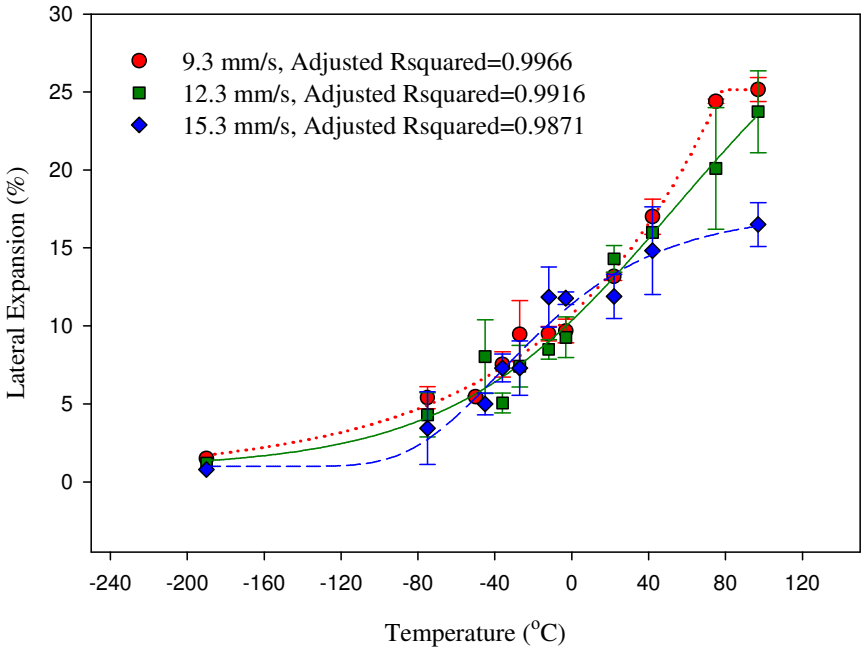

Figure E.6. Effect of welding speed on lateral Expansion of the WM using Method 2.

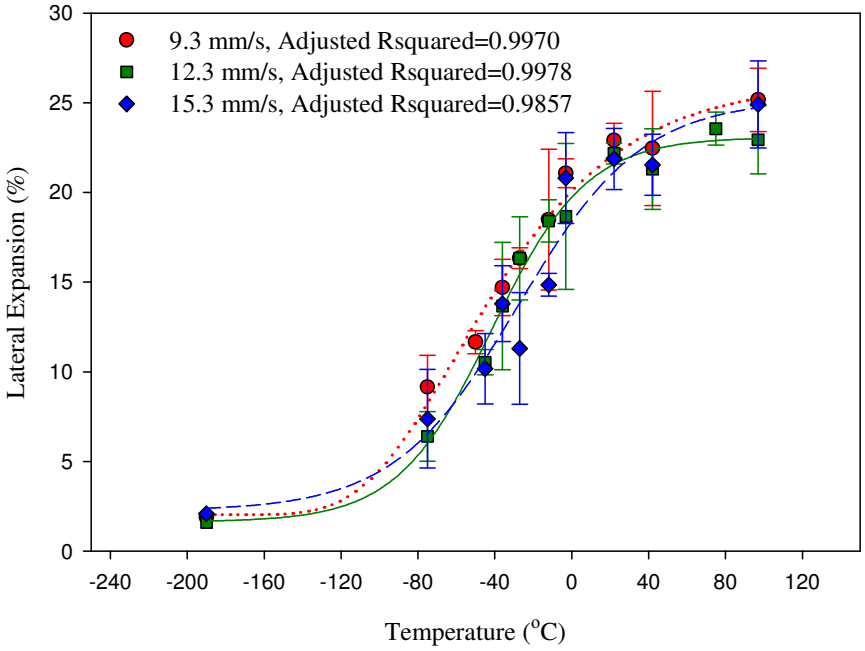

Figure E.7. Effect of welding speed on lateral Expansion of the HAZ using Method 2.

APPENDIX F. Copyright Permissions

From: **Penny Edmundson** (penny.edmundson@twi.co.uk)
Sent: September 10, 2009 7:17:41 AM
To: amh117@mail.usask.ca
Cc: Christine Talbot (christine.talbot@twi.co.uk)

Dear Alicia

You are welcome to use the photograph mentioned. However, please do caption it 'Courtesy of TWI' as you suggested.

Regards

Penny

Penny Edmundson BSc
Marketing,Products and Promotions
TWI Ltd, Granta Park, Great Abington,
Cambridge CB21 6AL United Kingdom
E-mail: penny.edmundson@twi.co.uk <mailto:penny.edmundson@twi.co.uk>
Tel: +44 (0)1223 899000
Fax: +44 (0)1223 892794

TWI Ltd
Registered Number: 3859442 England
Registered Office: Granta Park, Great Abington, Cambridge, CB21 6AL, UK

Hall, Alicia

From: Brian Bartlett [brian@bbweldingservices.co.uk]
Sent: Thursday, September 24, 2009 10:24 AM
To: Hall, Alicia
Subject: Re: Permission for use of photos in Master's Thesis

Hi Alicia.
Yes you can use the two photos and good luck with your thesis.
Regards.
Brian.

---- Original Message ----
From: Hall, Alicia
To: brian@bbweldingservices.co.uk
Sent: Thursday, September 10, 2009 12:45 AM
Subject: Permission for use of photos in Master's Thesis

Hello Brian,

I am a Master of Science student at the University of Saskatchewan in Saskatoon, Saskatchewan, Canada. I am writing a thesis studying the effects of welding parameters on the mechanical properties of a specific steel. In the literature review I discuss weld defects that can occur and would like to use your lack of root fusion and slag inclusion defect photos that you have posted on the following page:

http://www.bbweldingservices.co.uk/Test_Specimens/test_specimens.htm

I would appreciate it very much if you would grant me permission to use this photo within my literature review. I will have your website as a reference and acknowledge your company in my acknowledgements section.

Thank you very much for your consideration. If you could reply as soon as possible so I can submit my thesis that would be much appreciated.

Thank you,

Alicia Hall
Graduate Student

Hall, Alicia

From: Pullinen Mirjami [Mirjami.Pullinen@vtt.fi]
Sent: Tuesday, September 22, 2009 1:27 AM
To: Hall, Alicia
Subject: RE: Copyright permission

Hello again!
I just got a confirmation that you´re free to use the figure. Here´s how the publication should be referred to:

Vilpas, Martti; Tihekari, Hannele; Karppi, Risto. 1985. Mechanical properties of SMA- and SA-welded joints for quenched and tempered high-strength steel N-A-XTRA 70. Espoo, VTT. 26 p. Tutkimuksia (Researches) / Technical Research Centre of Finland; 363.
ISBN 951-38-2402-0.

Have a great autumn!
Regards,
Mirjami

Mirjami Pullinen
Publications editor
VTT, Knowledge solutions
+358 20 722 6530

Hall, Alicia

From: LibraryKCBL, Vancouver
Sent: Friday, September 25, 2009 9:31 AM
To: Hall, Alicia
Subject: FW: Request for permission to republish in a thesis: article from Welding Journal

---

From: Mary Ruth Johnsen [mailto:mjohnsen@aws.org]
Sent: Friday, September 25, 2009 6:30 AM
To: LibraryKCBL, Vancouver
Subject: Re: Request for permission to republish in a thesis: article from Welding Journal

Kim,

You have our permission to use the requested figures under the following conditions:

The figures cannot be altered.

Credit must be given to the Welding Journal, American Welding Society, Miami, Fla.

We retain the copyright so they can't be used for other purposes than this without our permission.

Let me know if you need anything else.

Mary Ruth Johnsen
Editor, Welding Journal and Inspection Trends
550 NW LeJeune Rd.
Miami, FL 33126
(800) 443-9353 ext. 238
FAX: (305) 443-7404

Plan now to attend the 2009 FABTECH International and AWS Welding Show on November 15-18, 2009 in Chicago, IL. {It's North America's largest welding, metal forming and fabricating event.} For more information, please visit www.aws.org/expo <http://www.aws.org/expo> .

On 9/24/09 3:11 PM, "LibraryKCBL, Vancouver" <library@klohn.com> wrote:

> Dear Mary Ruth Johnson, Editor, Publishing Services, Welding Journal.
>
> Our engineer Alicia Hall is requesting to include the graphs in Figures 3 and 9 from the following paper in her literature review for her thesis, entitled "Effects of Submerged Arc Welding Parameters on the Mechanical Properties of a Specific Steel".
>
> Microstructure/Mechanical Property Relationships of Submerged Arc Welds in HSLA 80 Steel
> N.J. Smith, J.T. McGrath, J.A. Ginaetto, R.F. Orr
> Welding Journal , March 1989, Volume 68, Issue 3, pp 112-120
>
> Please advise,
>
> Kim Feltham

9/25/2009

APPENDIX G. Curve Fit

The curve fit statistics for each of the Charpy impact and lateral expansion curves are listed according to the welding speed and location of the notch.

Charpy Curve Fits:

Parent Metal

Transverse
Equation: Weibull, 5 Parameter

R	Rsqr	Adj Rsqr	Standard Error of Estimate
0.9990	0.9979	0.9968	4.4778

	Coefficient	Std. Error	t	P	VIF
a	117.3648	5.3716	21.849	<0.0001	8.7047<
b	1142367.464	154501345.1	0.0074	0.9943	4396512.0370<
c	33013.3322	4463758.193	0.0074	0.9943	4396401.6467<
x0	-18.5038	2.9553	-6.2613	0.0001	4.3307<
y0	1.5797	4.2257	0.3738	0.7172	12.4680<

Longitudinal
Equation: Sigmoidal, Gompertz, 3 Parameter
f=a*exp(-exp(-(x-x0)/b))

R	Rsqr	Adj Rsqr	Standard Error of Estimate
0.9816	0.9636	0.9563	16.0034

	Coefficient	Std. Error	t	P	VIF
a	228.2884	16.0528	14.2211	<0.0001	4.6886<
b	39.9836	8.1119	4.929	0.0006	2.9424
x0	-36.5317	4.4606	-8.1899	<0.0001	2.1082

9.3 mm/s Weld:

Weld Metal
Equation: Sigmoid, 5 Parameter

R	Rsqr	Adj Rsqr	Standard Error of Estimate
0.9999	0.9998	0.9997	0.9620

	Coefficient	Std. Error	t	P	VIF
a	103.2832	1.3276	77.7961	<0.0001	5.3680<
b	1.5977	182.1091	0.0088	0.9933	103667443.3346<
c	0.0321	3.6558	0.0088	0.9933	103667843.7420<
x0	62.5368	1.1912	52.5006	<0.0001	5.3949<
y0	1.7174	0.9156	1.8757	0.1098	9.9650<

HAZ
Equation: Weibull, 5 Parameter

R	Rsqr	Adj Rsqr	Standard Error of Estimate
0.9983	0.9966	0.9932	6.7533

	Coefficient	Std. Error	t	P	VIF
a	112.1078	8.54	13.1274	<0.0001	7.0813<
b	300.6341	859.791	0.3497	0.7408	499.7922<
c	8.9141	26.4139	0.3375	0.7495	505.1608<
x0	-27.622	4.6717	-5.9127	0.002	3.1823
y0	8.1454	6.9883	1.1656	0.2964	10.7082<

12.3 mm/s:

HAZ
Equation: Gompertz, 4 Parameter

R	Rsqr	Adj Rsqr	Standard Error of Estimate
0.9992	0.9984	0.9974	4.4370

	Coefficient	Std. Error	t	P	VIF
a	120.6193	5.8682	20.5548	<0.0001	8.8606<
b	31.5807	3.9077	8.0817	<0.0001	3.2056
x0	-40.2092	2.8061	-14.3293	<0.0001	3.2013
y0	6.0649	3.9733	1.5264	0.1707	8.8207<

Weld Metal
Equation: Sigmoid, 4 Parameter

R	Rsqr	Adj Rsqr	Standard Error of Estimate
0.9989	0.9978	0.9965	3.1706

	Coefficient	Std. Error	t	P	VIF
a	112.0344	8.7104	12.8622	<0.0001	16.6665<
b	32.7201	4.1309	7.9208	<0.0001	6.6573<
x0	27.824	5.5144	5.0457	0.0015	9.3008<
y0	4.5306	2.7498	1.6476	0.1434	8.2739<

15.3 mm/s:

HAZ
Equation: Weibull, 5 Parameter

R	Rsqr	Adj Rsqr	Standard Error of Estimate
0.9977	0.9954	0.9908	7.8557

	Coefficient	Std. Error	t	P	VIF
a	123.0361	10.9019	11.2858	<0.0001	7.9424<
b	436319.3368	260790254	0.0017	0.9987	19092237.5775<
c	12065.0773	7212373.17	0.0017	0.9987	19090119.6365<
x0	-22.7101	9.0004	-2.5232	0.053	9.1531<
y0	3.2268	7.9827	0.4042	0.7028	10.3260<

Weld Metal
Equation: Sigmoid, 4 Parameter

R	Rsqr	Adj Rsqr	Standard Error of Estimate
0.9927	0.9855	0.9819	4.9891

	Coefficient	Std. Error	t	P	VIF
a	54.5089	4.9298	11.057	<0.0001	7.3518<
b	22.7956	4.7764	4.7725	0.0002	2.228
x0	-19.7981	5.1104	-3.8741	0.0013	3.2785
y0	3.9245	3.173	1.2369	0.234	8.0892<

Lateral Expansion Curve Fits:

Method 1:

Parent Metal
Equation: Sigmoidal, Gompertz, 3 Parameter
f=a*exp(-exp(-(x-x0)/b))

R	Rsqr	Adj Rsqr	Standard Error of Estimate
0.9934	0.9868	0.9845	0.9728

	Coefficient	Std. Error	t	P	VIF
a	26.0961	1.0077	25.8956	<0.0001	6.2290<
b	43.4704	4.7714	9.1107	<0.0001	4.2113<
x0	-44.2694	2.5958	-17.0541	<0.0001	2.2545

9.3 mm/s:

HAZ
Equation: Sigmoidal, Sigmoid, 3 Parameter
f= a/(1+exp(-(x-x0)/b))

R	Rsqr	Adj Rsqr	Standard Error of Estimate
0.9752	0.9511	0.9371	1.9353

	Coefficient	Std. Error	t	P	VIF
a	23.2102	1.7474	13.2826	<0.0001	3.7056
b	28.428	7.1085	3.9991	0.0052	1.9278
x0	-37.0155	6.7526	-5.4816	0.0009	2.3729

Weld Metal
Equation: Sigmoidal, Weibull, 4 Parameter
f= if(x<=x0-b*ln(2)^(1/c), 0, a*(1-exp(-(abs(x-x0+b*ln(2)^(1/c))/b)^c)))

R	Rsqr	Adj Rsqr	Standard Error of Estimate
0.9990	0.9980	0.9972	0.4065

	Coefficient	Std. Error	t	P	VIF
a	23.1244	0.7766	29.7781	<0.0001	10.2158<
b	173385.0202	57453127.82	0.003	0.9977	115005087.8565<
c	3858.446	1278828.145	0.003	0.9977	115022617.0380<
x0	20.1223	2.4272	8.2904	<0.0001	5.0180<

12.3 mm/s:

HAZ
Equation: Sigmoidal, Gompertz, 3 Parameter
f=a*exp(-exp(-(x-x0)/b))

R	Rsqr	Adj Rsqr	Standard Error of Estimate
0.9976	0.9952	0.9940	0.5985

	Coefficient	Std. Error	t	P	VIF
a	20.9798	0.3918	53.5426	<0.0001	2.4622
b	25.9857	2.2638	11.4786	<0.0001	2.5341
x0	-44.8621	1.4041	-31.9513	<0.0001	1.598

Weld Metal
Equation: Sigmoidal, Weibull, 4 Parameter
f= if(x<=x0-b*ln(2)^(1/c), 0, a*(1-exp(-(abs(x-x0+b*ln(2)^(1/c))/b)^c)))

R	Rsqr	Adj Rsqr	Standard Error of Estimate
0.9933	0.9866	0.9808	0.8945

	Coefficient	Std. Error	t	P	VIF
a	19.0592	0.9759	19.5302	<0.0001	4.0402<
b	1200992.371	507950971.4	0.0024	0.9982	23735036.4454<
c	27223.9434	11516815.9	0.0024	0.9982	23739758.6442<
x0	7.1729	7.5039	0.9559	0.371	7.6017<

15.3 mm/s:

HAZ
Equation: Sigmoidal, Sigmoid, 3 Parameter
f= a/(1+exp(-(x-x0)/b))

R	Rsqr	Adj Rsqr	Standard Error of Estimate
0.9871	0.9743	0.9669	1.3162

	Coefficient	Std. Error	t	P	VIF
a	22.8096	1.341	17.0088	<0.0001	4.2964<
b	30.6581	5.5026	5.5716	0.0008	1.9982
x0	-30.9202	5.2837	-5.852	0.0006	2.8578

Weld Metal
Equation: Sigmoidal, Sigmoid, 3 Parameter
f= a/(1+exp(-(x-x0)/b))

R	Rsqr	Adj Rsqr	Standard Error of Estimate
0.9663	0.9337	0.9148	1.2575

	Coefficient	Std. Error	t	P	VIF
a	14.5616	1.7208	8.4622	<0.0001	6.0384<
b	35.9483	10.0344	3.5825	0.0089	2.2763
x0	-15.9867	11.6131	-1.3766	0.211	4.9736<

Method 2:

Parent Metal
Equation: Gompertz, 4 Parameter

R	Rsqr	Adj Rsqr	Standard Error of Estimate
0.9957	0.9914	0.9880	2.0361

	Coefficient	Std. Error	t	P	VIF
a	23.4024	2.8745	8.1414	<0.0001	12.5374<
b	38.1513	10.0267	3.805	0.0035	4.4214<
x0	-47.0254	7.8101	-6.0211	0.0001	4.4057<
y0	3.0571	1.9144	1.5969	0.1414	12.3765<

9.3 mm/s:

HAZ
Equation: Gompertz, 4 Parameter

R	Rsqr	Adj Rsqr	Standard Error of Estimate
0.9991	0.9982	0.9970	0.9672

	Coefficient	Std. Error	t	P	VIF
a	24.1735	1.6642	14.5254	<0.0001	12.7868<
b	48.8134	7.9247	6.1596	0.0008	5.8643<
x0	-59.9711	5.0106	-11.969	<0.0001	4.0238<
y0	2.026	0.964	2.1018	0.0803	9.9332<

Weld Metal
Equation: Sigmoid, 5 Parameter

R	Rsqr	Adj Rsqr	Standard Error of Estimate
0.9991	0.9981	0.9966	0.8012

	Coefficient	Std. Error	t	P	VIF
a	24.6353	1.4436	17.0654	<0.0001	10.4218<
b	0.3779	4442.5445	8.51E-05	0.9999	123836987027.7849<
c	0.0042	49.8935	8.51E-05	0.9999	123839713939.8692<
x0	78.2302	8.5162	9.186	<0.0001	19.1130<
y0	0.5147	1.2008	0.4287	0.6831	24.7070<

12.3 mm/s:

HAZ
Equation: Sigmoid, 4 Parameter

R	Rsqr	Adj Rsqr	Standard Error of Estimate
0.9993	0.9986	0.9978	0.8150

	Coefficient	Std. Error	t	P	VIF
a	21.4434	1.0373	20.6732	<0.0001	9.7689<
b	24.6129	2.9816	8.2548	<0.0001	2.1267
x0	-41.5162	3.1401	-13.221	<0.0001	2.9229
y0	1.6291	0.815	1.9988	0.0858	11.0022<

Weld Metal
Equation: Sigmoid, 4 Parameter

R	Rsqr	Adj Rsqr	Standard Error of Estimate
0.9973	0.9946	0.9916	1.1583

	Coefficient	Std. Error	t	P	VIF
a	33.3326	11.6673	2.8569	0.0244	141.0589<
b	57.8324	18.3033	3.1597	0.0159	26.9844<
x0	53.4061	38.0183	1.4047	0.2029	131.0026<
y0	0.8713	1.5251	0.5713	0.5857	19.0715<

15.3 mm/s:

HAZ
Equation: Sigmoid, 4 Parameter

R	Rsqr	Adj Rsqr	Standard Error of Estimate
0.9957	0.9914	0.9857	1.9621

	Coefficient	Std. Error	t	P	VIF
a	22.9454	3.3444	6.8608	0.0005	11.3412<
b	32.2804	10.0282	3.219	0.0182	2.739
x0	-27.6316	10.0302	-2.7548	0.0331	4.3998<
y0	2.244	2.0472	1.0961	0.3151	10.8852<

Weld Metal
Equation: Gompertz, 4 Parameter

R	Rsqr	Adj Rsqr	Standard Error of Estimate
0.9961	0.9923	0.9871	1.1671

	Coefficient	Std. Error	t	P	VIF
a	16.2885	2.2488	7.243	0.0004	12.2928<
b	46.6045	13.1911	3.533	0.0123	4.5080<
x0	-37.4074	8.5117	-4.3948	0.0046	4.6557<
y0	0.9941	1.13	0.8798	0.4128	9.3736<

APPENDIX H. Additional Details of Results

Tables of data including error details not already included in the thesis, are listed here for reference. In all cases error values shown in these tables of experimental results represent the standard deviation for the value.

Table H.1. Average tensile data for varying welding speeds and the parent metal.

		Welding Speed (mm/s)		
Property	PM	9.3 (mm/s)	12.3 (mm/s)	15.3 (mm/s)
YS (MPa)	344.7±19	320.2±7	319.2±4	336.3±5
TS (MPa)	536.8±1	543.4±3	539.5±0	542.4±1
El (%) (50.8 mm gauge length)*	39.8	26	27.8	23.4

*Individual data were not available.

Table H.2. Hitachi minimum impact toughness requirements.

Location (Speed mm/s)	**Energy at –30 ˚C (J)**	**≥ 27 J?**
WM (9.3)	24±3	No
WM (12.3)	28±9	Yes
WM (15.3)	34±8	Yes
HAZ (9.3)	83±7	Yes
HAZ (12.3)	89±21	Yes
HAZ (15.3)	77±12	Yes
PM Trans.	64±13	Yes
PM Long.*	98	Yes

*Only one sample was tested for the PM cut longitudinal to the rolling direction at this temperature.